Aus dem Departement für Physik
Universität Freiburg (Schweiz)

Interaction of hydrogen with sp^2-bonded carbon: Effects on the local electronic structure

Inaugural-Dissertation

zur Erlangung der Würde eines *Doctor rerum naturalium*
der Mathematisch-Naturwissenschaftlichen Fakultät
der Universität Freiburg in der Schweiz

vorgelegt von

Pascal Ruffieux

aus Plasselb (FR)

Dissertation Nr. 1387

Paulusdruckerei Freiburg

2002

Von der Mathematisch-Naturwissenschaftlichen Fakultät der Universität Freiburg in der Schweiz angenommen, auf Antrag der Herren

Prof. Dr. Peter Schurtenberger, Universität Freiburg (Präsident der Jury)
Dr. Pierangelo Gröning, Universität Freiburg (Referent)
Prof. Dr. Christian Schönenberger, Universität Basel (Koreferent)
Prof. Dr. Øystein Fischer, Université de Genève (Koreferent)
Prof. Dr. Louis Schlapbach, Universität Freiburg (Koreferent)

Der Leiter der Dissertation

Dr. Pierangelo Gröning

Der Dekan

Prof. Dr. Dionys Baeriswyl

Abstract

The presented thesis treats the local structural and electronic modification induced by point defects incorptorated in sp^2-bonded carbon networks. The work is motivated by the ongoing efforts to miniaturise electronic devices down to the molecular level. The electronic properties of devices working at this level can be substantially altered due to the presence of single atomic defects. Carbon-based structures are thought to have a great potential in the field of molecular electronics due to the variety of electronic properties they can exhibit. For instance, carbon nanotubes, which consist of rolled-up graphene sheets can show either semiconducting or metallic conduction, depending on their diameter and chiral angle. For the local modification of the electronic structure of sp^2-bonded carbon, hydrogen chemisorption is particularly interesting, since it induces a rehybridisation of the carbon orbitals to a sp^3-configuration.

The first two chapters of this thesis start with some introductory remarks in order to point out the scope of the presented work and give a brief review of the properties of carbon allotropes and the experimental methods used for the presented investigations.

Our experimental results on the interaction of hydrogen with sp^2-bonded carbon are presented in chapter 3, where we discuss the influence of the local curvature of the carbon network on the adsorption energy barrier for hydrogen chemisorption. For this purpose we studied the interaction of atomic and ionic hydrogen with C_{60} molecules, single-walled carbon nanotubes and graphite by means of photoemission experiments. The samples have been chosen to represent a wide range of curvatures in the sp^2-bonded carbon network. Our findings show a pronounced increase of the adsorption energy barrier with decreasing local curvature of the carbon surface. Furthermore, the adsorption energy barrier shows a marked dependence on the hydrogen coverage. The observed behaviour is attributed to the increasing sp^3-character of the hybridisation as the local curvature of the carbon network is increased.

The fourth chapter treats the local modifications of the electronic structure in the vicinity of defects at the graphite surface. Scanning probe microscopy studies reveal a long-range redistribution of the charge density induced by hy-

drogen adsorption sites and atomic vacancies. For single atomic defects the range of the induced electronic modifications is of the order of 6 nm. The underlying effect for this redistribution is large momentum scattering of electron waves at the defect sites which results in standing waves in the charge density. The interference of such standing waves results in a variety of patterns in the charge distribution, where their symmetry is directly related to the Fermi surface of graphite, as can be shown by a simulation.

Polycyclic aromatic hydrocarbons can be viewed as being hydrogen terminated graphite sections on the molecular level. Their exactly controllable size and the possibility to attach functional chains make them attractive for the application as building blocks for molecular devices. In chapter 5, we present the investigations of the self-assembly of hexa-*peri*-hexabenzocoronene (HBC) at metal surfaces. The X-ray photoelectron diffraction study reveals the growth of columnar structures, where the disc-shaped molecules are stacked parallel to each other due to the non-covalent interaction between the molecules. The seperation between the columns has been found to depend on the two-dimensional lattice formed by the first molecular monolayer and is, therefore, substrate dependent.

Zusammenfassung

Das Thema dieser Doktorarbeit ist die Untersuchung des Einflusses von Punktdefekten auf die lokale elektronische Struktur von sp^2-gebundenem Kohlenstoff. Die Motivation für die vorgelegte Arbeit sind die Bestrebungen, die zentralen Komponenten von elektronischen Schaltkreisen auf die Längenskala von molekularen Strukturen zu reduzieren ($\sim$ nm). Die elektronischen Eigenschaften von Strukturen dieser Grössenordnung werden massgeblich von atomaren Defekten beeinflusst, weshalb das genaue Kennen derer Auswirkungen von grosser Wichtigkeit ist. Auf Kohlenstoff basierende Strukturen sind dabei besonders interessant, da sie sich durch eine Vielfalt von elektronischen Eigenschaften auszeichnen. Zum Beispiel können Kohlenstoff - Nanoröhrchen je nach Durchmesser und Chiralität halbleitendes oder metallisches Leitungsverhalten zeigen. Für die lokale Veränderung der elektronischen Eigenschaften von sp^2-gebundenem Kohlenstoff ist die Chemisorption von Wasserstoff besonders interessant, da sie eine lokale sp^3-Hybridisierung der Kohlenstofforbitale bewirkt.

Die ersten zwei Kapitel dieser Doktorarbeit geben einen kurzen Überblick über die Eigenschaften der verschiedenen Formen von Kohlenstoff sowie über die verwendeten experimentellen Methoden, Photoelektronenspektroskopie und Rastersondenmikroskopie.

Im dritten Kapitel diskutieren wir die Untersuchungen, die wir bezüglich der Wechselwirkung zwischen Wasserstoff und sp^2-gebundenem Kohlenstoff gemacht haben. Die zentrale Fragestellung dabei ist der Einfluss der lokalen Krümmung der Kohlenstoffstrukturen auf die Chemisorption des Wasserstoffs. Dazu wurden C_{60}-Moleküle, einwandige Kohlenstoff-Nanoröhrchen, sowie Graphit untersucht, womit ein grosser Bereich von verschiedenen Krümmungen in sp^2-gebundenem Kohlenstoff abgedeckt ist. Unsere Resultate zeigen, dass grosse Krümmungen im Kohlenstoffgitter zu einer erniedrigten Energiebarriere für die Chemisorption von Wasserstoff führen. Des weiteren wurde eine ausgeprägte Änderung dieser Energiebarriere als Funktion der Wasserstoffbedeckung festgestellt.

Im vierten Kapitel berichten wir von Resultaten zu den lokalen Änderungen der elektronische Struktur in der Nähe von Punktdefekten im Graphitgitter.

Die Rastersondenmikroskopiemessungen zeigen eine langreichtweitige Neuverteilung der Ladungsdichte, die von einzelnen adsorbierten Wasserstoffatomen und atomaren Fehlstellen induziert wird. Der Ursprung für diese Neuverteilung ist die Streuung der Elektronen an den Defektstellen, was zu stehenden Wellen in der Ladungsdichte führt. Die Interferenz von stehenden Wellen, die ihren Ursprung bei verschiedenen Defekten haben, ergibt eine Vielzahl von Strukturen in der Ladungsverteilung. Eine Simulation der experimentell beobachteten Ladungsverteilungen zeigt, dass deren Symmetrie direkt mit den Konturen der Fermifläche von Graphit zusammenhängt.

Polyzyklische aromatische Kohlenwasserstoffe sind Moleküle, die als wasserstoffterminierte Graphitteilstücke angesehen werden können. Ihre exakt kontrollierbare Grösse sowie die Möglichkeit, sie mit chemisch funktionellen Ketten zu versehen, machen sie interssant für die Verwendung als Bausteine für den Bau von funktionalisierten molekularen Strukturen. Das letzte Kapitel beschäftigt sich mit Untersuchungen, die wir bezüglich der Selbstorganisation von polyzyklischen aromatischen Kohlenwasserstoffen an Metalloberflächen ausgeführt haben. Die mit Photoelektronendiffraktion unternommene Studie offenbart das Ausbilden von turmartigen Strukturen, wobei die scheibenförmigen Moleküle parallel zueinander gestapelt sind und ihre Orientierung bei wachsender Stapelhöhe erhalten bleibt. Die Turmabstände werden dabei vom Gitter, das die erste Molekülllage bildet, vorgegeben. Dieses wiederum hängt von der Struktur des gewählten Substrates ab, womit eine Variation der Distanz zwischen den Molekültürmen möglich ist.

Contents

Preface

This thesis is based on research carried out at the *Departement für Physik der Universität Freiburg, Schweiz*. It consists of five chapters and an appendix: The first two chapters give an introduction to the carbon systems and an overview on the experimental methods used for the investigations. Chapter three consists of an article dealing with the chemisorption of hydrogen with sp^2-bonded carbon networks having different local curvatures. The fourth chapter comprises two articles where we focus on the local modifications of the electronic structure of graphite induced by individual atomic defects. The fifth chapter consists of an article where we report on the study of the self-assembly of hexabenzocoronenes at noble metal surfaces. In Appendix A we report on the work done on the characterisation of an electron analyser used for the photoemission experiments in this work.

The sections in the chapters 3 - 5 and the appendix consist of independent articles written during this thesis. Consequently, each section stands on its one and includes an introduction, a description of the experiment, results, discussion and the references of the article allowing the reader to study these sections independently.

The articles included in this thesis are:

Chapter 1

Introduction

1.1 Introductary Remarks and Scope

In 1959 Richard Feynman gave his nowadays famous lecture *"There's Plenty of Room at the Bottom"*. The purpose of his talk was to convince the audience that there are new laws to be discovered and to be taken into account when structures are miniaturised down to the atomic level. For instance, he anticipated that quantised energy levels that are characteristic for structures on the atomic scale could be used for a new information technology.

Technological developements of the last four decades were marked by enormous efforts to miniaturise electronic devices in order to increase computational speed and the transistor density. The progress made has led to today's semiconductor technology, which allows the integration of 55 million transistors on a single chip (P4, Intel) with a density as high as 300'000 per mm^2 at a price of about 10^{-4} cents per transistor. Although the miniaturisation of the structures has progressed at an enormous pace, this "top-down" strategy, where the existing technology is stressed to create ever-smaller features, will reach fundamental limits within the next few years, making alternative approaches necessary.

The invention of the *Scanning Probe Microsopy* techniques in the early 1980's has set a milestone in science. These methods offered for the first time the possibility of direct imaging and manipulation of individual atoms and molecules. What has been forseen by Feynman, could now be realised by using

these techniques: The building of small structures where quantum mechanical effects predominate. This new ability for building functional structures out of individual atoms or molecules, a technique belonging to the "bottom-up" strategy, has initiated a large number of activities in the field of the so called nano-technology. Beside the interest for possible applications, the builiding of such low-dimensional structures is also attractive from an academic point of view, since their physical and chemical properties can be very different from those of the bulk.

In recent years carbon has attracted much interest as a post-silicon electronic material, due to the variety of stable forms and electronic properties. In particular, the discovery of the carbon nanotubes in 1991 has motivated a large number of studies of their electronic and mechanical properties in view of potential applications for electronic devices on the nanometer scale. However, for structures on the nanometer scale a high sensitivity of the electronic properties to the presence of defects has to be expected. This has been observed in several studies of the charge transport properties of carbon nanotubes where defects act as scatterers for the conduction electrons and may substantially alter the electronic properties compared to the defect-free tube. On the other hand, a controlled introduction of such defects can be used to "design" functions on individual molecules. Due to its unequalled lateral resolution scanning probe microscopy is the only technique which is capable of imaging individual defect sites and the modifications in the electronic structure induced by the defect. Of particular interest are the scattering properties and the position-dependent charge redistribution induced by defects. This modified properties influence the transport properties and the local reactivity, respectively.

Another approach within the "bottom-up" strategy is the self-assembly of molecules where the components of the individual molecules are designed to create parts attracting each other in a way to steer the final structure. Compared to the positioning of individual molecules by scanning probe techniques it has the advantage of building a large number of structures simultaneously. One promising way to grow such nano-structures in a controlled way is the combination of traditional methods for the definition of nucleation centers and self-assembly for the growth itself.

The presented thesis contributes to the above mentioned questions by a study of defect-induced modifications in the topography and the electronic structure of sp^2-bonded carbon. Within this context, hydrogen is a particularly attractive candidate for the modification of the local electronic structure, since its chemisorption on the basal plane of sp^2-bonded carbon results in a local rehybridisation to a sp^3-configuration of the carbon orbitals, which locally removes the electron states from the Fermi level. This can act as scattering center for the delocalised electrons. The interaction of hydrogen with sp^2-bonded carbon is investigated on materials having different local curvatures in the carbon network, namely graphite, single-walled carbon nanotubes and C_{60}. The study of the local modifications induced by defects such as hydrogen chemisorption sites and atomic vacancies has been performed on graphite using scanning probe microscopy. Due to its flat and largely defect-free arrangement of the sp^2-bonded carbon layers, graphite is the ideal substrate for the study of long-range modifications of the electronic structure induced by artificially introduced defects.

In a second part we address the question of the self-assembly of polycyclic aromatic hydrocarbons at metal surfaces. The presented results focus on the structural arrangement of theses disc-shaped molecules for which the three-dimensional arrangement is found to depend on the intermolecular interaction as well as from the substrate-molecule interaction.

1.2 Carbon allotropes

Carbon is a group IV element with the atomic number 6 and has the electronic configuration $1s^2 2s^2 2p^2$. Carbon materials span an enormous range of mechanical and electonic properties that is larger than that of any other element. Even for materials containing exclusively carbon, a very wide range of material properties is observed. Regarding the mechanical properties of pure carbon structures we find on the one hand diamond with an extraordinary hardness and on the other hand graphite with a very weak interlayer bonding making it a good lubricant. The large range of properties for carbon materials is mainly due to the fact, that carbon can form different bonding configurations by rearranging its outer electrons. This reconfiguration of the $2s$ and the $2p$ electrons is called *hybridisation*.

1.2.1 Diamond

One possible hybridisation consists of the linear combination of one s-state and three p-states resulting in a tetrahedral arrangement of the bonds, each at an angle of 109.5° to the other. The configuration is called sp^3 and results in a coordination number of four.

Diamond is one example of a structure that satisfies this bonding arrangement. The symmetry of the diamond lattice is cubic and the atom arrangement can be described by two face-centered cubic (fcc) lattices with one lattice displaced by one-quarter of the unit cell ($a = 3.57$Å) along the [111] direction. This results in an atomic lattice with a nearest-neighbour distance of 1.54 Å which has the highest atom density of all elements although the low coordination number of 4 of the atom arrangement inidicates, that the structure is far from being close-packed. The band structure of diamond is characterised by a large energy gap of 5.5 eV between valence band maximum and the conduction band minimum. This makes it, in the undoped case, an insulator with a resistivity of $\sim 10^{20}$ Ωcm at room temperature.

The large carrier mobility and the thermal properties make diamond an interesting material for electronic applications. The p-type doping has been realised with boron, resulting in an acceptor level at 0.37 eV above the valence

band maximum [2]. However, n-type doping on the other hand has proven to be very difficult. Although substitutional doping can be achieved using the group V element nitrogen, the donor level at 1.7 eV below the conduction band minimum is far too low to be excited to the conduction band at room temperature [3]. Current investigations try to substitutionally dope diamond with phosphorus, another group V element, and with lithium and sodium, two

Properties of Graphite and Diamond

Property	Graphite[a]		Diamond
Lattice structure	Hexagonal		Cubic
Space group	$P6_3/mmc$ (D^4_{6h})		$Fd3m$ (O^7_h)
Lattice constant[b] (Å)	2.462	6.708	3.567
Atomic density (C atoms/cm^3)	1.14×10^{23}		1.77×10^{23}
Specific gravity (g/cm^3)	2.26		3.515
Specific heat (cal/g·K)	0.17		0.12
Thermal conductivity[b] (W/cm·K)[c]	30	0.06	~25
Binding energy (eV/C atom)	7.4		7.2
Debye temperature (K)	2500	950	1860
Bulk modulus (GPa)	286		42.2
Elastic moduli (GPa)	1060[d]	36.5[d]	107.6[e]
Compressibility (cm^2/dyn)	2.98×10^{-12}		2.26×10^{-13}
Mohs hardness[f]	0.5	9	10
Band gap (eV)	−0.04[g]		5.47
Carrier density (10^{18}/cm^3 at 4 K)	5		0
Electron mobility[b] (cm^2/Vsec)	20,000	100	1800
Hole mobility[b] (cm^2/Vsec)	15,000	90	1500
Resistivity (Ωcm)	50×10^{-6}	1	$\sim10^{20}$
Dielectric constant[b] (low ω)	3.0	5.0	5.58
Breakdown field (V/cm)	0	0	10^7 (highest)
Magnetic susceptibility (10^{-6}cm^3/g)	−0.5	−21	—
Refractive index (visible)	—	—	2.4
Melting point (K)	4450		4500
Thermal expansion[b] (/K)	-1×10^{-6}	$+29 \times 10^{-6}$	$\sim1\times10^{-6}$
Velocity of sound (cm/sec)	$\sim2.63\times10^5$	$\sim1\times10^5$	$\sim1.96\times10^5$
Highest Raman mode (cm^{-1})	1582	—	1332

Table 1.1: Properties of graphite and diamond [4]. The anisotropic properties for graphite are given separately (left column in-plane values and right column for the values along the c-axis).

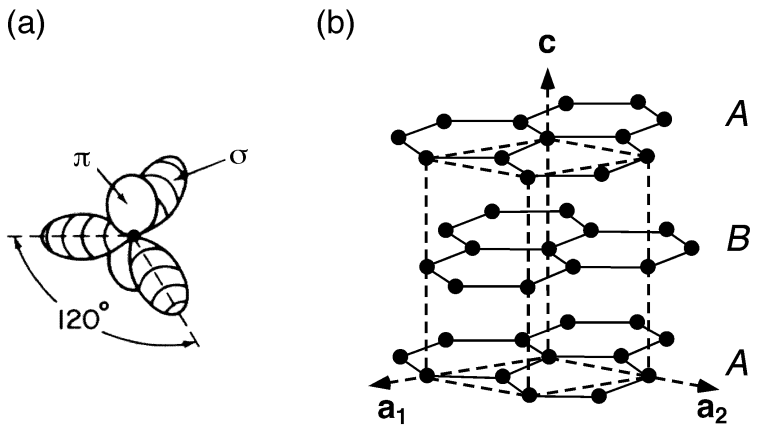

Figure 1.1: (a) Illustration of the electron charge cloud for the sp^2 hybridisation [1]. (b) Three-dimensional graphite lattice with lattice vectors and the unit cell (dashed lines).

group I elements which are expected to be incorporated on interstitial lattice positions.

1.2.2 Graphite

Another possible configuration for the bonding electrons occurs for carbon atoms that are arranged in a honeycomb network. In this geometry, bonding orbitals composed of one s and two p orbitals (sp^2) are formed 120° to each other in the same plane. These form the strong covalent bonds between the carbon atoms in graphite and are called σ-bonds. The resulting atom lattice consists of a hexagonal atom arrangement with a nearest-neighbour distance of 1.421 Å, which is about 7% shorter than in the diamond lattice. The one remaining orbital is delocalised and has a p_z configuration, called π-orbital.

The large interlayer separation of 3.354 Å leads to the very anisotropic properties of graphite (Table 1.1) and an atomic density of $1.14{\cdot}10^{23}$ atoms/cm^3, which is lower compared to the atomic density of diamond. Under ambient conditions, graphite is the thermodynamically stable form of solid carbon, whereas

diamond is only metastable.

The density of states (DOS) of graphite is shown in Fig. 1.2. Near the Fermi level, the DOS consists exclusively of the delocalised π-electrons. These states are directly related to the presence of sp^2-bonded carbon and their spectral weight in a photoemission spectrum allows, for example, the determination of the fraction of sp^2-bonded carbon in amorphous carbon [7].

The two-dimensional dispersion relation for the π-electron system can be calculated within the tight-binding approximation [5] and is displayed in Fig. 1.3. If the interaction between the sheets is neglected (treating a single graphite layer, called graphene), the DOS at the Fermi level E_F drops to zero. This is due to the fact, that the occupied π-bands and the unoccupied π^*-bands just touch at the corners of the first Brillouin zone, called the K points, making graphene a zero bandgap semiconductor. The Fermi surface consists in this case of the six K points. The occupied and the unoccupied π-bands are symmetric with respect to Fermi energy E_F. The displayed hexagon shows the two-dimensional

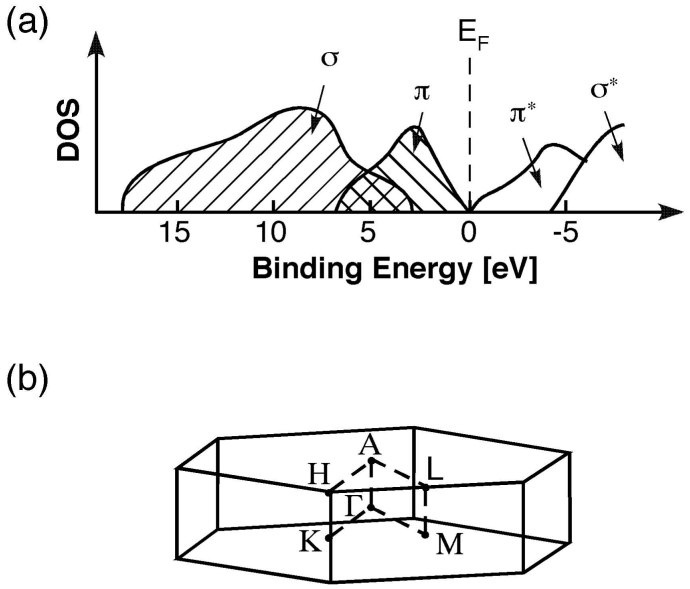

Figure 1.2: (a) Schematic representation of the DOS of graphite showing the energy position of the π- and σ-derived states relative to the Fermi level E_F. (b) First Brillouin zone of graphite showing the special points in the reciprocal lattice.

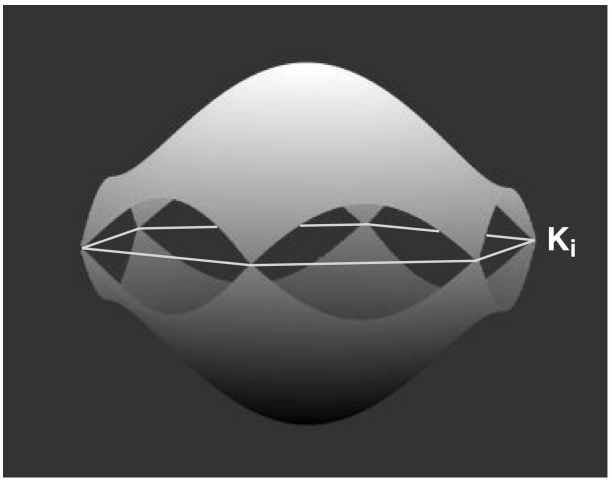

Figure 1.3: (a) Band dispersion of the occupied and unoccupied π-bands in the first Brillouin zone of graphene. The greyscales indicate the energy relative to the Fermi level E_F: Black corresponds to -8.4 eV and white to 8.4 eV. The white lines show the two-dimensional Brillouin zone.

Brillouin zone and defines the plane with $E = E_F$. The bottom of the occupied band is related to the nearest neighbour C-C overlap integral γ_0 and is, for the honeycomb structure, equal to $3\gamma_0$. For graphite, γ_0 can be estimated to be 2.8 ± 0.2 eV [8]. The overlap of the π-orbitals on adjacent atoms of the same layer is the reason for the delocalisation of the π-states and is responsible for the high charge carrier mobility in graphite.

The description of graphene, however, is not sufficient to understand the properties of three-dimensional graphite, in particular regarding the π-states near the Fermi level. The weak interlayer bonding of graphite, which is often incorrectly referred to as Van der Waals bonding, originates from the small overlap of the π-orbitals between atoms of adjacent layers. This creates two types of atoms, since in the ABA stacked graphite, only one half of the atoms, called α-atoms, are positioned above an atom of the adjacent layer. The consequence on the electronic structure is that the degeneracy of the π-bands is lifted.

Figure 1.4 shows band structure calculations for different separations between adjacent graphene layers. The calculation has been performed with the WIEN97 code [9] using the generalised gradient approximation (GGA). The calculation with a large interlayer distance of 8 Å yields the band structure of two-dimensional graphite, i.e. the interaction between adjacent layers can be neglected and the occupied and unoccupied π-bands just touch at the corners of the Brillouin zone.

However, if the interlayer seperation is reduced to the one of graphite (3.35 Å), the interaction between the π-electrons of subsequent layers is observed as a splitting of the bands, which is most pronounced for the π-bands. The marker size in the bandplot of graphite has been chosen to reflect the band character in

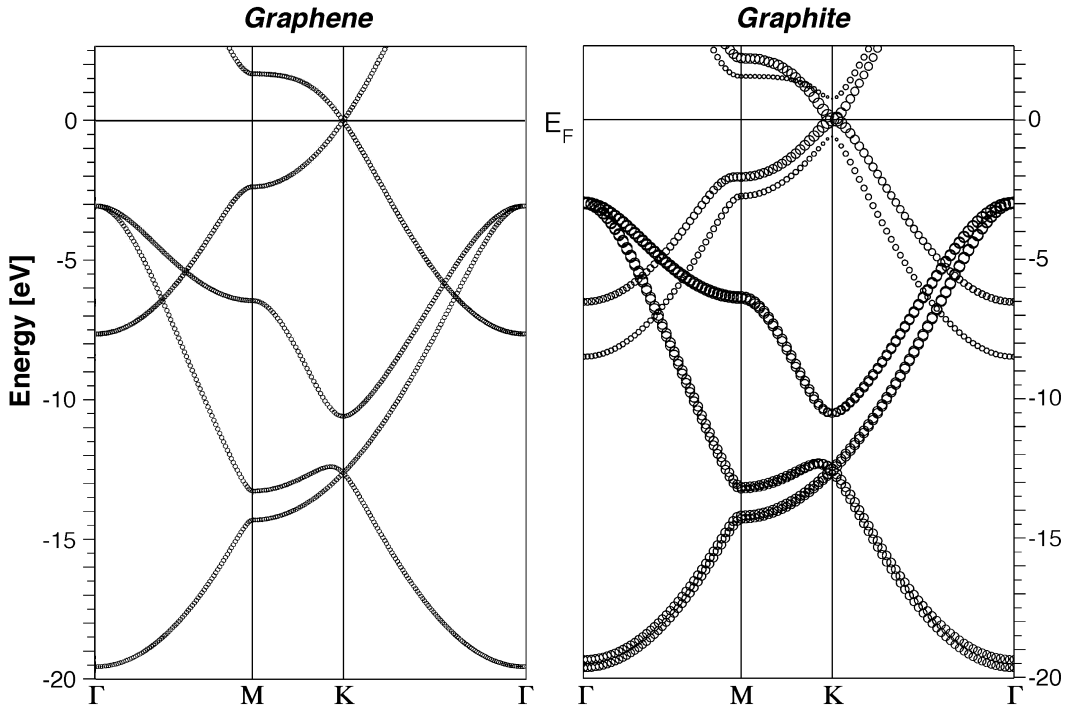

Figure 1.4: Band structure of graphite and graphene as calculated using the WIEN code [9]. The band structure of graphene has been simulated by increasing the interlayer distance $c/2$ of the graphite structure to 8 Å. For graphite, the marker size reflects the band character in terms of the valence charge originating from the β-atom.

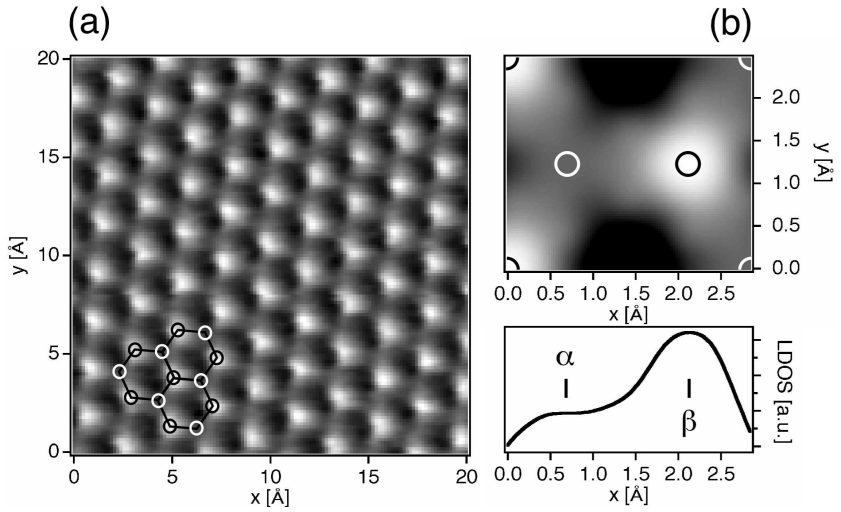

Figure 1.5: (a) Experimental STM current images. The area was scanned in the 'constant height' mode with a tunneling voltage of 0.5 V. (b) LDOS calculated with WIEN [9] in a range of 2.84 Å × 2.46 Å for a height of 4 Å above the suface carbon layer. The density plot comprises states between 0.5 eV binding energy and the Fermi level E_F. Positions of α- and β-atoms are marked by white and black circles, respectively. The line profile shows the calculated LDOS for $y = 1.23$ Å.

terms of the valence charge originating from the β-atom. This representation shows that only the π-electrons related to the β-atoms contribute to the DOS near the Fermi level E_F. The bands related to the α-atom show an energy gap of ∼1.4 eV at the K-point. The remaining bands show a small overlap of 40 meV at the K-points and transform the Fermi surface, consisting of six points for graphene, into six small pockets around the K points for three-dimensional graphite. It is this tiny interaction between the π-electrons of adjacent layers which makes three-dimensional graphite a *semimetal*.

The large asymmetry between the π-band related to the α and the β atoms is also observed in the real space charge distribution. For probes that are sensitive to the local density of states (LDOS) near the E_F, as for instance STM, maxima in the tunneling current are detected exclusively on the β-atoms. An

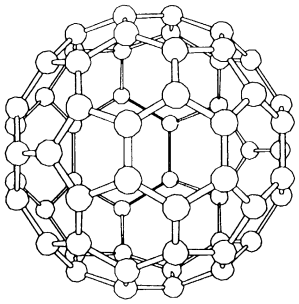

Figure 1.6: Buckminster (C_{60}) fullerene.

experimental current image is shown in Fig. 1.5 which has been recorded with a gap voltage of 0.5 V. Instead of the hexagonal structure expected from the honeycomb arrangement of the carbon atoms in a layer, a trigonal symmetry consisting of maxima in the tunneling current observed on every second atom only is imaged. Figure 1.5 (b) shows the calculation of the LDOS using the WIEN97 code [9]. In order to simulate the surface we used a supercell containing two graphene layers separated by 3.35 Å and 12 Å of empty space. This allows the calculation of the LDOS at a typical STM height of 4 Å above the surface. The results show, that the interlayer interaction results in a very small DOS near E_F that is positioned at the position of the α-atoms. For lower tunneling voltages, i.e. a further restriction on the energy difference to E_F of the states probed in the scan, the asymmetry between α- and β-atoms becoms even more pronounced. The calculated density plot for states having a binding energy of $E_B \leq 150$ meV yields a LDOS on the α-atoms that is even lower than above the center of the hexagon, where no atom resides.

1.2.3 Carbon Fullerenes and Nanotubes

Fullerenes can be viewed as closed networks of sp^2-bonded carbon. The local curvature needed for the closure is induced by the incorporation of pentagons in the atomic arrangement. The experimental discovery of fullerenes occured

in the investigation of unusual infrared emission from large carbon clusters streaming out of red giant carbon stars [10] and the development of a laser vaporisation cluster technique to produce such kind of carbon clusters [11]. According to Euler's theorem, twelve pentagons are required to close a structure. The most stable molecule is C_{60} (Fig. 1.6), where the 60 carbon atoms are identical and are located at the corners of a truncated icosahedron.

Another class of carbon nanostructures related to the fullerenes was discovered in 1991 by S. Iijima [12] and consists of rolled-up grahene sheets, the so-called carbon nanotubes. Depending on the number of shells present in the tube, one refers to single-walled nanotubes (SWNT) or multi-walled nanotubes (MWNT). Typical dimensions of the tubes are one to serveral nanometers in diameter and a length of several hundred nanometer. A direct application of the structural properties of nanotubes is the use of nanotubes as electron field emitters. The high aspect ratio leads to a large local field enhancement factor and lowers the required macroscopic electric field by a factor of a few hundreds [13, 14].

The bandstructure of SWNT can basically be explained by the dispersion relation calculated for graphene. However, one important restriction on the allowed states originates from the periodic boundary conditions in the circumferential direction of the tube. This reduces drastically the number of allowed wavevectors in this direction and leads to the one-dimensionality of the bands, which expresses itself in the appearance of van Hove singularities in the density of states.

Fig. 1.7 (b) shows the band dispersion of graphene as a grey-level plot and the allowed states for a (5,5) SWNT (black lines). This representation of the allowed states shows that the electronic properties of SWNT are directly related to the chirality of the tube. The tubes are metallic if the allowed wavevectors cross the K point of the Brillouin zone or are otherwise semiconducting. Using the description with the wrapping vector (n, m), the tubes are metallic if $n - m = 3i$, i being an integer, or are semiconducting if $n - m \neq 3i$. The energy bandgap of semiconducting tubes decreases with increasing tube diameter according to $E_g = \frac{\gamma_0 a_{C-C}}{d_T}$ [4]. Here, a_{C-C} denotes the nearest-neighbour distance in graphene and d_T the tube diameter which is

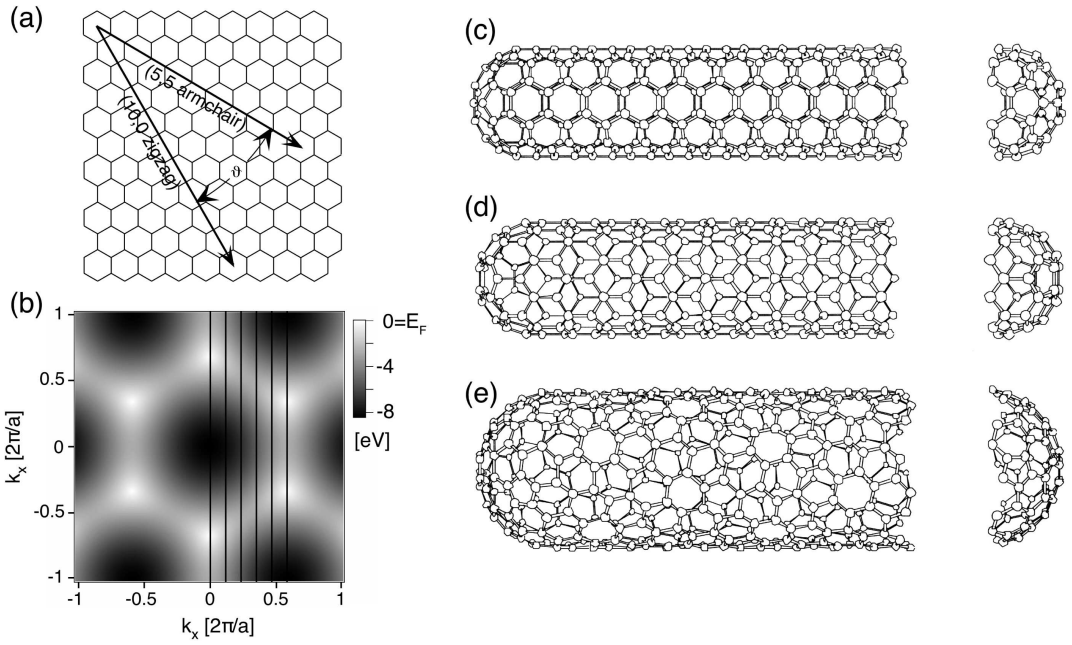

Figure 1.7: (a) Wrapping vectors (n, m) for two SWNT. (b) 2D-band dispersion for graphene [5] with allowed wavevectors for a (5,5) SWNT (black lines). (c)-(e) Armchair tube, zigzag tube, and chiral tube, from Ref. [4].

---

given by $d_T = \sqrt{3}a_{C-C}\sqrt{m^2 + mn + n^2}/\pi$. This leads to a bandgap of 0.34 eV for a typical tube diameter of 1.2 nm.

For metallic tubes, the electronic behaviour is determined by the states near the Fermi level which consist of two degenerate π-bands (Fig. 1.4). These two bands have opposite slopes at the K-points and thus describe two forward- and two backward-moving channels of the delocalised electrons.

Limiting the size of the tube anlong the tube axis results in a further restriction of the allowed wavevectors and replaces the lines in Fig. 1.7(b) by chains of points. Acoordingly, the energy spectrum of the allowed wavevectors becomes discrete and the one-dimensional bands are replaced by molecular

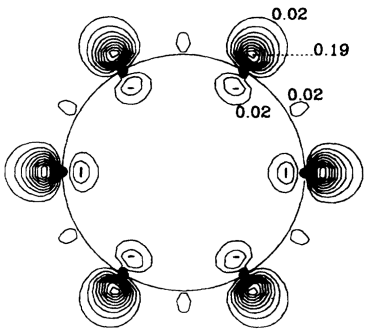

Figure 1.8: Charge density of the curvature induced state at the Fermi level in units of e/(a.u.)^3 for a $(6, 0)$-tube [19].

---

orbitals. These indvidual molecular wavefunctions have been observed [15] using low-temperature STM on a SWNT cut to a length of ∼30 nm.

The unique electronic properties and the low defect density achieved with today's growth techniques make nanotubes a good candidate for the investigation and development of molecular electronics. Among the important works on this road is the realisation of a room temperature single electron transistor, which is based on the local chemical modification of a SWNT [16]. The modified part of the nanotube (∼ 10 nm) acts as a quantum dot with discrete energy levels, whereas the unmodified parts of the tube serve as leads to the dot.

Local modifications on a nanotube, such as structural defects and chemisorption of adatoms induce important modifications in the electronic structure. Such defects can potentially be used to incorporate tunneling junctions [17] and electron scatter centers [18] on a SWNT. We address the question of the local electronic modifications of a sp^2-bonded carbon network containing point defects, such as adsorption sites and atomic vacancies in chapter 4.

For both, carbon nanotubes and fullerenes, the hybridisation of the carbon atoms is generally described with the sp^2-arrangement although the bonds between adjacent atoms are located on a curved surface. This deviation from

planarity, however, leads to some admixture of sp^3-character to the bonding configuration. The curvature in the carbon network can also be regarded as a partial tetrahedrisation of the bonding configuration which depends on the radius of curvature and if the structure is curved only in one dimension (nanotubes) or in two dimensions (fullerenes). Blase *et al.* [19] calculated the bandstructure of SWNT with various tube diameters within the local density approximation (LDA). They found an increasing hybridisation of the π^* and the σ^* for small tubes and a charge distribution (Fig. 1.8) of this state which is not symmetric with respect to the surface containing the carbon atoms. This asymmetry is not consistent with pure π-states and indicates the rehybridisation in highly curved structures such as small diameter nanotubes and C_{60} molecules. This unsaturated sp^3-like orbital which is developed normal to the surface containing the carbon atoms has to be expected to alter the energy barriers for chemisoption of elements. We address this question for the case of the interaction of hydrogen with sp^2-bonded carbon as a function of curvature in chapter 3.

1.2.4 Polycyclic Aromatic Hydrocarbons

Recent years have brough much interest to the class of large organic molecules. Among this vast class of molecules Polycyclic Aromatic Hydrocarbons (PAHs) have attracted particular interest in view of their self-assembly and transport properties [20, 21]. The PAHs consist of an aromatic core of variable size which may be surrounded by functional chains. The packing of these molecules is largely dominated by the π-π interaction between the cores and may be varied by changing the core size. The binding energies between these large molecules are of the order of a typical chemical bond. Figure 1.9 shows the structure of hexa-*peri*-hexabenzocoronene (HBC) which consists of a core of 13 aromatic rings. The solubility of the molecules can be controlled by the chains attached to the HBC core. For instance, alkyl-substituted derivatives of HBC (R=$C_{10}H_{21}$, $C_{12}H_{25}$) show a high solubility and self-assemble into columnar structures for which a high conductivity along the column axis has been observed [22]. This one-dimensional conductivity is related to the overlap of the π-orbitals of adjacent molecules in the columns. In view of potential appli-

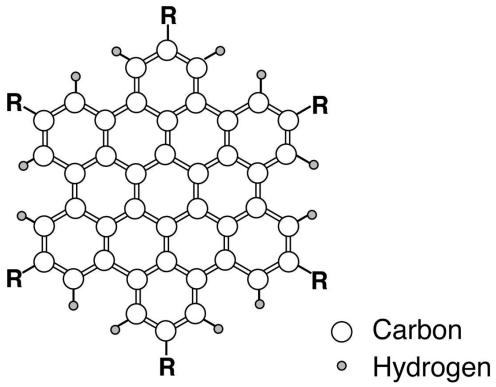

Figure 1.9: Structure of the HBC moledule. *R* represents chains that may be attached to the molecule or hydrogen atoms in the unsubstituted case ($C_{42}H_{18}$).

---

cations the growth with controlled column orientation and separation at solid surfaces would be interesting. We address the question of the growth mode of the insoluble unsubstituted HBC at noble metal surfaces in chapter 5.

References for Chapter 1

[1] I.L. Spain, Chem. Phys. Carbon, **16**, 119 - 304 (1981).

[2] L.S. Pan and D.R. Kania, *Diamond: Electronic Properties and Applications*, Kluwer Academic Publishers, Boston, 1995.

[3] G. Davies, *Properties and Growth of Diamond*, Inspec, (1994).

[4] M.S. Dresselhaus, G. Dresselhaus, and P.C. Eklund, *Science of Fullerenes and Carbon Nanotubes* Academic Press, San Diego, 1996.

[5] P.R. Wallace, Phys. Rev., **71**, 622 (1947).

[6] M.S. Dresselhaus and G. Dresselhaus, Adv. in Phys. **30**, 139 (1981).

[7] S.R.P. Silva, J. Robertson, W. I. Milne, and G.A.J. Amaratunga, *Amorphous Carbon: State of the Art*, World Scientific, Singapore, 1997.

[8] A. Santoni, L.J. Terminello, F.J. Himpsel and T. Takahashi, Appl. Phys. A **52**, 299 (1991).

[9] P. Blaha, K. Schwarz, and J. Luitz, **WIEN97**, Vienna University of Technology 1997. (Improved and updated Unix version of the original copyrighted WIEN-code, which was published by P. Blaha, K. Schwarz, P. Sorantin, and S.B. Trickey, in Comput. Phys. Commun. **59**, 399 1990).

[10] E. Herbig, Astrophys. J. **196**, 129 (1975).

[11] T.G. Dietz, M.A. Duncan, D.E. Powers, and R.E. Smalley, J. Chem. Phys. **74**, 6511 (1981).

[12] S. Iijima, Nature, **354**, 56 (1991).

[13] O. Gröning, *Fieldemission properties of carbon thin films and carbon nanotubes*. Inaugural-Dissertation no **1258**, University of Fribourg (1999).

[14] L. Nilsson, *Microscopic characterization of electron field emission from carbon nanotubes and carbon thin-film electron emitters*. Inaugural-Dissertation no **1337**, University of Fribourg (2001).

[15] S.G. Lemay, J.W. Janssen, M van den Hout, M. Mooij, M.J. Bronikowski, P.A. Willis, R.E. Smalley, L.P. Kouwenhoven, and C. Dekker, Nature **412**, 617 (2001).

[16] J.B. Cui, M. Burghard, and K. Kern, Nano Lett. **2**, 117 (2002).

[17] H. W.Ch. Postma, T. Teepen, Z. Yao, M. Grifoni, and C. Dekker, Science **293**, 76 (2001).

[18] M. Bockrath, W. Kiang, D. Bozovic, J.H. Hafner, C.M. Lieber, M. Tinkham, and H. Park, Science **291**, 283 (2001).

[19] X. Blase, L.X. Benedict, E.L. Shirley, and S.G. Louie, Phys. Rev. Lett. **72**, 1878 (1994).

[20] S. Ito, M. Wehmeier, J.D. Brand, C. Kübel, R. Epsch, J.P. Rabe, and K. Müllen, Chem. Eur. J. **6**, 4327 (2000).

[21] N. Karl and Ch. Günther, Cryst. Res. Technol. **34**, 243 (1999)

[22] A.V. de Craats, J. Warman, A. Fechtenkötters. J.D. Brandt, K. Müllen, Adv. Mater. **11**, 1469 (1999)

Chapter 2

Experimental Techniques

2.1 Scanning Probe Microscopy

In contrast to other microscopy techniques, imaging with scanning probe microscopy (SPM) does not require a complex lens system to collect the emitted or reflected particles (electrons, photons, ...) from the sample. Instead, SPM probes the sample surface via tip-sample interactions on a characteristic area which is defined by the dimensions of the tip apex and the tip-sample separation. This allows a resolution on the lengthscale of the atom if tip-sample separations of a few Å and atomically sharp tips are used.

2.1.1 Scanning Tunneling Microscopy

As suggested by its name, imaging using Scanning Tunneling Microscopy (STM) is based on the quantum mechanical tunneling of electrons between the tip and the sample. The invention of the STM in 1981 by Binnig and Rohrer [1, 2] had a large impact in surface science and opened the door for the imaging and the manipulation of structures on the atomic scale. One considerable breakthrough needed for this microscope was the ability to control the tip-surface separation with picometer resolution which was achieved using piezoelectric transducers.

The required tip-sample separation for low energy electron tunneling is of the order of 3 - 5 Å, the distance where the electron wavefunctions of the tip and the sample start to overlap. Applying a voltage between tip and sample

yields the situation depicted in Fig. 2.1(b). Depending on the sign of the applied gap voltage V_t, electrons will tunnel from the occupied states or into the unoccupied states of the sample [4, 5]. If an equal work function Φ for the sample and the tip are assumed, the tunneling probability for electrons is given by

$$P \propto V_t \cdot \exp(-\sqrt{\Phi} \cdot z) \tag{2.1}$$

where z denotes the tip-sample separation and V_t is the applied gap voltage. For typical metals ($\Phi \simeq 5$ eV), the current is reduced by a factor of ten if the tip is retracted by ~ 1Å. It is this extreme sensitivity which is responsible for the high vertical resolution of (≤ 0.1Å) of the STM.

The usual measurement mode is the *constant current* mode where the distance z is adjusted during the xy-scan in order to maintain a given setpoint current (of the order of 1 nA, Fig. 2.1). Alternatively, the sample is scanned

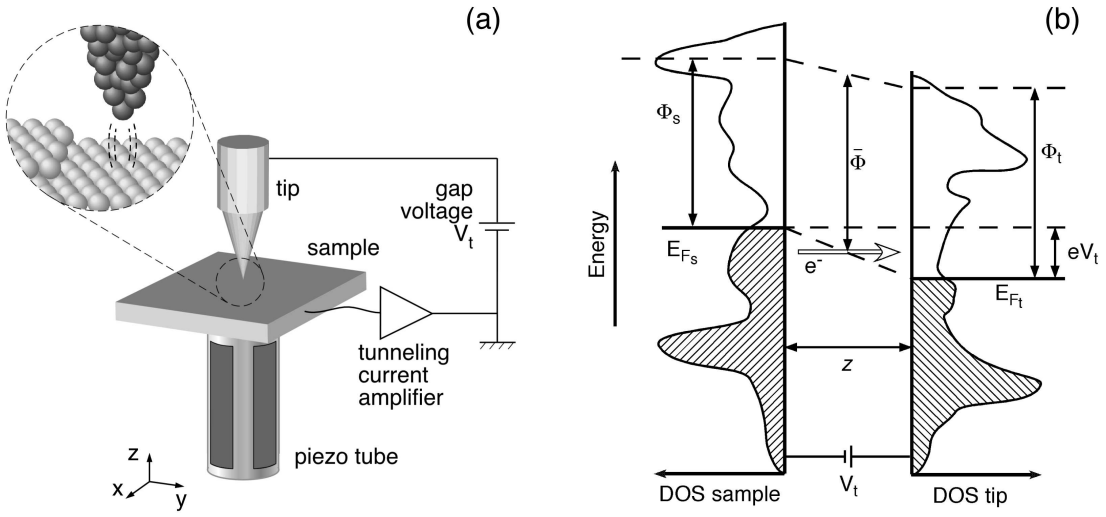

Figure 2.1: (a) Schematic representation of the STM. The piezo tube allows the movement of the sample in three directions and can thus execute both, the xy-scanning and the distance control. The distance is controlled by using the tunneling current as feedback signal. (b) Schematic energy diagram for tunneling junction between the metal tip and a metallic sample. V_t is the applied voltage and z is the tip-sample distance.

in the *constant heigth* mode and the variations in the tunneling current are recorded.

Tersoff [6, 7] has modeled the tunneling junction by assuming a spherical tip with radius R and electronic tip states with s-symmetry. For low gap voltages, the three-dimensional treatment of the problem gives a description of the tunneling current measured at a distance z from the surface, which has the simple form of

$$I \propto \sum_{\mu} |\psi_{\mu}(\mathbf{r_0})|^2 \delta(E_{\mu} - E_F) = \rho_s(\mathbf{r_0}, E_F), \qquad |\mathbf{r_0}| = R + z \tag{2.2}$$

This important result shows that the measured tunneling current at $\mathbf{r_0}$ depends only on the sample wavefunctions and is proportional to the LDOS of the sample at the Fermi level if small bias voltages are applied. Accordingly, measurements in the *constant current* mode image a surface of constant density of states at E_F.

For larger voltages, the above given result can be generalised to

$$I \propto \int_{E_F}^{E_F+V} \rho_s(\mathbf{r_0}, E) dE \tag{2.3}$$

According to this expression, STM probes the occupied or the unoccupied states near the Fermi level depending on the sign of the bias voltage applied to the sample (Fig. 2.1 (b)). However, the expression is not strictly correct, since the energy-dependence of the matrix elements and the tip wave function has been neglected. Nevertheless, Eq. 2.3 is a reasonable approximation for many purposes as long as the bias voltage is considerably smaller than the work function [9]. As an example we show constant current scans on the (7x7) reconstructed Si(111) surface in Fig. 2.2. The data has been recorded with a sample of +1.6 V and -1.5 V, respectively. The comparison of the two scans shows the different distribution of the occupied and unoccupied states within the unit cell of the reconstructed surface. Comparison with the atom positions within the unit cell shows further, that positions with a high LDOS do not necessarliy coincide with atom positions.

A detailed description of the theory of STM and scanning tunneling spectroscopy is given in the book edited by D. Bonnell [9].

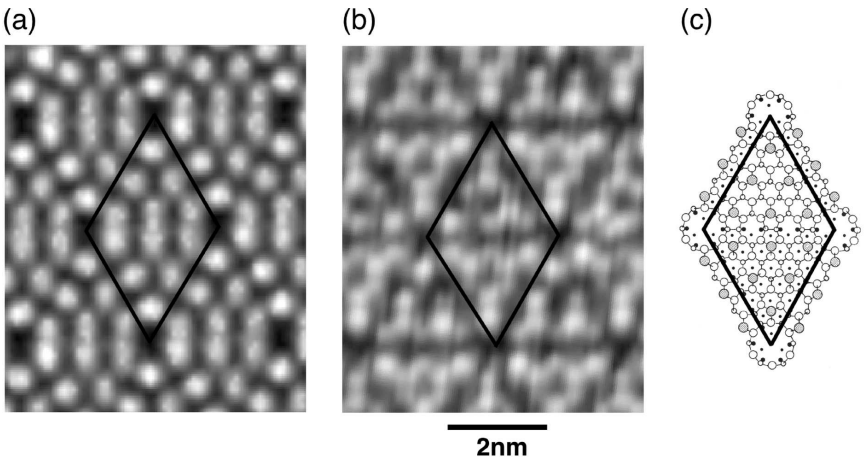

Figure 2.2: Constant current images of the (7 x 7) reconstructed Si(111) surface. (a) Empty state image recorded at a sample bias of -1.6 V and a tunneling current of 0.3 nA. The scan range is 6 nm x 7.4 nm. (b) Occupied state image recorded at 1.5 V and 0.5 nA. (c) Atom arrangement within the unit cell of the reconstructed surface taken from [8]. The size of the circles reflects the distance of the atoms with respect to the top layer (largest circles).

Beside all the advantages of an imaging tool that reveals the local DOS, it brings up the difficulty of the interpretation of the recorded images, since the recorded topography reflects a superposition of the real-space topography and the variations in the LDOS. This applies especially for the imaging of defects, which have in general a low symmetry and for which the topographic structure is usually unknown.

2.1.2 Atomic Force Microscopy

One attempt to overcome this deficiency, is the use of Atomic Force Microscopy (AFM), which detects the forces acting on the tip. AFM is sensitive to the total valence charge and thus reproduces an image which is near the real topographic structure of the surface.

The developement of the AFM was mostly motivated by the desire to build a SPM for insulators that achieves a similar resolution as STM on metals [3]. AFM is based on the same scanning technique as STM (Fig. 2.1 (a)), but uses, instead of the tunneling current, a constant force detected as a deflection of the tip holder (cantilever), as feedback signal. Depending on the tip-sample separation and the tip material, AFM is capable to detect a large variety of short-range and long-range interaction. During the past two decades various scanning probe techniques have been developped including electrostatic force microscopy, magnetic force microscopy and near-field scanning optical microscopy. Very good overviews on the measurement modes of AFM and on the intermolecular forces are given in the books of Bonnell [9] and Israelachevili [10], respectively.

Obviously, if the tip is in contact with the sample, predominantly repulsive forces induced by Pauli exclusion are experienced. This *contact mode* is thus sensitive to the total valence charge and reflects the topography of the sample.

In order to get a complete description of a defect and its influence on the electronic structure of the substrate, the combination of AFM and STM would be desirable. One way to do so, is scanning the surface in the *constant force* mode by using a conductive AFM tip and simultaneously applying a voltage to the tip. This measurement mode allows the separation of structural and electronic information in the way taht the recorded distance variations reflect the surface topography and the variations in the current signal reveal the LDOS.

2.2 Photoelectron Spectroscopy

Photoelectron spectroscopy is nowadays a well established tool for the chemical and structural analysis of the near-surface region of solids. The method is based on the detection of electrons that are emitted into vacuum via the photoelectric effect. The original motivation and the first application of the method, the developement of corrosion resistant materials, are well reflected in its name: Electron Spectroscopy for Chemical Analysis (ESCA) [11]. Beside its important benefits for applied reasearch [12], photoelectron spectroscopy has been applied to fundamental physics [13]. Some of the spectroscopy methods are briefly

reviewed in the following.

X-ray Photoelectron Spectroscopy (XPS) allows the determination of the chemical composition at the surface by exciting core electrons using soft X-rays (50 eV$\leq h\nu \leq$1500 eV) as excitation source. The typcial probe depth of a few tenth of Å is given by the inelastic mean free path $\lambda(E_{kin})$ of the excited photoelectrons which depends on their kinetic energy [14]. Determination of the exact energy of the emitted photoelectrons reveals their 'chemical shift' and provides information on the coordination and the chemical state of the elements. The intensity detected by the energy analyser is given by

$$I \propto n \cdot \sigma \cdot \lambda(E_{kin}) \cdot T(E_{kin}) \cdot cos(\theta) \tag{2.4}$$

where n is the number of atoms per unit area, σ the photoionisation cross section, $T(E_{kin})$ the analyser transmission factor and θ the photoelectron emission angle with respect to the surface normal. Beside the mean free path of the photoelectrons, the instrument-specific analyser transmission has to be known over the entire kinetic energy range in order to allow a quantitative determination of the elemental composition of the surface. We have determined the transmission function for the analyser used in this work (EA125, Omicron) using a method that is independent of the knowledge of the mean free path. The experimental procedure and the results are described in Appendix A.

2.2.1 X-ray Photoelectron Diffraction

In 1970 Siegbahn *et al.* [15] observed enhanced photoelectron emission along certain crystal directions of NaCl (001). Their observation was explained later by Fadley and Bergström [16] by final state elastic scattering effects, which is in general termed Photoelectron Diffraction.

The physical situation is schematically shown in Fig. 2.3 (a). The spherical photoelectron wave is scattered by the neighbouring atoms and the scattered wave interferes with the unscattered wave. Parameters determining the interference are the nearest-neighbour distances, the scattering angle, the atomic type of the scatterer and the relative phase of direct and scattered waves. At kinetic energies above about 500 eV the so-called 'forward-focusing effect' in the directions of nearest-neighbours becomes dominant. This is shown in Fig.

2.3 (b) for photoelectrons of different kinetic energies. In a typical XPD experiment, the photoelectrons have an energy of ~ 1 keV and accordingly, the scattering is dominated by the fordward focusing effect. On metals, this effect often allows a very direct structure determination, since prominent intensity maxima can be directly related to the nearest-neighbour directions. Experimentally, the photoelectron intensities of a selected core level are collected at different emission angles. The angle-scanning of the sample allows the intensity detection in a solid angle of almost 2π above the sample surface [17].

The method has been successfully applied to the structure determination of adlayers and molecules adsorbed on metal surfaces [18–20]. Recording the intensity distribution for different core levels provides the chemically resolved atomic structure around the photoemitter. This has for instance been used as fingerprinting tool to determine the substitution sites of doped High-T_C superconductors [21].

Beside the forward-focusing maxima, further intensity maxima appear due to the interference of the scattered and the unscattered waves (Fig. 2.3(a)). In contrast to the forward focusing maxima which contains just the information

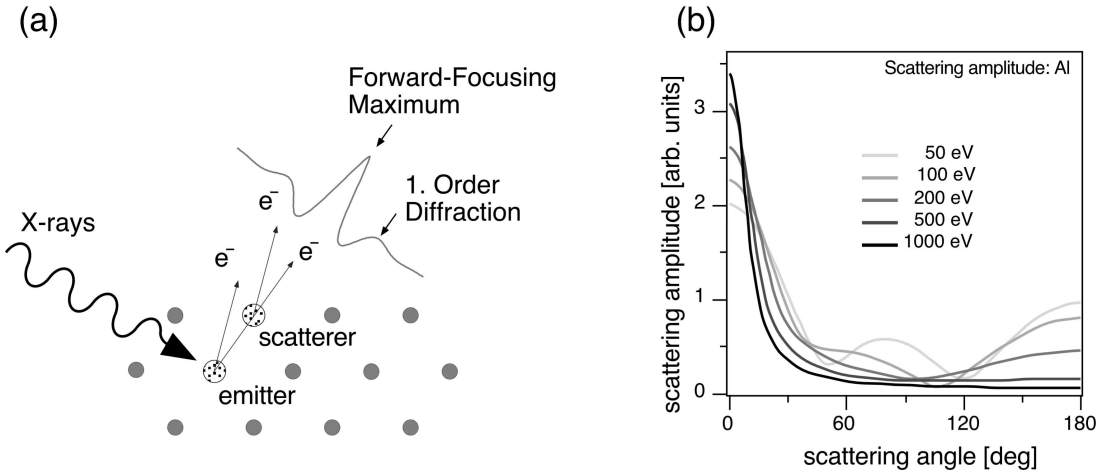

Figure 2.3: (a) Schematic representation of the forward-focusing effect along atom chains and interference between the scattered and unscattered waves. (b) Scattering amplitude for various kinetic energies of the electron.

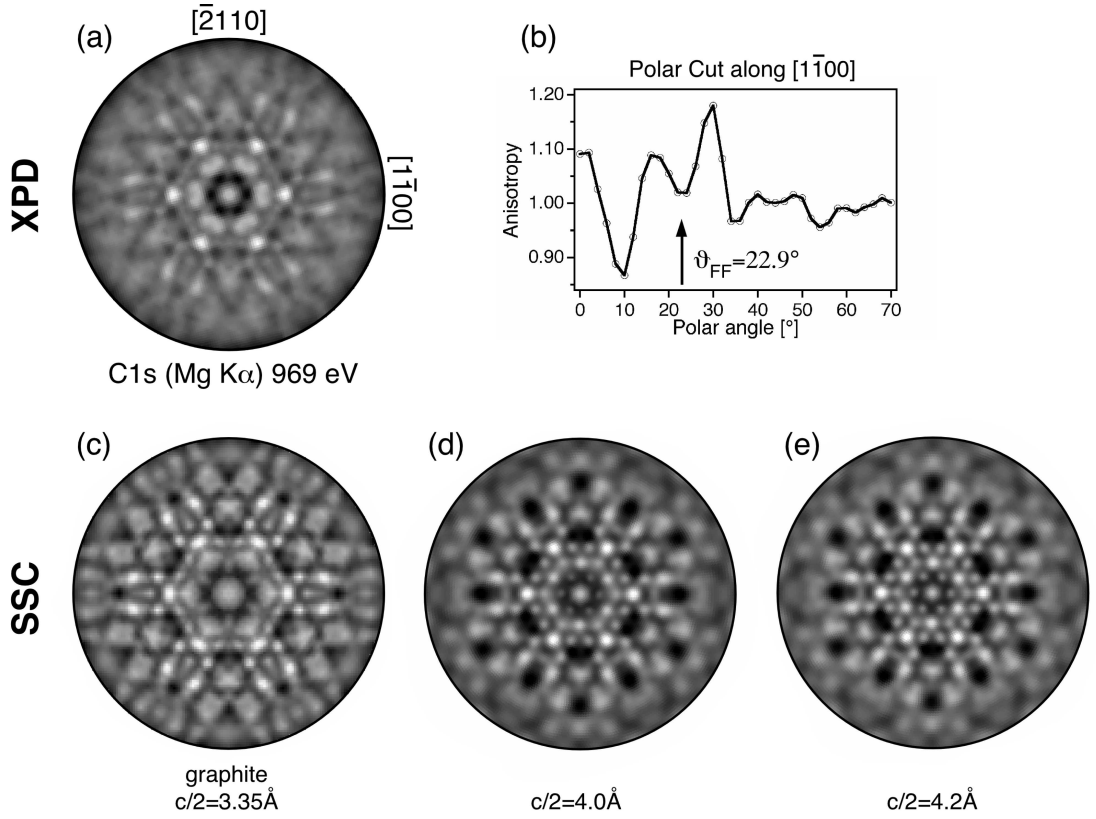

Figure 2.4: (a) XPD pattern of the C1s core level excited using Mg Kα radiation on the graphite (0001) surface. The data is shown in stereographic projection with $\vartheta_{max} = 70°$. The data shown is after background subtraction and is three-fold averaged. The grey-scale represents the detected photoelectron emission with white highest and black lowest intensity. Two directions parallel to the surface are labeled. (b) Polar cut along the [1$\bar{1}$00] direction. The arrow labels the expected forward-focusing direction at 22.9°. (c) SSC calculation of the graphite structure for $E_{kin} =$ 970 eV. (d), (e) Calculations for increased distances between the graphene layers.

---

of the direction of the nearest neighbours, these features are also sensitive to the nearest neighbour distance. In a recent work, Wider *et al.* [22] showed that this information can be used for the real space reconstruction of the nearest

neighbour positions around the emitter. They used a geometric arrangement of the excitation source and the analyser where the forward-focusing effect is largely suppressed. This holographic mode allowed the reconstruction of the atom positions of up to 10 Å from the emitter atom.

In the case, where the intensity maxima cannot be directly attributed to nearest neighbour directions due to interference effects, further efforts are required for the structure determination. For simulation of experimental diffraction patterns, Single Scattering Cluster (SSC) theory is frequently used and has proven to reproduce the experimental data with a rather good agreement [18, 23]. Details on SSC calculations are given in [17, 18, 23].

Graphite is an example where the geometrically determined angles of expected forward-focusing maxima do not coincide with the detected intensity maxima. Figure 2.4 (a) shows an experimental diffraction pattern of a graphite (0001) surface. The outer ring represents data collected at a polar angle of 70° off-normal. The arrow in (b) indicates the direction where an intensity maximum is expected. The large difference between the nearest-neighbour directions and the directions of the intensity maxima indicate, that the diffraction patterns are dominated by interference effects. This is further emphasised by SSC calculations performed for various interlayer distances which leads to the appeareance and disappearance of intensity maxima due to the varying phase shifts between waves scattered at neighbouring atoms.

2.2.2 Angle-Resolved UPS

In order to study the electronic bandstructure of a solid, good resolution in the reciprocal space and in energy are required. Both can be realised by using UV photons for the photoelectron emission [13].

In an Angle-Resolved UPS (ARUPS) experiment one measures the kinetic energy E_{kin}^{vac} of an electron for a given polar angle ϑ_{ext} with respect to the surface normal and an azimuthal angle φ_{ext}. A schematic setup is shown in Fig. 2.5.

For a basic understanding on how the initial state $E_i(\mathbf{k}_i)$ can be determined with the measured quantities ϑ_{ext} and φ_{ext} the following relations are required.

Assuming free electron final states in the solid and in vacuum, one has

$$E_f(\mathbf{k}_f) = \frac{\hbar^2 \mathbf{k}_f^2}{2m} \qquad E_{kin}^{vac} = \frac{\hbar^2 \mathbf{k}_{vac}^2}{2m} \tag{2.5}$$

where E_f and $\mathbf{k}_f$ describe the final state in the solid to which the electron has been excited by a photon of energy $h\nu$. Energy and momentum conservation rules lead to the following expressions:

$$E_f(\mathbf{k}_f) = E_i(\mathbf{k}_i) + h\nu \tag{2.6}$$

$$\mathbf{k}_f = \mathbf{k}_i + \mathbf{k}_{h\nu} + \mathbf{G} \tag{2.7}$$

At photon energies below 50 eV the momentum of the light $\mathbf{k}_{h\nu}$ can be neglected. $\mathbf{G}$ is a reciprocal lattice vector which provides the necessary momentum for the photoelectron emission into vacuum. The momentum contribution of the light $\mathbf{k}_{h\nu}$ can be neglected for photon energies below about 50 eV.

Emission into vacuum is influenced by a potential energy step at the surface barrier which originates from the Coulomb and exchange interactions in the solid that create a mean attractive potential V_0 (the inner potential). This

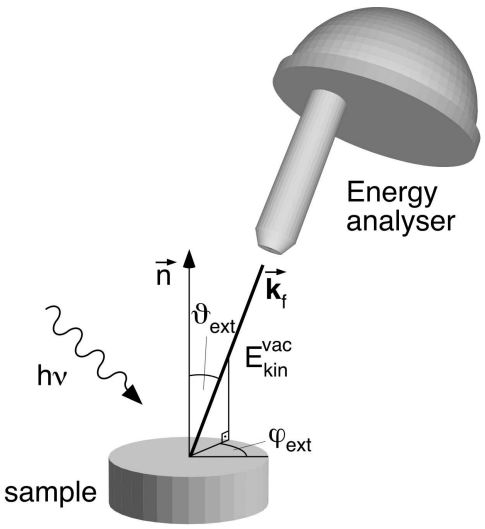

Figure 2.5: Schematic setup for angle scanned photoelectron detection.

potential energy step affects only the component parallel to the surface normal. Accordingly, the determination of $k_\perp$ requires the knowledge of V_0 and is given by

$$k_\perp = \frac{\sqrt{2m(h\nu - \Phi - E_b + V_0)}}{\hbar} \cdot \cos\vartheta \tag{2.8}$$

where ϑ referes to the polar angle in the solid. The relation between the propagation direction inside and outside the solid is described by

$$\sin\vartheta = \sin\vartheta_{ext}\sqrt{\frac{h\nu - \Phi - E_b}{h\nu - \Phi - E_b + V_0}} \tag{2.9}$$

However, the parallel component of the photoelectron wave vector $\mathbf{k}_{||}$ is conserved during emission into vacuum. Using the above given relations we find the exact expression for $k_{||}$:

$$k_{||} = \frac{\sqrt{2m(h\nu - \Phi - E_b)}}{\hbar} \cdot \sin\vartheta_{ext} \tag{2.10}$$

Accordingly, the scanning of the hemisphere above the sample surface allows the measurement of the energy distribution curve $E(\mathbf{k})$ for different $\mathbf{k}$-locations, typically along high-symmetry directions. Alternatively, a large number of angle settings can be scanned with a fixed energy. This allows, for instance, the mapping of the Fermi surface, if the energy is set to E_F [24]. This mode was first been applied by Santoni *et al.*. They used a display type analyser for the mapping of the Fermi surface of graphite [8].

As an example we show the mapping at constant energy on a graphite single crystal in Fig. 2.6. Maps are shown for electrons having 0 eV (Fermi surface), 2.0 eV and 2.8 eV binding energies. The observed high intensity regions can be directly transformed in the momentum distribution for a certain energy using Eq. 2.10. The map recorded for electrons with 0 eV binding energy reveals the Fermi surface of graphite consisting just of the six point-like structures at the K-points. The experimentally determined Fermi wavevector of 1.69 Å^{-1} is in good agreement with the calculated one of $k_F = 4\pi/3a = 1.70\text{Å}^{-1}$. For higher

binding energies the high emission regions are located on triangles around the K-points which grow in diameter with increasing binding energy. The best agreement between the experimentally observed momentum distribution and the dispersion relation calculated within the tight binding approximation is found for a C-C overlap integral of $\gamma_0 = 2.85$ eV.

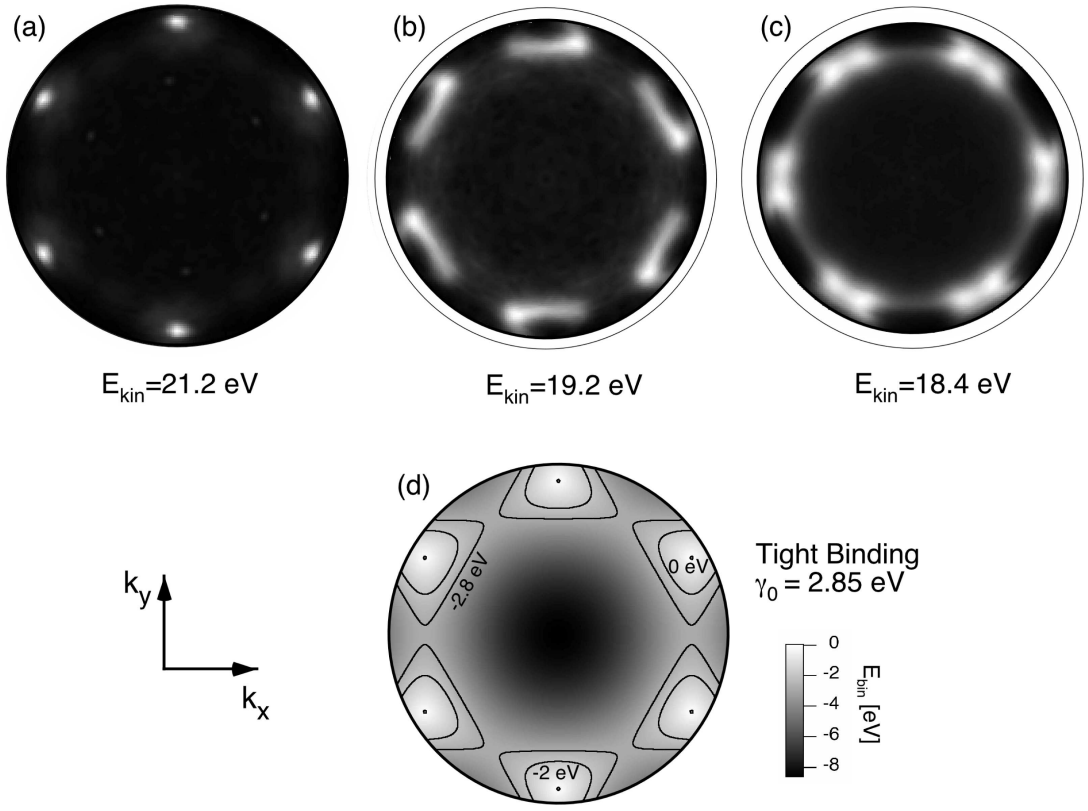

Figure 2.6: Constant energy mapping showing the intensity as function of $\mathbf{k}_{||}$ for various energies. Photoelectrons have been excited using He-I radiation (21.2 eV). All maps were recorded with $\vartheta_{max} = 60°$. The outer circle corresponds to $k_{||} = 1.83\text{Å}^{-1}$. (a) Fermi surface ($E_b$=0 eV). (b) E_b=2 eV. (c) E_b=2.8 eV. (d) Band dispersion calculated within the tight binding approximation [5] with $\gamma_0 = 2.85$ eV. Contour lines are shown for the energies measured in (a)-(c).

References for Chapter 2

[1] G. Binnig and H. Rohrer, Helv. Phys. Acta **55**, 726 (1982).

[2] G. Binnig and H. Rohrer, Rev. Mod. Phys. **59**, 615 (1987).

[3] G.Binnig, C.F. Quate, and Ch. Gerber, Phys. Rev. Lett. **56**, 930 (1986).

[4] I. Hwang, R. Lo, and T.T. Tsong, J. Vac. Sci. Technol. A **16**, 2632 (1998).

[5] Ph. Ebert, B. Engels, P. Richard, K. Schroeder, S. Blügel, C. Domke, M. Heinrich, and K. Urban, Phys. Rev. Lett. **77**, 2997 (1996).

[6] J. Tersoff and D.R. Hamann, Phys. Rev. Lett. **50**, 1998 (1983).

[7] J. Tersoff and D.R. Hamann, Phys. Rev. B **31**, 805 (1985).

[8] K. Takayanagi, Y. Tanishiro, M. Takahashi, H. Motoyoshi, and K. Yagi, J. Vac. Sci. Technol. **A3**, 1502 (1985).

[9] D. Bonnell, *Scanning Probe Microscopy and Spectroscopy*, Wiley-VCH, New York (2001).

[10] J.N. Israelachvili, *Intermoleclar and Surface Forces*, Academic Press, New York (1992).

[11] K. Siegbahn *et al.*, *ESCA: Atomic, Molecular and Solid State Structure Studied by Means of Electron Spectroscopy*, Almqvist and Wiksells, Uppsala (1967).

[12] D. Briggs and M.P. Seah, *Practical Surface Analysis*, Second Edition, Wiley, Chichester (1994).

[13] S. Hüfner, *Photoelectron Spectroscopy*, Springer Series in Solid State Sciences **82**, Springer (1995).

[14] M.P. Seah and W.A. Dench, Surf. Int. Anal. **1**, 2 (1979).

[15] K. Siegbahn, U. Gelius, H. Siegbahn and E. Oslon, Phys. Lett. **32a**, 221 (1970).

[16] C.S. Fadley and S.Å.L. Bergström, Phys. Rev. Lett. **5**, 375 (1971).

[17] J. Osterwalder, T. Greber, A. Stuck, and L. Schlapbach, Phys. Rev. B **44**, 13764 (1993).

[18] R. Fasel, PhD thesis, University of Fribourg (1996).

[19] R. Fasel, P. Aebi, L. Schlapbach, and J. Osterwalder, Phys. Rev. B **52**, R2313 (1995).

[20] R. Fasel, P. Aebi, R.G. Agostino, D. Naumovic, J. Osterwalder, A. Santaniello, and L. Schlapbach, Phys. Rev. Lett. **76**, 4733 (1996).

[21] T. Pillo, J. Hayoz, P. Schwaller, H. Berger, P. Aebi, and L. Schlapbach, Appl. Phys. Lett. **75**, 1550 (1999).

[22] J. Wider, F. Baumberger, M. Sambi, R. gotter, A. Verdini, F. Bruno, D. Cvetko, A. Morgante, T. Greber, and J. Osterwalder, Phys. Rev. Lett. **86**, 2337 (2001).

[23] C.S. Fadley, in *Synchrotron Radiation Research: Advances in Surface Science*, edited by R.Z. Bachrach, Plenum, New York (1989).

[24] P. Aebi, J. Osterwalder, R. Fasel, D. Naumovic, L. Schlapbach, Surf. Sci. **307-309**, 917 (1993).

Chapter 3

Chemisorption of Hydrogen on sp^2-bonded Carbon

In this chapter the results on the interaction of hydrogen with sp^2-bonded carbon networks are presented. Since the local modification of the electronic structure of sp^2-bonded carbon is the main issue of this work, we are mainly interested in hydrogen adsorption where the hydrogen atom chemically binds to the carbon network. This type of adsorption is characterised by a charge transfer between the adsorbate (atom or molecule) and the substrate, called *chemisorption*. This is in contrast to *physisorption*, where the adsorbate is bound to the surface by van der Waals interactions and only a very low charge transfer occurs.

The theoretical works of Sha and Jeloaica (see Ref. [8] and [9] of the following article) showed that a stable bond between hydrogen and graphitic surfaces is only possible with the hydrogen atom located in the on-top position of a carbon atom. This process is accompanied by a pull-out of the now four-fold coordinated carbon atom and results in a local rehybridisation to a sp^3-configuration.

The following article focusses on the influence of the local curvature of the sp^2-bonded carbon network on the chemisorption of hydrogen.

3.1 Hydrogen adsorption on sp^2-bonded carbon: Influence of the local curvature

P. Ruffieux[1,], O. Gröning[1,2], M. Bielmann[1], P. Mauron[1], L. Schlapbach[1,2] and P. Gröning[1]

[1] *Physics Department, University of Fribourg, Pérolles, CH-1700 Fribourg, Switzerland*

[2] *Swiss Federal Laboratories for Materials Testing and Research, Überlandstrasse 129, 8600 Dübendorf, Switzerland*

accepted for publication in *Phys. Rev. B*

The interaction of atomic hydrogen and low-energy hydrogen ions with sp^2-bonded carbon is investigated on the surfaces of C_{60} multilayer films, single-walled carbon nanotubes and graphite (0001). These three materials have been chosen to represent sp^2-bonded carbon networks with different local curvatures and closed surfaces (i.e. no dangling bonds). Chemisorption of hydrogen on these surfaces reduces emission from photoemission features associated with the π-electrons and leads to a lowering of the work function up to 1.3 eV. It is found that the energy barrier for the hydrogen adsorption decreases with increasing local curvature of the carbon surface. Whereas in the case of C_{60} and single-walled carbon nanotubes, hydrogen adsorption can be achieved by exposure to atomic hydrogen, the hydrogen adsorption on

graphite (0001) requires H^+ ions of low kinetic energy ($\sim$1 eV). On all three materials, the adsorption energy barrier is found to increase with coverage. Accordingly, hydrogen chemisorption saturates at coverages which depend on the local curvature of the sample and the form of hydrogen (i.e. atomic or ionic) used for the treatment.

3.1.1 Introduction

Adsorbates, topological defects, and atomic vacancies influence many physical properties of solids and modify the electronic structure, particularly for nano-sized systems [1–3]. Scanning tunneling microscopy has been used to image the long-range (∼6 nm) modifications in the electronic structure of sp^2-bonded carbon networks caused by hydrogen adsorption sites, atomic vacancies and structural defects [4–7]. Recently, defects acting as tunnel barriers or as electron scatterers have been used for the realisation of electronic devices on single carbon nanotubes [1, 3]. Chemisorption of hydrogen on sp^2-bonded carbon is an interesting candidate for the local modification of the electronic structure since it leads to a local rehybridisation from sp^2 to sp^3 of the carbon network.

Additional interest in the interaction of hydrogen with graphitic surfaces originates from the astrophysical community. Interstellar dust particles con-

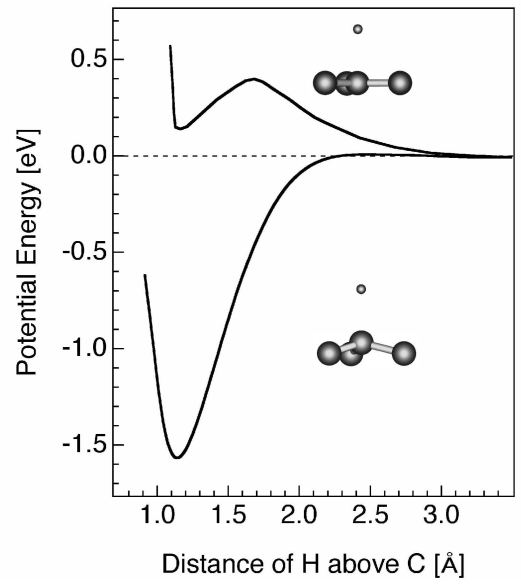

Figure 3.1: Interaction potential as a function of hydrogen-substrate distance as calculated by Sha *et al.* [9] for top site adsorption. The upper curve shows the result for flat geometry. The lower curve shows the potential for a protruded (0.36 Å) carbon atom.

taining graphite are thought to play a catalytic role for the H_2 formation from atomic hydrogen in interstellar space. The yield of different recombination mechanisms strongly depends on the binding energy, the mobility and the potential barriers of hydrogen atoms on graphitic surfaces and has therefore led to several theoretical investigations of the hydrogen-graphite system [8, 9].

The chemical binding of hydrogen to an sp^2-bonded carbon network requires a local rehybridisation from sp^2 to sp^3 and has therefore a rather large adsorption energy barrier for a strictly planar sp^2-bonded carbon network. Figure 3.1 shows the calculated potential energy for a hydrogen atom approaching a graphite surface where all carbon atoms are fixed to positions in the same plane and further for a gaphite surface where one carbon atom is fixed at 0.36 Å above the plane defined by its neighbours, as presented by Sha *et al.* [9]. The almost complete reduction of the adsorption energy barrier for the carbon atom raised by 0.36 Å shows the strong dependence of the energy barrier on the local tetrahedresation, i.e. the admixture of sp^3-character to the sp^2-configuration. Starting from these considerations, the adsorption energy barrier should strongly depend on local deviations from planarity of sp^2-bonded structures. More precisly, the adsorption energy barrier is expected to be lower for convex structures due to an increased sp^3-character introduced by the local curvature.

In this work, we investigated the interaction of atomic hydrogen with sp^2 bonded carbon as a function of the local curvature of the graphitic network. In order to cover a large range of curvature, we chose graphite (0001), single-walled carbon nanotubes (SWNT), and C_{60} fullerenes as substrates. The radius of curvature ranges from $r = \infty$ for graphite to $r = 3.55$Å for C_{60}.

The paper is organised as follows. Details on the sample preparation and on the hydrogen sources used for the treatments are given in the experimental section. In the following section we first discuss the results of the individual samples followed by a discussion of the interaction of hydrogen with sp^2-bonded carbon from the point of view of the local curvature of the samples.

3.1.2 Experimental

Experiments were performed in an OMICRON photoelectron spectrometer modified for motorised sequential angle-scanning data acquisition having a base pressure in the range of $5 \cdot 10^{-11}$ mbar. The analysis part is equipped with a twin-anode X-ray source (Mg$K\alpha$, $h\nu$ = 1253.6 eV; Al$K\alpha$, $h\nu$ = 1486.7 eV) for X-ray photoelectron spectroscopy (XPS) and a He discharge lamp (He I: $h\nu$ = 21.2 eV; He II: $h\nu$ = 40.8 eV) for ultraviolet photoelectron spectroscopy (UPS). The connected preparation chamber has been extended with an electron cyclotron resonance (ECR) microwave plasma source and an atomic hydrogen source.

Typical plasma treatments were conducted at a hydrogen pressure of 10^{-2} mbar and a microwave power of 60 W with the sample positioned at a distance of about 6 cm from the ECR-plasma region. The ion energy distribution has been determined using an electrostatical analyzer [10,11]. Spectra taken under the conditions used in the following experiments show that 85% of the hydrogen ions are comprised in a narrow energy region around 1 eV and the maximum detected energy is $\sim$ 16 eV. A typical ion flux at the sample position is of the order of $2 \cdot 10^{13}$ $s^{-1}cm^{-2}$.

The atomic hydrogen source has been built with the design proposed by Bischler *et al.* [12] where the hydrogen molecules are dissociated in a heated tungsten tube (1700° C), through which the hydrogen is dosed onto the sample. The design enables high dissociation efficencies of about 50% (at 1700°C) and allows fluxes of atomic hydrogen of $\sim 10^{14}$ $s^{-1}cm^{-2}$ at the sample position with a background pressure of $3 \cdot 10^{-8}$ mbar.

The C_{60} film ($\sim$40 Å) has been grown on a clean and well ordered Cu(111) surface by evaporation from a resistively heated stainless steel crucible. The film has been judged well ordered based on low-energy electron diffraction (LEED).

For the investigations on SWNT we used bucky paper samples that were produced out of commercially available SWNT (Tubes@Rice, Carbon Nanotechnologies Inc.). Samples were cleaned in situ by heating to 800° C for several hours. The cleanness of the samples was checked with XPS revealing contamination free (<1 at%) surfaces. Raman analysis of the nanotube sam-

ples has been performed on a commercial microspectrometer (Labram, Dilor) under ambient conditions using a green excitation laser (514.5 nm).

The single-crystal graphite sample (C(0001)) has been cleaved under UHV conditions and heated to 800° C for several hours. The surface has been judged clean and well ordered based on XPS and LEED measurements.

3.1.3 Results and Discussion

3.1.3.1 H/C_{60}

Figure 3.2 shows a series of valence band spectra of a C_{60} multilayer film taken for different H_2 plasma treatment times. Spectra were measured on a 40Å mulilayer film on Cu(111) using He II radiation (40.8 eV) and normalised to have the same integrated intensity with respect to the range of 0 - 17 eV binding energy. The energy transferred from the hydrogen ions to the C_{60} molecules is limited to a level that is low enough to prevent molecule desorption during plasma treatments, as has been checked with XPS where no film thickness variation was detected.

The bottom curve shows the valence band of the untreated film with the highest occupied orbital (HOMO) located at 2.3 eV. The HOMO and the HOMO-1, labeled 1 and 2, are pure π orbitals [15]. They have degeneracies of 10 and 18, respectively, and are thus occupied by 28 eletrons. States with binding energies >4 eV are of mixed $\sigma - \pi$ character.

Exposing the C_{60} multilayer film to H_2 plasma results in a marked intensity reduction on the features labeled 1 and 2. At the same time the spectral features shift by up to 0.9 eV (feature 4). The observation of features shifted in the opposite direction indicates, that the shifts are not due to a Fermi level shift, i.e. due to doping of the film. The strongest increase in intensity is observed at a binding energy of ∼10 eV.

The intensity reduction on the two highest occupied orbitals and the intensity gain on states with higher binding energies indicates the conversion of delocalised π-states to C-H bond states with σ-character, which have a binding energy of ∼10 eV. [16, 17] The intensity reduction gives a measure of how many of the 28 π-electrons contained in the two highest molecular orbitals

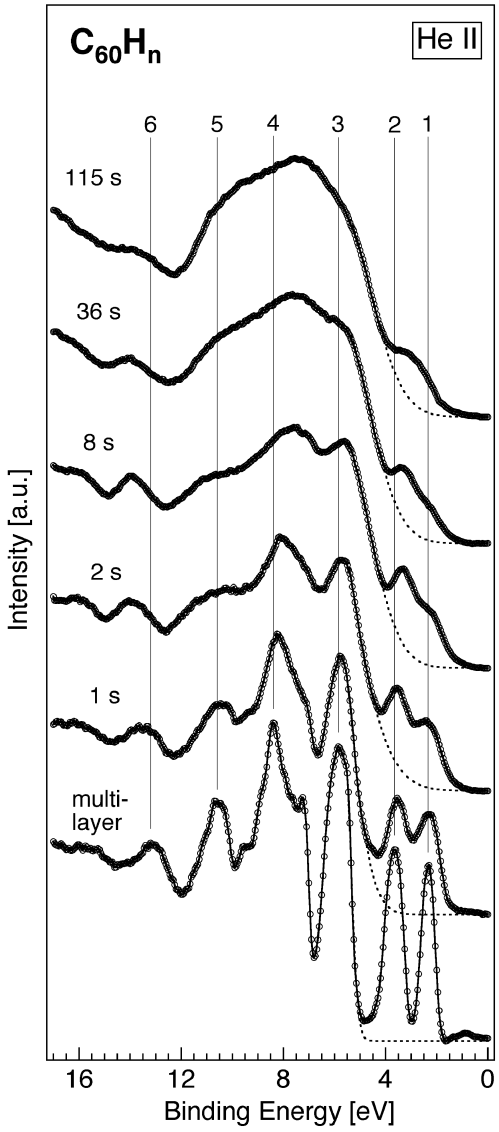

Figure 3.2: Series of valence band spectra for different H_2 plasma treatment times measured using He II radiation (40.8 eV) and an energy resolution of 200 meV. The valence band spectra are normalised to the integrated intensity between 0 and 17 eV binding energy and are displayed with an offset. The background below the features 1 and 2 has been determined by fitting a gauss tail to the feature 3.

are converted to lower lying C-H bonds. The maximum reduction of intensity observed on the π-derived states is 73% (intensity determination after background substraction) indicating the conversion of $\sim$20 π-electrons. However, this estimation does not take into account the conversion of lower lying π-states. Assuming a similar reduction as on the pure π-states results in a conversion of $\sim$44 π-electrons in all. This indicates a somewhat higher degree of hydro-

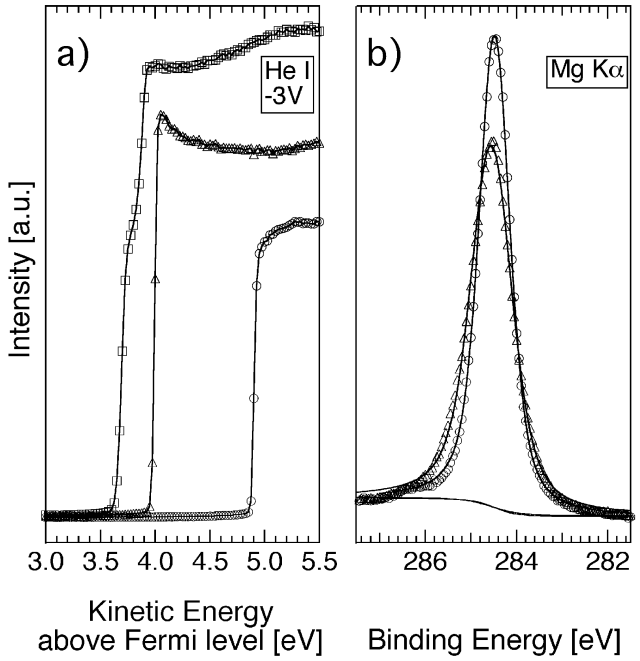

Figure 3.3: (a) Low energy cutoff of the valence band of C_{60} measured with He I radiation (21.2 eV) and an energy resolution of 30 meV for the untreated film (circles), after 36 s (triangles) and 115 s (squares) plasma treatment. The sample was biased to -3 V in order to overcome the work function of the electron analyzer. The energy scale has been corrected for the applied sample bias and displays the energy with respect to the Fermi level. The work fuction has been determined by taking the intersection of the intensity cutoff with the energy axis at zero intensity. (b) C1s core level spectra excited with MgKα measured before (circles) and after 36 s (triangles) H_2 plasma. Spectra were recorded in normal emission and have been normalized to total intensity after background substraction.

genation as has been synthesised via a Birch reduction, yielding $C_{60}H_{36}$ [13]. Theoretical results show that $C_{60}H_{36}$ and $C_{60}H_{48}$ are very stable molecules [18]. Further hydrogenation is energetically unfavourable due to the increased stress in the molecule induced by the sp^2 to sp^3 rehybridisation. Another limiting factor may be stress induced by the expected lattice expansion when hydrogen is adsorbed on the fullerenes, since in this experiment hydrogenation is done on a solid film and not on free molecules.

Hydrogenation of the C_{60} films results in an important lowering of the work function, as seen on the position of the low-energy cutoff of the valence band spectrum (Fig. 3.3a). For the longest treatment time, the work function amounts to 3.6 eV, which signifies a drastic lowering by 1.3 eV compared to the as deposited C_{60} film. The lower work function indicates a change in the surface dipole originating from the polar C-H bond. Since hydrogen atoms are adsorbed on the outside of the fullerene cage and carbon is the more electronegative element, a dipole layer is formed at the surface with the positive charge on the vacuum side. This lowering of the work function induced by hydrogen chemisorption has been observed on other carbon allotropes and is in particular responsible for the negative electron affinity at diamond surfaces [4, 19].

The main change observed in the XPS study is an increasing line width of the C1s line upon hydrogen uptake in the C_{60} film. Figure 3.3(b) shows the spectrum of the C1s core level for the C_{60} multilayer film before and after 36 s of H_2 plasma treatment. The line broadens to higher binding energies resulting in an increase of the full width at half maximum (FWHM) from 0.8 eV to 1.1 eV and a shift of the peak position from 284.48 eV to 284.55 eV, as determined from a fit to the data. This contribution at higher binding energies is known to be the C-H component, although electronegativity arguments would yield a shift to the opposite direction, since carbon is the more electronegative element. The shift to higher binding energies has to be explained by a different relaxation energy of the differently hybridised carbon atoms, as has been shown for different hydrocarbon systems [20–22]. Part of the broadening may also be due to the larger depth that is probed by XPS ($\sim$50Å) compared to the UPS study, which is sensitve to the outermost molecule layer only.

The same series of measurements has been performed on C_{60} films that

were exposed to atomic hydrogen. The second spectrum in Fig. 3.4 shows the valence band of the C_{60} multilayer film for a treatment level, where the hydrogen uptake has saturated. The intensity on the pure π-states is lowered to 47% of the value for the untreated sample, which is in agreement with the

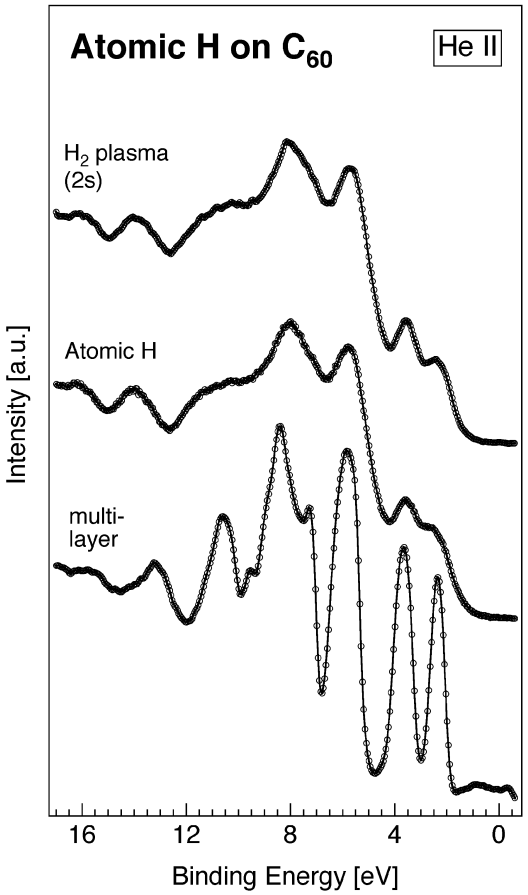

Figure 3.4: Valence band spectra of the C_{60} film after different treatments. The spectrum at the bottom shows the valence band for the untreated film. The second spectrum shows the spectrum for the atomic hydrogen treated film after a treatment time of where hydrogen chemisorption has reached its saturation value. The top spectrum shows the valence band after a H_2 plasma treatment of 2s, yielding similar changes as for the saturation coverage of atomic hydrogen.

results presented by Ohno *et.al* [23]. This indicates a conversion of ∼28 π-states if a similar reduction on the lower lying π-states is assumed, as discussed above. The lowering of the work function amounts to ∼0.8 eV. Comparison with the valence band spectrum of the C_{60} film that was exposed to H_2 plasma shows that the evolution of spectral features upon hydrogenation is identical for plasma and atomic hydrogen treatments. This further confirms, that damage induced by hydrogen ions can be neglected at least for plasma treatments up to this level.

Since H_2 plasma contains both reactive species, atomic hydrogen and hydrogen ions, the higher level of hydrogenation achieved with the plasma can be attributed to the presence of the hydrogen ions. At the level where hydrogen uptake saturates for treatments with atomic hydrogen, the hydrogen ions still see an adsorption energy barrier that is sufficiently low to allow further hydrogenation of the C_{60} film.

3.1.3.2 H/SWNT

SWNT can be looked at as rolled up graphene sheets resulting in tubules with diameters of $d_T \geq 4$ Å [24] where the electronic properties approach those of graphene with increasing diameter. States with a binding energy less than ∼4 eV are of pure π character, whereas states in the range of 4 to 11 eV have mixed σ-π character and states having binding energies larger than ∼ 11 eV are pure σ-states.

We have used Raman spectroscopy to determine the diameter of the SWNT smaples. It has been shown that the position of the first spectral feature in the Raman spectrum, the radial breathing mode, observed between 140 and 220 cm^{-1}, is unique for SWNT [25]. For the laser line used in this work (514.5 nm), the wave number ν of the radial breathing mode is, to a good approximation, related to the tube diameter d_T as $1/d_T = \nu/234$, and thus allows the determination of the mean tube diameter of the sample [25]. Analysis of the SWNT (Tubes@Rice) used for this study revealed a mean tube diameter of $d_T \simeq 1.2$ nm.

Figure 3.5 displays valence band spectra of the SWNT film measured using He II radiation (40.8 eV). The prominent spectral features observed for the

untreated SWNT film are similar to those observed in angle-integrated measurements on graphite. The state at ~ 2.5 eV binding energy is a pure π-state and thus represents a feature whose intensity is supposed to be lowered in in-

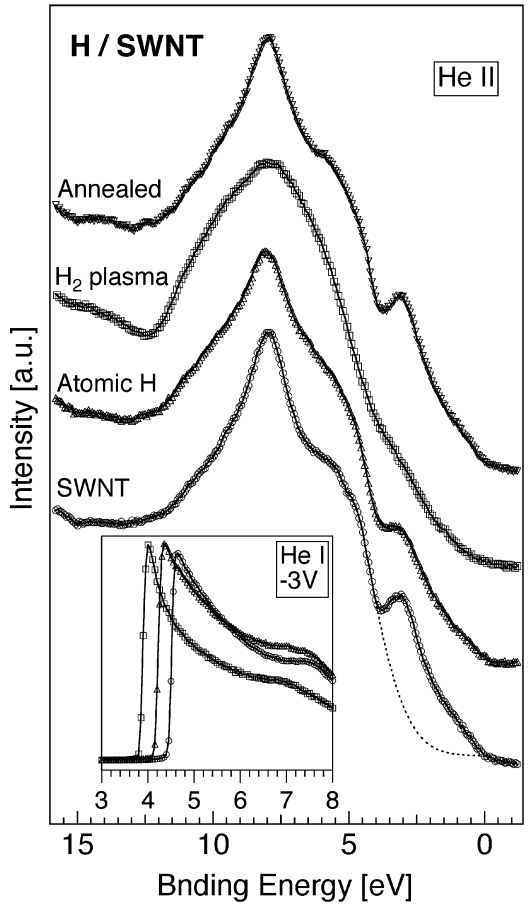

Figure 3.5: Valence band spectra of SWNT's for the untreated (circles), atomic hydrogen treated (triangles) and plasma treated (squares) sample using He II radiation (40.8 eV). Spectra have been offsetted for better visibility. The intensity on the π-derived states has been determined after substraction of a gauss-background (dotted line). The inset shows the low energy cutoff of the valence band as a function of kinetic energy rel. to the Fermi level. These spectra have been measured with a sample bias of -3V.

tensity if hydrogen is chemically bond to the tube walls since in that case, as discussed above, the delocalised π-states are transformed to lower lying C-H states. In contrast to this, the passivation of dangling bonds of carbon atoms at the edge of graphene sheets, as for open tubes or tube fragments, with hydrogen does not affect the π-states, since this C-H bond state is a σ-state and does not mix with the π-states [26]. The work function of the untreated film is 4.4 eV, as determined from the low energy cutoff of the He I spectrum.

In order to be able to distinguish between hydrogenation induced by atomic hydrogen and hydrogen ions, we first treated the film with atomic hydrogen. The second spectrum in Fig. 3.5 shows the valence band after 120 s of treatment with atomic hydrogen. At this level of atomic hydrogen treatment the reduction on the intensity of the π-derived states has achieved its saturation value of $\sim$22% and the work function has been lowered by 0.3 eV to 4.1eV (inset of Fig. 3.5). This shows a significant hydrogen uptake on this type of tubes, but remains significantly below the value observed for the atomic hydrogen treatment of the C_{60} film (47%).

Further hydrogenation of the SWNT film could be achieved by H_2 plasma treatment. This is manifested by a further reduction of the spectral weight of states with binding energies < 4 eV. Hydrogen uptake seems to saturate after 200 s of plasma treatment when the intensity of the π-derived states has been reduced to $\sim$50 % of its original value, i.e. half of the delocalised π-states have been transformed to lower lying C-H states resulting in a coverage of $\theta \simeq 0.5$ of chemisorbed hydrogen. Similar to the C_{60}-film, these new states are located at $\sim$10 eV binding energy. This further hydrogen uptake results in a work function of 3.8 eV, which is 0.6 eV lower than for the untreated film. However, an uncertainty remains on the hydrogen coverage of the nanotubes, since these samples are known to contain small amounts of amorphous carbon residues, which may contribute to the spectral weight on the π-states.

XPS analysis on the films shows a similar behaviour as observed on the C_{60} film. Hydrogen uptake gives rise to a new component at higher binding energies, leading to an increase of the FWHM from 1.05 eV to 1.14 eV for the sample exposed to atomic hydrogen.

Heating the samples to $\sim$ 800° C restores the original valence band and

the work function of 4.4 eV, indicating that all hydrogen has desorbed at this temperature and that damage on the tubes induced by the most energetic hydrogen ions is limited to a low level.

Lee *et al.* predicted two stable configurations of hydrogenated SWNT with a coverage of $\theta = 1$ based on a density functional calculation [27,28]. The *zigzag* type has the hydrogen atoms alternatively chemisorbed on the inside and on the outside of the tube wall and has a higher stability than the *arch* type, which has all the hydrogen atoms at the exterior of the tube wall. The superior stability of the *zigzag* type is due to a more pronounced tetrahedrisation that is allowed by the alternating position of the hydrogen atoms with respect to the tube wall.

The observed lowering of the work function does not speak in favour of the *zigzag* geometry since for this adsorbate configuration, no pronounced change of the surface dipole is expected due to the position of the hyrogen atoms, which adsorbe alternatively on the inside and the outside of the tube wall. On the other hand, chemisorption on the outside of the tube wall agrees well with the observed change in surface dipole. However, the coverage seems to be limited to $\theta \simeq 0.5$ even with hydrogen ions having an energy of ~ 1 eV. A possible explanation of this limiting behaviour is an adsorption energy barrier that increases with hydrogen coverage. This can be understood by taking into account the pull-out of the carbon atom induced by the C-H bond formation [9]. This results in an increased energy barrier for hydrogen chemisorption on the neighbour atoms, since the later ones find themself in a depressed position. If this larger adsorption energy barrier is too high for the bond formation, the maximum coverage will be limited to $\theta = 0.5$ with hydrogen chemisorbed to every second carbon atom.

3.1.3.3 H/Graphite

Figure 3.6 shows UV photoemission spectra of the C(0001) surface taken for different polar emission angles ϑ along the $\Gamma - \mathrm{K}$ of the Brioullin zone direction using He I radiation (21.2 eV). The angle-resolved measurements allow a clear attribution of the photoelectron features to the various valence bands of graphite. Spectra in the $\Gamma - \mathrm{K}$ direction are dominated by two dispersing

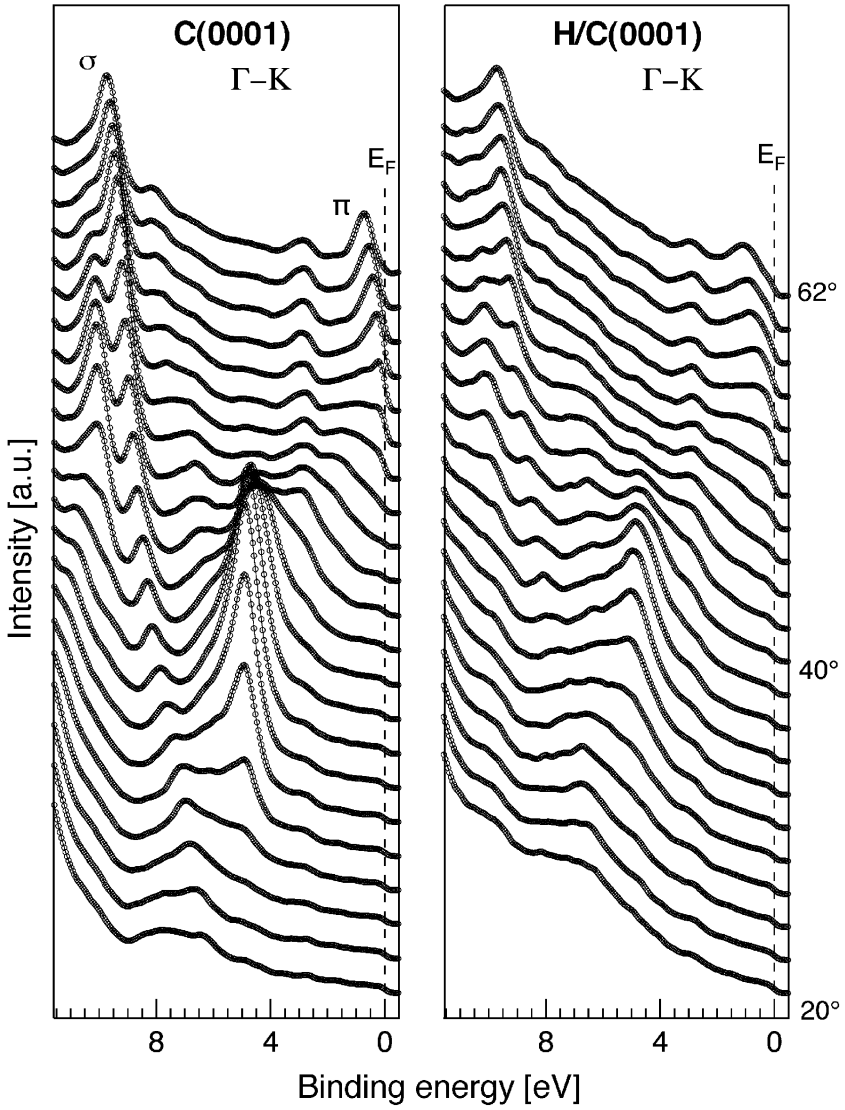

Figure 3.6: Angle-resoved spectra in the $\Gamma - K$ direction for the untreated C(0001) surface and after 180 s H_2 plasma treatment using He I (21.2 eV) radiation and an energy resolution of 60 meV. Spectra are taken for polar angles in the range between 62° and 20° with increments of 2°.

features, which are due to emission from a σ-band at high binding energies and emission from the π-band dispersing from the Fermi level ($\vartheta = 54°$) to 5 eV binding energy ($\vartheta = 34°$), respectively. The low-energy cutoff of the valence band spectrum reveals a work function of 4.5 eV for the untreated sample.

In a first attempt to adsorb hydrogen on the graphite surface we exposed the sample to atomic hydrogen. Comparison of the electronic structure and the work function with the values before the treatment showed no change induced by the atomic hydrogen. That is even the case for doses, where hydrogen chemisorption has saturated on C_{60} and SWNT.

The situation is different when the C(0001) surface is treated in the H_2 plasma. Doses of about 10^{14} ions/cm^2 cause modifications in the electronic structure of the surface. The intensity on the π-band decreases as a function of the plasma treatment time. The ratio between the intensity on the π-state and the intensity on the σ-state drops by a factor of about 1.7 for the longest treatment time (320 s). This indicates that the hydrogen ions are sufficiently energetic to chemically bond to the basal plane of graphite. Hydrogen adsorption leads to a broadening of the features, which affects especially the π-band. The σ-derived state shows an increase of the FWHM from 0.79 to 0.84 eV, whereas the FWHM of the π-derived state increases from 0.63 to 0.86 eV (Fig. 3.6). At 9.9 eV binding energy, a localised state appears upon hydrogen uptake at the surface. The dispersing graphitic features remain unchanged in their energy position.

Spectra taken in the $\Gamma - \mathrm{M}$ direction are dominated by a single dispersing feature at 8 - 3 eV binding energy, which is due to emission from a π-band. The changes due to hydrogen uptake are similar to the ones observed on the π-band in the $\Gamma - \mathrm{K}$ direction, i.e. a lowering of the intensity and a small broadening. Again, a hydrogen-related state appears at 9.9 eV binding energy with increasing coverage of chemisorbed hydrogen.

Chemisorption of hydrogen leads to an increased emission of secondary electrons over the hole range of the valence band and the lowering of the work function by 0.4 eV to a value of 4.1 eV for a treatment time of 320 s. The non-dispersing feature at 9.9 eV binding energy is consistent with the position of the hydrogen-related feature of density-of-states calculations for this C-H

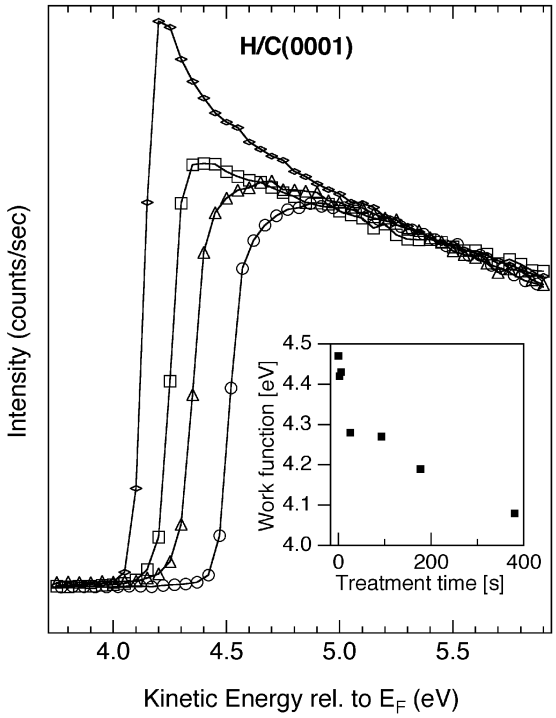

Figure 3.7: Low energy cut off of the valence band spectra of graphite after different H_2 plasma treatment times. The spectra have been measured using He I (21.2 eV) radiation and an energy resolution of 60 meV. Spectra are given for the untreated surface (circles), 25 s (triangles), 180 s (squares) and 390 s (diamonds) treatment time and are normalised to the intensity at 5.5 eV. The inset shows the work function change as a function of the treatment time.

---

configuration. [16]

XPS analysis at grazing emission (enhanced surface sensitiviy) of the C1s core level after different treatment times shows the growing of a hydrogen-related component at higher binding energies leading to a broadening of the line by ~ 0.1 eV.

For the longest treatment times a loss of surface quality was observed in

the LEED pattern. This is due to the small fraction of hydrogen ions having an energy that is high enough to create atomic vacancies in the top layer, as observed with atomic force microscopy [4]. This might also be responsible for part of the broadening observed on the spectral features.

The theoretical works of Jeloaica *et al.* [8] and Sha *et al.* [9] showed DFT calculations of the potential energy between atomic hydrogen and the graphite surface. They found adsorption energy barriers of ∼0.2 eV for an approaching hydrogen atom in the case where the carbon atom below the hydrogen atom is allowed to fully relax to its minimum energy position. However, a substantial displacement of ~ 0.4 Å is required to minimise the energy barrier. If the carbon atoms are not allowed to move, the adsorption energy barrier seen by the hydrogen atom increases to ~ 0.4 eV. The theoretical works thus yields an energy barrier for the chemisorption process that varies between ~ 0.2 eV and ~ 0.4 eV, depending on how fast the carbon atoms can relax. However, the experimental results show, that thermally dissociated hydrogen does not chemisorb on the graphite surface. This indicates, that the calculated adsorption energy barriers are probably underestimated.

3.1.3.4 Curvature dependence of H chemisorption

The results discussed above are summarised in Table 3.1. The local curvature is described by the height h, which is the distance between a carbon atom and the plane defined by its nearest neighbours. It is as well a measure of the local admixture of sp^3-character. The bond angle varies from 120° (pure sp^2-bonding) to 109.5° for pure sp^3-bonding, i.e. for diamond, which is given here for comparison [19].

The results obtained for different sp^2-bonded carbon samples reveal a strong dependence of the hydrogen-carbon interaction on the admixture of sp^3 bonding induced by the local curvature of the substrate. The fact that atomic hydrogen adsorbs on SWNT and C_{60}, but not on graphite, indicates a lowered adsorption energy barrier for strongly curved structures. The maximum hydrogen coverage achieved on C_{60} and SWNT upon exposure to atomic hydrogen treatment is limited by an increase of the adsorption energy barrier to a critical value, as further hydrogen adsorption can be observed by exposure to more

energetic hydrogen species of a H_2 plasma. From this consideration the saturation hydrogen coverage upon exposure to atomic hydrogen corresponds to the same critical value of the adsorption energy barrier for C_{60} and SWNT. That this critical value is obtained at higher hydrogen coverage for C_{60} as compared to the SWNT can have two possible reasons. Firstly, the coverage dependent energy barrier for the SWNT is offset to higher values as compared to the C_{60}, or secondly, the energy barrier increases more rapidly with increasing coverage for the SWNT. Considering the DFT results of Sha *et al.* and the fact, that no adsorption was observed on planar graphite using atomic hydrogen speaks in favour of a lowered adsorption energy barrier for all coverages when the local curvature in the sp^2-network is increased.

Comparison of the intensity reduction on the π-related features with the lowering of the work function shows a clear dependence between the work function change and the hydrogen coverage, as expected from the coverage dependent dipole density at the surface. However, the lowering of the work function is not proportional to the coverage, but flattens with increasing coverage. This is mainly due to the fact, that dipoles depolarise each other with increasing coverage, a phenomena that is generally observed for adsorbates [30].

	h [Å]	$(I_\pi/I_{\pi_0})_H$	$(I_\pi/I_{\pi_0})_{H^+}$	$\Delta\phi_H$ [eV]	$\Delta\phi_{H^+}$ [eV]
C(0001) (sp^2)	0	1	0.60	0.0	0.4
SWNT	0.11	0.78	0.50	0.3	0.6
C_{60}	0.29	0.53	0.27	0.8	1.3
C(111) (sp^3)	0.52	-	-	-	1.4

Table 3.1: Summarised results on the interaction of atomic hydrogen and hydrogen ions with the investigated samples. The height h indicates the distance of a carbon atom to the plane defined by its nearest neighbours and gives a measure for the local curvature of the sp^2-network. $\Delta\phi$ is the maximum reduction of the work function for atomic hydrogen treatments (H) and H_2 plasma treatments (H^+). The ratio (I_π/I_{π_0}) gives the lowering of the intensity on the π-derived states with respect to the untreated sample. The values for the SWNT are for the sample with an average diameter of $d_T = 1.2$ nm. The work function change between the hydrogen-passivated and the hydrogen-free diamond (111) surface is given for comparison [19].

It is interesting to compare the work function changes observed on the sp^2-bonded carbon with experiments done on hydrogen-covered diamond (sp^3). The maximum work function change of 1.3 eV observed on the C_{60} film approaches the values for the diamond C(111) and C(100) surfaces, where the hydrogen-covered surface has a work function which is lowered by 1.4 eV compared to the hydrogen-free surface [19, 29]. This gives a further indication of the large dipole created on the the C_{60} film.

3.1.4 Summary and conclusion

We have studied the interaction of atomic hydrogen and low energy hydrogen ions with sp^2-bonded carbon surfaces of different local curvatures. Hydrogen chemisorption is evidenced by a reduced intensity on the π-derived states induced by the transformation to more tightly bound σ-derived C-H bond states. The chemisorption of hydrogen generally leads to a lowering of the work function of up to 1.3 eV (C_{60} mulitlayer). This reduced work function is mainly attributed to a modified surface dipole and, by electronegativity arguments, indicates that hydrogen is adsorbed above the carbon layers.

Experiments with atomic hydrogen show that the adsorption energy barrier for bond formation decreases with the local curvature of the sp^2-network since atomic hydrogen was partially adsorbed on C_{60} and SWNT but not on graphite. This behaviour is attributed to the higher sp^3-character of convex sp^2-structures, which is in agreement with DFT calculations [8, 9] showing a lowering of the energy barrier for a carbon atom that is raised above the plane defined by its nearest neighbours. Our results show that the adsorption energy barrier increases with increasing coverage, leading to saturation coverages which depend on the form of hydrogen (i.e. atomic or ionic) used for the treatment. Accordingly, we found the highest hydrogen coverage ($\theta \simeq 0.7$) on the C_{60} multilayer using low energy hydrogen ions.

The experiments indicate a lower estimation of the critical radius of curvature of $r_{cr} \approx 6$ Å for the chemisorption of hydrogen on sp^2-bonded carbon structures. For a more restrictive determination of the critical curvature, SWNT samples with narrow diameter distributions would be required for tube diameters of $d_T > 1.2$nm.

This work was supported by the Swiss National Science Foundation (MaNEP) and the European Network FUNCARS.

References for Chapter 3

[1] H.W.Ch. Postma, T. Teepen, Z. Yao, M. Grifoni, and C. Dekker, Science **293**, 76 (2001).

[2] H.J. Choi and J. Ihm, Phys. Rev. Lett. **84**, 2917 (2000).

[3] M. Bockrath, W. Liang, D. Bozovic, J.H. Hafner, C.M. Lieber, M. Tinkham, and H. Park, Science **291**, 283 (2001).

[4] P. Ruffieux, O. Gröning, P. Schwaller. L. Schlapbach, and P. Gröning, Phys. Rev. Lett. **84**, 4910 (2000).

[5] W. Clauss, D.J. Bergeron, M. Freitag, C.L. Kane, E.J. Mele, and A.T. Johnson, Europhys. Lett. **47**, 601 (1999).

[6] Z. Klusek, Appl. Surf. Sci. **125**, 339 (1997).

[7] H.A. Mizes and J.S. Foster, Science **244**, 559 (1989).

[8] L. Jeloica and V. Sidis, Chem. Phys. Lett. **300**, 157 (1999).

[9] X. Sha and B. Jackson, Surf. Sci. **496**, 318 (2002).

[10] S. Nowak, P. Gröning, O.M. Küttel, M. Collaud, and G. Dietler, J. Vac. Sci. Technol. A **10**, 3419 (1992).

[11] O.M. Küttel, J.E. Klemberg-Sapieha, L. Marinu, and M.R. Wertheimer, Thin Solid Films **193/194**, 155 (1990).

[12] U. Bischler and E. Bertel, J. Vac. Sci. Technol. A **11**, 458 (1993).

[13] R.E. Haufler, J.J. Conceicao, L.P.F. Chibante, Y. Chai, N.E. Byrne, S. Flanagan, M.M. Haley, S.C. O'Brien, C. Pan, Z. Xiao, W.E. Billups, M.A. Ciufolini, R.H. Hauge, J.L. Margrave, L.J. Wilson, R.F. Curl, and R.E. Smalley, J. Phys. Chem. **94**, 8634 (1990).

[14] D. Koruga, S. Hameroff, J. Withers, R. Loutfy, and M. Sundareshan, *Fullerene C_{60}: History, Physics, Nanobiology, Nanotechnology*, North-Holland, Amsterdam (1993).

[15] J.L. Martins, N. Troullier, and J.H. Weaver, Chem. Phys. Lett. **180**, 457 (1991).

[16] J. Schäfer, J. Ristein, R. Graupner, and L. Ley, Phys. Rev. B **53**, 7762 (1996).

[17] J. Robertson and E.P. O'Reilly, Phys. Rev. B, **35**, 2946 (1987).

[18] T. Guo and G.E. Scuseria, Chem. Phys. Lett. **191**, 527 (1992).

[19] L. Diederich, O.M. Küttel, P. Aebi, and L. Schlapbach, Surf. Sci. **418**, 219 (1998).

[20] G. Beamson and D. Briggs, High Resolution XPS of Organic Polymers (John Wiley and Sons, Chichester, 1992).

[21] J.J. Pireaux, S. Svensson, E. Basilier, P.-A. Malmqvist, U. Gelius, R. Caudano, and K. Siegmann, Phys. Rev. A **14**, 2133 (1976).

[22] R. Graupner, Ph.D. thesis, University of Erlangen-Nürnberg, 1997.

[23] T.R. Ohno, C. Gu, J.J. Weaver, L.P.F. Chibante, and R.E. Smalley, Phys. Rev. B **47**, 13848 (1993).

[24] L.C. Qin, X. Zhao, K. Hirahara, Y. Miyamoto, Y. Ando, and S. Iijima, Nature **408**, 50 (2000).

[25] H. Kuzmany, W. Planck, M. Hulman, Ch. Kramberger, A. Grüneis, Th. Pichler, H. Peterlik, H. Kataura, and Y. Achiba, Eur. Phys. J. B **22**, 307 (2001).

[26] K. Kobayashi, Phys. Rev. B **48**, 1757 (1993).

[27] S.M. Lee and Y.H. Lee, Appl. Phys. Lett. **76**, 2877 (2000).

[28] S.M. Lee, K.H. An, W.S. Kim, Y.H. Lee, Y.S. Park, G. Seifert, and T. Frauenheim, Synth. Met. **121**, 1189 (2001).

[29] J.B. Cui, J. Ristein, and L. Ley, Phys. Rev. Lett. **81**, 429 (1998).

[30] Gabor A. Somorjai, *Chemistry in two dimensions: surfaces*, Cornell University Press, London (1981).

Chapter 4

Point Defect Induced Charge Redistribution at the Graphite Surface

This chapter consists of two sections dealing with the local modifications of the electronic structure of graphite in the presence of point defects consisting of hydrogen adsorption sites and atomic vacancies. Due to its largely defect-free surface, graphite represents the ideal system for the study of the long-ranged electronic effects of point defects that were artificially introduced into a sp^2-bonded carbon network.

The first section focusses on the characterisation of isolated defects in view of the range and kind of electronic modifications induced in by point defects. Thereby, the combined mode of AFM/STM permits the simultaneous imaging of the local topography and the LDOS near the defects sites. Furthermore, this mode with the normal force as feedback signal has proven to yield stable scanning conditions for the mapping of the tunneling current at low sample bias ($\leq$ 100 mV), a requirement for imaging the LDOS near the Fermi level.

In the second section, we discuss the origin of the standing wave patterns detected in the vicinity of defects and point out the direct relation between the contour of the Fermi surface of graphite and the observed patterns. The second

article is not yet submitted for publication because of an ongoing collaboration with a theoretical group, where we work on the simulation of the experimentally observed standing wave patterns in the LDOS. The aim of this simulation is the assignment of the phase of the induced standing waves to the type of point defect.

4.1 Hydrogen Atoms Cause Long-range Electronic Effects on Graphite

P. Ruffieux, O. Gröning, P. Schwaller, L. Schlapbach, and P. Gröning

Physics Department, University of Fribourg, Pérolles, CH-1700 Fribourg, Switzerland

published in Phys. Rev. Lett. **84**, 4910 (2000)

We report on long-range electronic effects caused by hydrogen-carbon interaction at the graphite surface. Two types of defects could be distinguished with a combined mode of scanning tunneling microscopy and atomic force microscopy: chemisorption of hydrogen on the basal plane of graphite and atomic vacancy formation. Both types show a $(\sqrt{3} \times \sqrt{3})R30^\circ$ superlattice in the local density of states but have a different topographic structure. The range of modifications in the electronic structure, of fundamental importance for electronic devices based on carbon nanostructures, has been found to be of the order of 20 - 25 lattice constants.

Defects control many physical properties of solids and dominate the electronic behaviour of nanoscale metallic and semiconducting systems, particularly at low dimensions. The study of changes in the electronic structure of graphite due to adsorbates is relevant for other carbon materials (such as nanotubes, fullerenes, etc.) having the six membered ring as structural unit [1]. Scanning tunneling microscopy (STM) makes it possible to directly investigate the electronic features induced by defects with atomic resolution [2, 3]. Graphite was one of the first materials for which long-range order electronic effects caused by surface defects have been predicted and experimentally observed using STM [4,5]. Graphite is a semimetal composed of stacked hexagonal planes of sp^2 hybrid bonded carbon atoms. The ABAB stacking of these planes in a three-dimensional crystal creates two inequivalent sites with different properties with regard to the electronic structure: α site atoms are exactly located above atoms of the underlying plane, whereas β site atoms are located above the center of the hexagonal rings of the underlying plane. The weak Van der Waals interaction between adjacent planes leads to a suppression of the charge density at the Fermi level at α sites [6]. These two inequivalent sites explain the fact that with STM, which probes only electronic tates near the Fermi level, a trigonal symmetry on the graphite surface is imaged.

In this letter we report on new electronic effects caused by adsorption of atomic hydrogen on graphitic surfaces. A combined mode of STM and atomic force microscopy (AFM) was used to study both, topographic and electronic changes in the vicinity of defects. The interaction of an individual H atom with a graphite surface modifies the electronic structure over 20 - 25 lattice constants leading to a $(\sqrt{3} \times \sqrt{3})R30^\circ$ superstructure in the local density of states (LDOS). A detailed understanding of such defect induced electronic modifications is indispensable for the development of electronic devices based on carbon nanostructures [1, 7, 8].

Samples of highly oriented pyrolithic graphite (HOPG) were cleaved in air with adhesive tape right before loading into the hydrogen electron cyclotron resonance (ECR) plasma chamber which served as a hydrogen ion source [9]. Typically a gas pressure of 10^{-3} mbar hydrogen was used for the plasma treatment, the base pressure of the chamber beeing in the low 10^{-8} mbar range.

The average ion energy at this pressure is ∼10 eV. The sample is set to ground potential. The ion flux at the sample position is typically 10^{12} $cm^{-2}s^{-1}$. Sample heating can be neglected under these conditions. After plasma treatment the samples were either vacuum transferred to a connected photoelectron spectrometer (VG ESCALAB 5) equipped with a Mg $K\alpha$ ($h\nu$ = 1253.6 eV) anode for X-ray photoelectron spectroscopy (XPS) and a helium discharge lamp ($h\nu$ = 21.2 eV) for ultraviolet photoelectron spectroscopy (UPS) or transferred in air to an AFM/STM (OMICRON) working in ultrahigh vacuum at room temperature. In order to observe isolated defects with SPM short plasma treatment times, typically a few seconds, were used resulting in a defect density of $\sim 10^{-2}$ nm^{-2}. To overcome the detection limit for the hydrogen induced features in XPS and UPS, however, the sample was treated for 300s. To obtain the topographic structure around one single defect the surface was scanned using a conductive cantilever in the AFM contact mode. This has the advantage of simultaneous imaging of the rearrangement of atom positions (AFM signals) and of the affected LDOS (current signal) in the vicinity of a defect. Atomically resolved current and topography images could be obtained using silicon nitride AFM tips coated with highly conductive boron doped diamond. Scan rates and applied forces in the contact mode were typically 10 Hz and 1nN, respectively. For the simultaneous measurement of the current image a gap voltage of 30 - 100 mV was applied to the AFM tip.

Simultaneous measurements of the current and AFM signals, like normal force, lateral force, and the piezo z-position do not only yield the topographic and electronic structure of defects, but additionally give information about changes of the tip condition: Sudden changes to higher tunneling currents for a given force setpoint indicate the sticking of a graphitic flake at the AFM tip.

Scanning the plasma treated surface with a conventional STM tip (W) revealed the wellknown protrusions around the adsorption sites [4]. However, imaging the same surface in AFM mode did not show any elevated structures at the adsorption site. To understand these at first sight contradictory results it should be kept in mind that STM probes the occupied or unoccupied (depending on the sign of the sample bias) LDOS near the Fermi energy whereas AFM probes the total charge density. In the following we describe the two types of

defects we observed, namely chemisorbed hydrogen and atomic vacancies.

Chemisorbed hydrogen: Scanning the plasma treated surface in the AFM contact mode with simultaneous acquisition of the current signal yield clear superlattice type modifications of the electronic properties over a distance of 25 lattice constants (Fig. 1). However, no modifications were detected in the topography image. In the inset of Fig. 1(a) the center of the Fourier transform of the current image is displayed. The six inner spots correspond to the $(\sqrt{3} \times \sqrt{3})R30°$ superstructure. The six outer spots with the same orientation are due to the second harmonic of the superlattice, whereas the six outer spots rotated by 30° originate from the regular graphite lattice, i.e. the imaging of the β site atoms. The scattering pattern is independent of the applied sample bias (30 - 100 mV) for both, tunneling from occupied states and tunneling into unoccupied states of the sample. The threefold symmetry of the scattering pattern is clearly seen in Fig. 1(b), which shows the same data as (a) but after applying a two dimensional band pass filter to isolate the superlattice contribution. The scattering pattern has the same orientation as

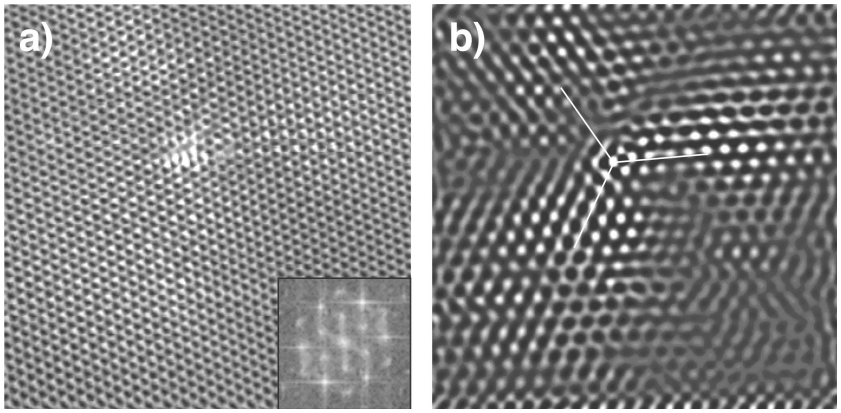

Figure 4.1: (a) Current image of a hydrogen plasma treated graphite surface recorded in AFM contact mode (94Å × 94Å). Measurement parameters are: force setpoint: 2 nN, sample bias: 30 mV. Current range: 1 nA (black) - 9 nA (white). The inset shows the center of the Fast Fourier Transform (FFT) of (a). (b) The same data as (a) after applying a two dimensional band pass filter to isolate the superlattice component.

the superstructure, which is indicated by the lines in Fig. 1(b). Applying the band pass filter to the six spots originating from the regular graphite lattice does not reveal any threefold scattering pattern.

Kelly *et al.* [10] discussed in a recent work the dependence of the orientation of the threefold scattering pattern on the type of atom, which is affected by an atomic vacancy. Scattering patterns originating from α site defects are rotated

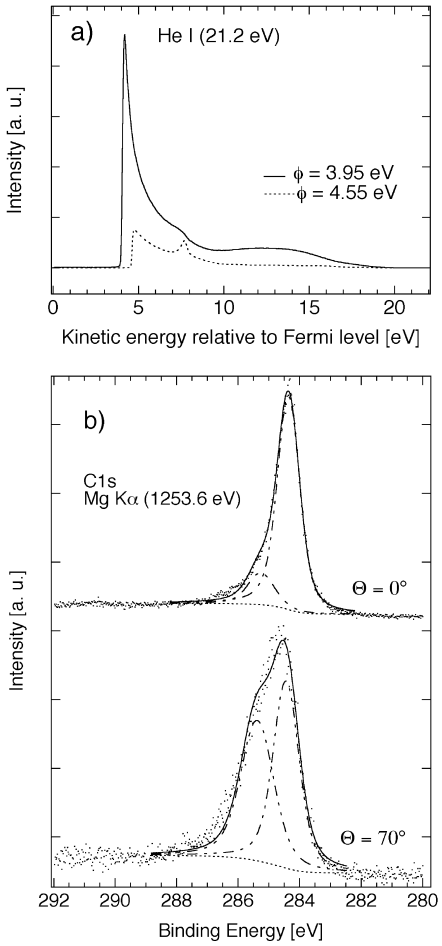

Figure 4.2: (a) Normal emission He I spectra before and after hydrogen plasma treatment. Sample bias: -10 V. (b) C 1s core level spectra of the hydrogen plasma treated graphite for normal (top) and grazing emission (bottom).

by 60° relative to the ones from β site atoms refelecting the symmetry of the dangling bonds of the nearest neighbours. These bonds are also affected if the hybridization of a carbon atom is changed by forming an additional bond to an adsorbed hydrogen atom. The lack of topographic modifications and the results of photoelectron spectroscopy (see below) suggest that this type of defect is caused by chemisorbed hydrogen atoms. Only one type of carbon atoms seems to be affected. If α and β sites were involved, one would expect a sixfold symmetric scattering pattern.

A more detailed analysis of the bandpass filtered current image shows that the measured scattering pattern results from two interfering scattering patterns with the same orientation, but with an origin shift of 2.46 Å, i. e. the distance between two carbon atoms of the same type.

The range of the superlattice in the electronic structure is found to be of the order of 25 lattice distances.

J.P. Chen *et al.* [11] found the chemisorption of hydrogen on the basal plane of graphite to be endothermic. A metastable state exists in all examined configurations, the most stable one being the on-top site. The on-top configuration also shows the lowest activation barrier ($\sim$1.8 eV). In an (ECR) plasma the ion energy (typically 10 eV) is large enough to populate this state, in contrast to treatments with an atomic hydrogen source [12], where we could not detect any adsorption of hydrogen on the basal plane of graphite.

Figure 2(a) shows normal emission photoelectron spectra recorded from the graphite surface before and after the hydrogen plasma treatment. In order to be able to determine the work function ϕ of the surface we applied a sample bias of -10 V. The cutoff at low kinetic energies reveals that the work function of the treated surface is lowered by 0.6 eV relative to that of the untreated surface. The lower work function indicates a change in the surface dipole moment originating from the polarized C-H bond. Since carbon is the more electronegative element, hydrogen atoms have to be positioned above the carbon atoms of the first monolayer. A lowering of the work function has also been observed for diamond where the hydrogen saturated surface has negative electron affinity [13, 15, 16]. The origin of this new dipole moment can be detected with XPS. Figure 2(b) shows C 1s core level photoelectron spectra of the treated

graphite surface for normal (top) and grazing emission (enhanced surface sensitivity). Analysis of relative intensities for different emission angles show that the hydrogen plasma induced feature at higher binding energy (285.4 eV) originates from the surface. A shift of 1.0 eV relative to the bulk contribution has also been observed on the hydrogen terminated diamond surface [13, 14]. It has been shown for different carbon systems that although carbon being the more electronegative element, the C-H contribution appears at higher binding energies. This has to be explained rather by a different relaxation energy (final state) for the differently hybridized carbon atoms of the first monolayer than

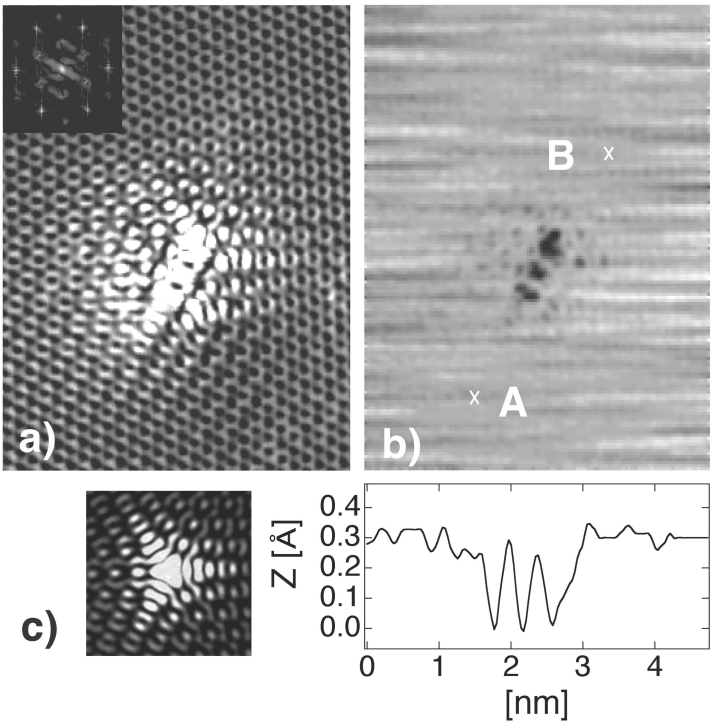

Figure 4.3: Simultaneously recorded current and topography image of a hydrogen plasma treated graphite surface in AFM contact mode (58Å × 78Å). Measurement parameters: force setpoint: 2 nN, sample bias: 30 mV. (a) Current image with FFT (inset). Current range: 2 nA (black) - 40 nA (white). (b) Topography image with line profile from A to B. (c) Calculated LDOS in the vicinity of a single atomic vacancy using a tight binding model (reprinted with permission from [4]).

simply with a Koopman's shift (initial state) [14, 17, 18].

Atomic vacancies: Typical images of the simultaneously recorded current and topography images of a local defect are shown in Fig. 3. The topographic structure of this defect consists of three local depressions with a corrugation of 0.3 Å. This strong enhancement of the corrugation, as compared to the ten times weaker corrugation of defect free zones, is interpreted as atomic vacancies in the first carbon monolayer, which were formed upon the hydrogen plasma treatment. The vacancy formation probability is found to be five times smaller than hydrogen adsorption. The depressions in Fig. 3(b) are separated by 4.1 Å. The direction and the distance between the topographic minima show that carbon atoms of the same type are affected (distance between second nearest neighbours of the same type is $\sqrt{3} \cdot 2.46$ Å $= 4.26$ Å). The current image shows the enhanced LDOS in the vicinity of the defect and again the $(\sqrt{3} \times \sqrt{3})R30°$ superlattice, which is visible over 25 lattice constants. The calculated LDOS for a single atomic vacancy [4] (Fig. 3(c)) shows the same features as we find for defects showing depressions in the topography image.

The threshold energies for sputtering off carbon atoms has been calculated by J. Bohdansky and J. Roth [19]. For a target-to-projectile ratio of $M_2/M_1 \leq 0.3$ the threshold energy is given by the empirical relation $E_{th} = \frac{U_0}{\gamma(1-\gamma)}$ where U_0 is the binding energy of surface atoms and $\gamma = 4\frac{M_1 M_2}{(M_1+M_2)^2}$ the energy transfer coefficient. For the interaction of hydrogen ions with graphite an energy threshold of $E_{th} \simeq 36\ eV$ (where U_0 can be approximated by the heat of sublimation [19] : $U_0 \simeq\ 7.4\ eV$ [20]) results from these considerations. The maximum ion energy in ECR plasma treatments is given by the plasma potential which originates from the different mobilities of electrons and ions. The potential depends on the chamber geometry and the gas pressure. The maximum ion energies in the plasma chamber used for this experiment range from ∼22 eV (10^{-4} mbar) to about 9 eV (10^{-1} mbar) [9] which is well below the estimated energy threshold for vacancy formation by sputtering. A possible channel for vacancy formation is the neutralization process of the ions. The charge transfer from the surface to the approaching ion leads to a weakening and a finite destruction cross section of the sp^2 bonds [21].

In summary, our studies of the interaction of hydrogen ions with the

graphite surface by means of a combined mode of AFM/STM and photoelectron spectroscopy reveal chemisorption of hydrogen and atomic vacancy formation on the basal plane of graphite. Chemisorbed hydrogen does not show any structure in the topography signal but consists of a local charge enhancement and a long-range perturbation of the electronic structure consisting of a $(\sqrt{3} \times \sqrt{3})R30°$ superstructure in the LDOS. The range of the modified electronic structure is of the order of 6 nm. Atomic vacancies consist of local depressions in the topography image. The current image of this defect type shows a local charge enhancement, which is in good agreement with the previously calculated LDOS near an atomic vacancy and again a $(\sqrt{3} \times \sqrt{3})R30°$ superlattice in the vicinity of the defect. Simultaneous recording of topography and current signal in the AFM contact mode has been found to be a powerful tool for imaging both, the topographic structure and the long-range changes in the LDOS of defects.

Skillful technical assistance was provided by R. Schmid, E. Mooser, O. Raetzo, Ch. Neururer, and F. Bourqui. This work was supported by the Swiss National Science Foundation.

References for Section 4.1

[1] M.S. Dresselhaus, G. Dresselhaus, and P.C. Eklund, *Science of Fullerenes and Carbon Nanotubes* (Academic Press, San Diego, 1996).

[2] M.F. Crommie, C.P. Lutz, and D.M. Eigler, Nature **363**, 524 (1993).

[3] Y. Hasegawa and Ph. Avouris, Phys. Rev. Lett. **71**, 1071 (1993).

[4] H.A. Mizes and J.S. Foster, Science **244**, 559 (1989).

[5] J. Xhie, K. Sattler, U. Muller, N. Venkateswaran, and G. Raina, Phys. Rev. B **43**, 8917 (1991).

[6] D. Tomanek, S.G. Louie, H.J. Mamin, D.W. Abraham, R.E. Thomson, E. Ganz, and J. Clarke, Phys. Rev. B **35**, 7790 (1987).

[7] L.C. Venema, J.W.G. Wildóer, J. W. Janssen, S.J. Tans, H.L.J. Temminck Tuinstra, L.P. Kouwenhoven, and C. Dekker, Science **283**, 52 (1999).

[8] F. Léonard and J. Tersoff, Phys. Rev. Lett. **83**, 5174 (1999).

[9] S. Nowak, P. Gröning, O.M. Küttel, M. Collaud, and G. Dietler, J. Vac. Sci. Technol. A **10**, 3419 (1992).

[10] K.F. Kelly and N.J. Halas, Surf. Sci. **416**, L1085 (1998).

[11] J.P. Chen and R.T. Yang, Surf. Sci. **216**, 481 (1989).

[12] U. Bischler and E. Bertel, J. Vac. Sci. Technol. A **11**, 458 (1993).

[13] L. Diederich, O.M. Küttel, P. Aebi, and L. Schlapbach, Surf. Sci. **418**, 219 (1998).

[14] R. Graupner, Ph.D. thesis, University of Erlangen-Nürnberg, 1997

[15] F.J. Himpsel, J.A. Knapp, J.A. VanVechten, and D.E. Eastman, Phys. Rev. B **20**, 624 (1979).

[16] J.B. Cui, J. Ristein, and L. Ley, Phys. Rev. Lett. **81**, 429 (1998).

[17] J.J. Pireaux, S. Svensson, E. Basilier, P.-A. Malmqvist, U. Gelius, R. Caudano, and K. Siegmann, Phys. Rev. A **14**, 2133 (1976).

[18] G. Beamson and D. Briggs, High Resolution XPS of Organic Polymers (John Wiley and Sons, Chichester, 1992).

[19] J. Bohdansky and J. Roth, J. Appl. Phys. **51**, 2861 (1980).

[20] B.T. Kelly, Physics of Graphite (Applied Science Publishers, New Jersey, 1981).

[21] V.V. Khvostov, M.B. Guseva, V.G. Babaev, E.A. Osherovich, Surf. Sci. **320**, L123 (1994).

4.2 Charge-density oscillation on graphite induced by the interference of electron waves

P. Ruffieux, M. Bielmann, and P. Gröning

Physics Department, University of Fribourg, Pérolles, CH-1700 Fribourg, Switzerland

O. Gröning and L. Schlapbach

Swiss Federal Laboratories for Materials Testing and Research, Überlandstrasse 129, 8600 Dübendorf, Switzerland

to be submitted

We report on a pronounced redistribution of the local electronic density of states at the graphite surface, which is induced by the presence of point defects. Room temperature scanning tunneling microscopy reveals standing waves in the LDOS which form within a range of ∼6 nm from a single point defect a superstructure that is commensurate with the graphite lattice. The origin of the superstructure is the scattering of the electron waves at point defects which induces the formation of standing waves in the local density of states. These standing waves can be directly related to the quasi point like Fermi surface of graphite. A high defect density leads to interference of standing waves originating form different defects and shows a variety of patterns in the charge distribution. The observed LDOS could be reproduced by a sum of plane waves with wavevectors that correspond to the Fermi wavevectors of graphite and adjusted amplitudes and relative phases.

Defects are known to play an important role in the local modification of electronic properties of solids. Their role as electron scatterers and creators of tunnel junctions has recently been evidenced on carbon nanostructures and has even allowed the realisation of single molecular electronic devices [1–3]. The long-range character of the electronic modifications due to defects has been shown for metals where they are known as Friedel oscillations [4–6]. These oscillations mediate an indirect interaction between adsorbates which exhibits the same oscillatory behaviour [5]. Similar oscillations in the charge density have been observed on the graphite surface with a typical range of the charge redistribution of ~ 6 nm [7–9]. On sp^2-bonded carbon, the strong redistribution of the delocalised π-electronsystem due to point defects can be expected to cause large local variations in the chemisorption behaviour, for instance for hydrogen.

In this work we report on the point defect induced charge redistribution at the graphite surface, which is manifested as standing waves with a wavelength that corresponds to the Fermi wavelength λ_F. These standing waves are due to the scattering of the delocalised electrons at the point defects and can be directly related to the point like character of the Fermi surface of graphite. For high defect densitites, the interference of standing waves originating from different defects leads to a variety of patterns in the local density of states (LDOS).

Samples of highly oriented pyrolithic graphite (HOPG) were cleaved in situ under ultrahigh vacuum conditions. Point defects on the clean graphite surface were created by exposure to a H_2 electron cyclotron resonance (ECR) plasma. A typical ion dose used for the treatment was of the order of 10^{13} ions/cm^{-2}. The average ion energy of ~ 2 eV, has been determined with an electrostatical analyser. The hydrogen plasma treatment leads to atomic defects consisting of hydrogen chemisorption on the basal plane of graphite and the formation of atomic vacancies. After plasma treatment, the sample was transferred to the vacuum-connected atomic force/scanning tunneling microscope (AFM/STM, Omicron) working under ultrahigh vacuum conditions at room temperature. Measurements were performed in the combined mode of AFM/STM using the normal force as feedback signal and applying a fixed bias voltage between the

sample and the tip. The recording of the piezo z-position and the tunneling current allows the simultaneous determination of the topography and the LDOS. For this measurement mode we used AFM tips coated with highly conductive boron doped CVD-diamond. In the absence of defects the usual trigonal structure with maxima in the LDOS observed on every second atom of the top layer [10].

Figure 4.4 shows an overview current image ($U = 70$ mV) of a sample that has been exposed to H_2-plasma for 3 s. As reported earlier, exposure to hydrogen ions mainly results in two types of defects [8]. Firstly, chemisorption of hydrogen on the basal plane of graphite and secondly, atomic vacancy formation. The formation of atomic vacancies is observed with about four times lower frequency compared to the formation of adsorption defects. Both types of defects lead to a strong modification of the local electronic structure near the Fermi level, as observed in the current image. The symmetry of the short-ranged (~ 1 nm) modifications has been used to determine the geometric structure of the defect [7]. In particular, atom vacancies have been shown to give rise to a local charge enhancement having a threefold symmetry. The orientation is related to the nearest-neighbour directions of the defect site and thus allows the separation between α- and β-atom vacancies. Beside these very local modifications, defects mediate a redistribution of the charge density on a large scale. For adsorbate and vacancy type defects on graphite we found a characteristic length of about 6 nm of the modified electronic structure. This perturbed structure is due to the scattering of electronic states at the impurity which gives rise to the formation of standing waves in the vicinity of a defect. The standing waves have a periodicity larger than, but commensurate with the underlying graphite lattice. From the Fast Fourier Transform (FFT) of current images in the vicinity of defects, the charge density redistribution expresses itself as a $(\sqrt{3} \times \sqrt{3})R30°$ superlattice.

The Fermi surface of graphite consists of small electron and hole pockets located at the corners of the Brillouin zone which enclose a very low volume. Figure 4.5 shows the bandstructure of graphite for the high-symmetry line Γ-K. [11] The weak interaction between the layers lifts the degeneracy of the bands. The resulting energy splitting of the π-bands is of 0.7 eV at the K

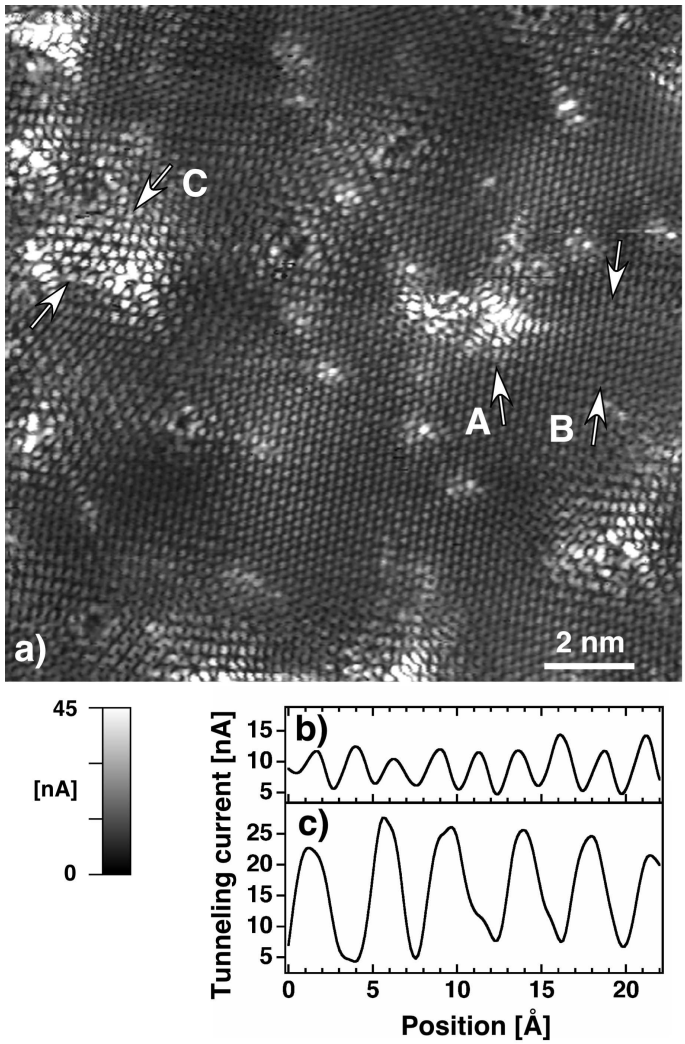

Figure 4.4: (a) Current image of sample treated with H_2 plasma. The observed defect density is of the order of 20 per 100 nm^2. The data is recorded in the AFM constant force mode with an gap voltage of 70 mV. The scan range is 16 x 16 nm^2. The data is displayed using a linear grey scale with the highest current (45 nA) in white. The arrow A markes the position of a vacancy type defect. (b) Line cut at position B showing the undisturbed lattice. (c) Line cut at position C where the LDOS is dominated by the $\sqrt{3}$-superstructure.

points. Accordingly, just one π-band contributes to the tunneling current if a small sample bias is applied in a tunneling experiment. As mentioned above, it contributes to the density of states (DOS) at the Fermi energy (E_F) with wave vectors corresponding to the K points. An electron at E_F thus has a wave vector of $k_F = 4\pi/3a$ directed towards a corner of the Brillouin zone (where a is the lattice constant of graphite ($a = 2.46$Å)).

In the case of graphite, backscattering of electrons at surface steps or point defects is possible via two scattering channels. Reflection via small momentum scattering is possible via coupling between bands at a **K** point since they describe a forward and a backward moving channel. The small momentum scattering conserves the lattice periodicity but can break the rotational symmetry of the LDOS [12]. The second possibility for reflection at defects is large mo-

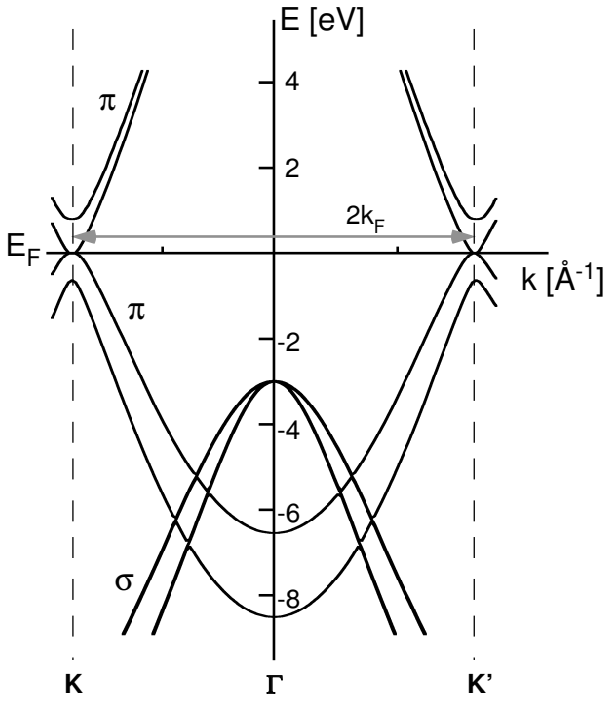

Figure 4.5: Bandstructure of graphite along the high-symmetry line Γ-K. The calculation has been performed using the WIEN code [11].

mentum scattering between two opposite **K** points. In this case, the required momentum change from **K** to **K'** equals $\mathbf{q} = 2\mathbf{k}_F$. This large momentum scattering has also been observed at metal surfaces leading to Friedel oscillations with a periodicity that is related to the Fermi wave vector of the surface states. Since in this case, the involved charges form a free electron gas, there is no firm relation between $\mathbf{k}_F$ and the lattice parameters and consequently, the ovserved superstructure in the LDOS is not commensurate with the underlying lattice.

On graphite, however, there is a relation between the lattice and the Fermi wave vectors, since they coincide with the corners of the first Brillouin zone. The relation between the momentum change for large momentum scattering and the lattice parameter is given by $q = 2k_F = 8\pi/3a$. The required momentum change is reduced to $\mathbf{q} = \mathbf{k}_F$ if an appropriate reciprocal lattice vector is taken into account: $\mathbf{q} = 2\mathbf{k}_F = \mathbf{k}_F + \mathbf{G}$ (Fig. 4.6). Therefore, a modulation of the LDOS with a wavelength that corresponds to the Fermi wavelength $\lambda_F = 3a/2$ is expected for large momentum scattering on graphite.

Figure 4.6 b) shows the Fast Fourier transform (FFT) of the large scale current image shown in Fig 4.4. Compared to a FFT of the unperturbed lattice, new peaks appear at smaller wave vectors which match the corners of the Brillouin zone, i.e. the Fermi wave vectors $\mathbf{k}_j$. In the real space image, this superstructure is observed as a $(\sqrt{3} \times \sqrt{3})R30°$ modulation of the LDOS in the vicinity of defects. This shows the direct relation existing between the Fermi surface contour and the observed pattern of the standing waves in the vicinity of scatterers. The observed $\sqrt{3}$-superstructure in the LDOS and the absence of rotational symmetry breaking, which would be characteristic for small momentum scattering, indicate that large momentum scattering is the dominant reflection mechanism in the presence of point defects on graphite.

On samples with a low defect density, a decay of the intensity on the superstructure spots in the FFT is observed, as the distance to the nearest point defect increases. For isolated defects, the superstructure is detected on a typical range of 20 - 25 lattice constants. The phase, amplitude, and decay of the standing wave reflect the structure and symmetry of the defect, which could, in principle, be used for the identification of defects. [6, 7]

For increased defect densities where the typical distance between neigh-

bouring defects is below the range of the electronic modifications induced by a single defect, new structures are expected to appear in the LDOS due to the interference of the standing waves originating from different defects. Such interference patterns can be observed on samples where the typical distance between defects is in the range of 20 Å.

Figure 4.7 shows small area current images of the same high defect density sample as shown in Fig. 4.4. The images displayed in (b) - (e) are recorded in-between defects separated by a few nm's. These areas are all dominated by the $\sqrt{3}$-superlattice contribution and show the variety of patterns in the LDOS originating from the interference of two or more standing waves. For comparison, the current image of a region with low defect density is given in (a). This region shows the usual graphite lattice periodicity described by the

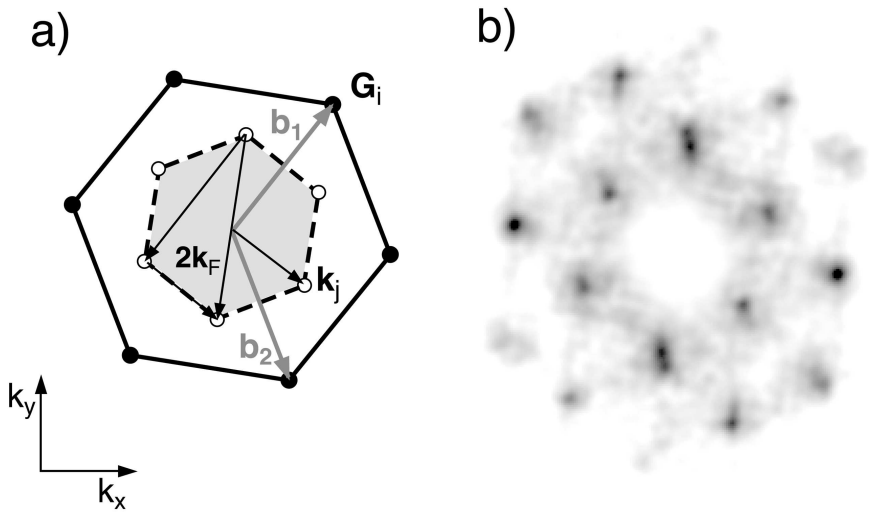

Figure 4.6: (a) Reciprocal lattice vectors and the 2D Brillouin zone (grey area) of graphite. The vectors $\mathbf{k}_j$ give the position of the K points. (b) Two-dimensional Fourier transform of the current image shown in Fig. 4.4. The spots forming the inner hexagon represent the $\sqrt{3}$-superstructure observed in the vicinity of defects. Spots forming the larger hexagon rotated by 30° appear at wave vectors that correspond to reciprocal lattice vectors $\mathbf{G}$. The outermost spots arise from the second harmonic of the inner hexagon. The spot at $\mathbf{k}$=0 has been removed for better visibility of the relevant features.

reciprocal lattice vectors $\mathbf{G}_i$.

Along the connecting line of the scatter centers of two interfering standing waves, the pattern remains unchanged, as the phase relation is conserved. However, due to the point-symmetry of the defects, the pattern changes along other directions. The characteristic range of a single phase is of the order of 20 Å.

The model of superposed scattered electron wavefunctions suggests a local description of the states near the Fermi level of the form of

$$\psi(\mathbf{r}) = \sum_{j=1}^{6} \phi_j e^{i\mathbf{k}_j \cdot \mathbf{r}} \tag{4.1}$$

where $\mathbf{k}_j$ denote the corners of the first Brillouin zone, since these are the only wave vectors allowed for states at the Fermi level. The coefficients ϕ_j are complex amplitudes describing the scattering phase shift and the reflection amplitudes. Images (f)-(i) show the calculated spatial distribution of $|\psi(\mathbf{r})|^2$ using Eq. (4.1). The complex numbers ϕ_j have been adjusted in order to reproduce the experimentally observed LDOS.

The good agreement between the calculated and the measured LDOS confirms the model of interfering standing waves originating from the scattering of electron wavefunctions at different defect sites. It shows in particular, that the local distribution of states near the Fermi level between defects is dominated by standing waves with wave vectors corresponding to the Fermi wave vectors $\mathbf{k}_j$ and that contributions having the lattice periodicity can be neglected. The variety of the spatial patterns originates from different phase shifts of the interfering standing waves that are due to the different relative positions of the defect sites and possible differences in the scattering potential, if different defects are present.

The extent of the charge redistribution near defects is further seen in the enhanced corrugation of the current signal. Compairing line cuts of the undisturbed lattice (Fig. 1a) with line cuts of a region where the $\sqrt{3}$-superstructure dominates (b), shows a corrugation of the tunneling current which is enhanced by a factor of about 3.

In conclusion, we have observed a marked redistribution of the LDOS in the vicinity of point defects on the graphite surface. The point defects, consisting

of hydrogen adsorption sites and atomic vacancies, break the lattice symmtery and act as scatterers for the delocalised electrons. The resulting standing waves are observed as a $\sqrt{3}$-superstructure in the tunneling current image which can be directly related to the point-like contour of the Fermi surface of graphite. For isolated defects, the typical range of the charge redistribution is of $\sim$6 nm. Our findings show that the origin of the superstructure in the LDOS is large momentum scattering of the π-electrons at the point defects. For samples with high defect densities, the interference of two or more standing waves results in a variety of patterns in the LDOS which depends on the relative phase between the individual standing waves. The experimentally observed patterns in the LDOS could be reproduced by a simulation where the electron wavefunctions are described as a superposition of plane waves having wave vectors that correspond to the corners of the first Brillouin zone which make up the Fermi surface.

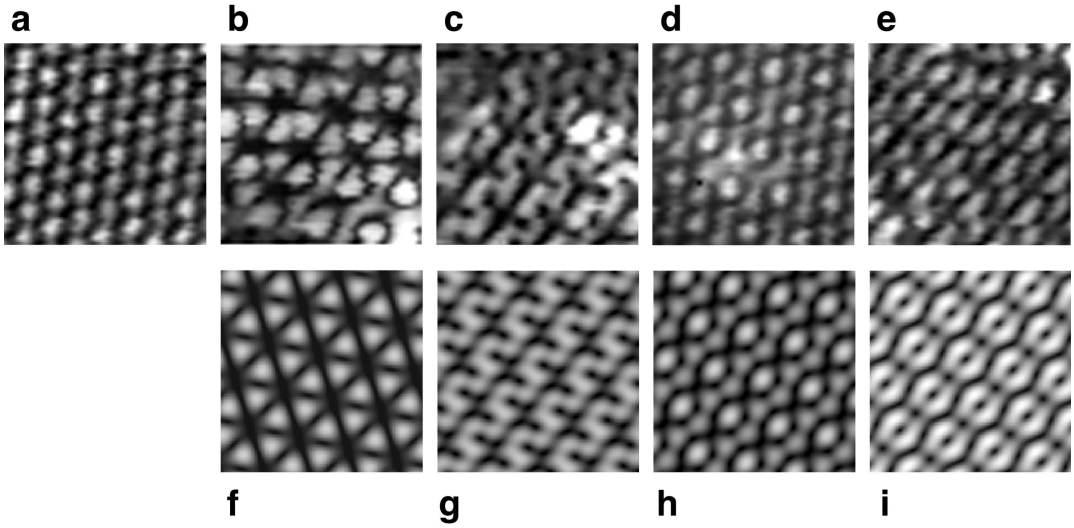

Figure 4.7: (a)-(e) Experimental current images recorded with a gap voltage of 70 meV. The individual images display regions that are present in the overview image (Fig. 4.4). The scan range for each image is 17.5×17.5 Å^2. (f)-(i) Calculated spatial maps of $|\psi(\mathbf{r})|^2$ according to Eq. (4.1). Appropriate values of the complex numbers ϕ_j have been selected to match the experimentally observed pattern.

Beside the influence on the transport properties due to scattering at the point defects, a modulation of the local reactivity for chemically adsorbing atoms has to be expected due to the marked redistribution of the LDOS in the vicinity of the defects.

References for Section 4.2

[1] M. Bockrath, W. Liang, D. Bozovic, J.H. Hafner, C.M. Lieber, M. Tinkham, and H. Park, Science **291**, 283 (2001).

[2] H.J. Choi and J. Ihm, Phys. Rev. Lett. **84**, 2917 (2000).

[3] H.W.Ch. Postma, T. Teepen, Z. Yao, M. Grifoni, and C. Dekker, Science **293**, 76 (2001).

[4] M.F. Crommie, C.P. Lutz, and D.M. Eigler, Nature **363**, 524 (1993).

[5] J. Repp, F. Moresco, G. Meyer, and K. Rieder, Phys. Rev. Lett. **85**, 2982 (2000).

[6] P.T. Sprunger, L. Petersen, E.W. Plummer, E. Lægsgaard, F. Besenbacher, Science **275**, 1764 (1997).

[7] H.A. Mizes and J.S. Foster, Science **244**, 559 (1989).

[8] P. Ruffieux, O. Gröning, P. Schwaller. L. Schlapbach, and P. Gröning, Phys. Rev. Lett. **84**, 4910 (2000).

[9] Z. Klusek, Appl. Surf. Sci. **125**, 339 (1997).

[10] D. Tománek, S.G. Louie, H.J. Mamin, D.W. Abraham, R.E. Thomson, E. Ganz, and J. Clarke, Phys. Rev. B **35**, 7790 (1983).

[11] P. Blaha, K. Schwarz, and J. Luitz, **WIEN97**, Vienna University of Technology 1997. (Improved and updated Unix version of the original copyrighted WIEN-code, which was published by P. Blaha, K. Schwarz, P. Sorantin, and S.B. Trickey, in Comput. Phys. Commun. **59**, 399 1990).

[12] C.L. Kane and E.J. Mele, Phys. Rev. B **59**, R12759 (1999).

Chapter 5

Supramolecular columns of hexabenzocoronenes on the copper and gold (111) surfaces

P. Ruffieux[1], O. Gröning[1,2], M. Bielmann[1], C. Simpson[3], K. Müllen[3], L. Schlapbach[1,2], and P. Gröning[1]

[1] *Physics Department, University of Fribourg, Pérolles, CH-1700 Fribourg, Switzerland*

[2] *Swiss Federal Laboratories for Materials Testing and Research, Überlandstrasse 129, 8600 Dübendorf, Switzerland*

[3] *Max-Planck-Institut für Polymerforschung, Ackermannweg 10, 55128 Mainz, Germany*

published in Phys. Rev. B **66**, 073409 (2002)

We report on the growth of supramolecular columns of polyaromatic hydrocarbons on Au(111) and Cu(111) single-crystal surfaces. The lateral separation of the columns was found to depend on the substrate and is determined by the commensurately formed superlattice of the first molecular monolayer. X-ray photoelectron diffraction in combination with low energy electron diffraction reveals stack growth with small lateral offsets from the column axis but with conservation of the molecular orientation. The mechanism of column growth is explained by simulation results of the intermolecular interaction assuming a Lennard-Jones potential. The size of hexabenzocoronene and its ability to condense into one - dimensional supramolecular structures make it an ideal candidate for the accommodation and the positioning of functional groups to form a functional molecular assembly.

For the realisation of molecule-based electronic devices the understanding and control of intermolecular and molecule-substrate interactions are crucial [1–4]. Directed supramolecular aggregation is achieved by adjusting intermolecular interactions and choosing appropriate substrates [3, 4]. Hexa-*peri*-hexabenzocoronene (HBC, $C_{42}H_{18}$) is a polycyclic aromatic hydrocarbon and can be viewed as being disc-shaped, hydrogen terminated two-dimensional graphite sections. The molecules are large enough to accommodate functional groups and therefore, the study of their growth mode and the control of it are of great importance. For the hexaalkyl-substituted derivatives of HBC high solubility and the ability to self-organize into a columnar mesophase in organic solvents has been shown [5, 6]. These structures are one-dimensional conductors with a very high charge carrier mobility [6–8]. However, the deposition of similar one-dimensional structures at surfaces would be desirable in view of a controlled positioning and orientation of such columns.

In this work we report on the growth mode of thin films of the insoluble HBC prepared by vacuum sublimation onto Au(111) and Cu(111). We show that the two-dimensional structural information of the first molecular monolayer is transmitted to molecules of the following layers yielding columnar stacks of HBC with substrate-dependent stack separation. The observed aggregation into columnar structures is completely different from the well-known herringbone bulk structure [9]. The combination of low energy electron diffraction (LEED) and X-ray photoelectron diffraction (XPD) allows the determination of the intermolecular ordering and the orientation of the adsorbed molecules within the columns. XPD in combination with single-scattering cluster (SSC) calculation has been proven adequate for near-surface and adsorbates structure determination of carbon allotropes [10, 11] and is used here for the determination of the intracolumn molecular ordering.

Experiments were performed in an OMICRON photoelectron spectrometer modified for motorized sequential angle-scanning data acquisition having a base pressure in the low 10^{-11} mbar range. X-ray photoelectron spectra and diffraction patterns were measured using Mg Kα ($h\nu$ = 1253.6 eV) radiation. The preparation of Au(111) and Cu(111) single crystals was done by repeated cycles of Ar^+ ion sputtering and subsequent annealing to 600°C and 550°C,

respectively. HBC was evaporated from a resistively heated stainless steel crucible. After outgassing below the sublimation temperature, molecules were evaporated at 400°C with the chamber pressure staying below $1 \cdot 10^{-9}$ mbar.

A monolayer of HBC was prepared by evaporation of several layers on the clean surfaces and subsequent annealing above the sublimation temperature of HBC, which results in a well ordered HBC monolayer, as confirmed by LEED.

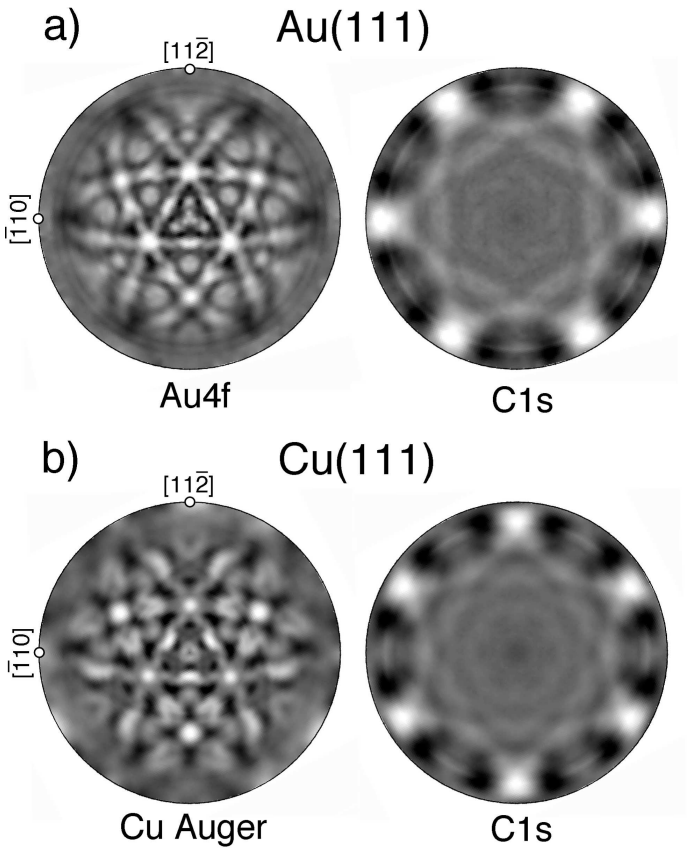

Figure 5.1: Experimental photoelectron diffraction patterns of substrate and monolayer film signal. Intensity plots are shown in stereographic projection with the center showing normal emission and the circle showing emission at $\vartheta = 90°$. White corresponds to highest intensity. (a) Monolayer of HBC on Au(111). Substrate $Au4f_{7/2}$ (E_{kin} = 1170 eV) and C1s (E_{kin} = 970 eV) signal. (b) Monolayer film on Cu(111). Cu L_3VV (E_{kin} = 919 eV), C1s (E_{kin} = 970 eV).

Figure 1 shows diffraction patterns of the simultaneously recorded C1s and substrate signals for a monolayer of HBC on Au(111) and Cu(111), respectively. Prominent maxima in the diffraction patterns can be interpreted as nearest-neighbour directions [12]. For the C1s diffraction pattern the strongest maxima, originating from the C-C bond directions, are found at angles close to 90° off normal, indicating that molecules are adsorbed flat on the surface. The strongest maxima show the directions of the C-C bonds; focusing in the direction of the next-nearest neighbours yields weaker features rotated by 30° to the principal maxima. Comparison to the substrate diffraction pattern then allows the determination of the molecular orientation with respect to the substrate lattice.

On Au(111) the molecular HBC monolayer film forms a hexagonal $\begin{pmatrix} 3 & 3 \\ -3 & 6 \end{pmatrix}$ structure, whereas that on Cu(111) shows a LEED pattern corresponding to a hexagonal arrangement of the molecules with the two possible domains $\begin{pmatrix} 5 & 1 \\ -1 & 6 \end{pmatrix}$ and $\begin{pmatrix} 6 & -1 \\ 1 & 5 \end{pmatrix}$. The combination of the results from XPD and LEED allows a complete picture of the molecular ordering in terms of intermolecular distance and molecule orientation (Fig. 2).

On Au(111) HBC has its molecular axis (labeled m in Fig. 2) parallel to the molecular lattice vector [01] with a nearest-neighbour distance of 15.0 Å. On Cu(111) the molecules adsorb with the molecular axis rotated by 9° relative to the molecular lattice vectors and with a nearest-neighbour distance of 14.2 Å. Structural data of the monolayer systems are summarized in table 5

In general, the two-dimensional ordering depends on the interplay of the molecule-substrate and the intermolecular interactions. The growth of commensurate superstructures requires a sufficiently strong molecule-substrate interaction. This molecule-substrate interaction modulates the intermolecular

Substrate	Superstructure	HBC [01] rel. to subs. [11$\overline{2}$]	N.-N. distance	Orientation of mol. axis rel. to HBC [01]
Au(111)	$(\sqrt{27} \times \sqrt{27})R30°$	60°	15.0 Å	0°
Cu(111)	$(\sqrt{31} \times \sqrt{31})R \pm 8.95°$	$30 \pm 9°$	14.2 Å	±9°

Table 5.1: Structural data of the two-dimensional HBC films on Au(111) and Cu(111). The ± stands for the two possible domains on Cu(111).

potential with a contribution having the periodicity of the substrate lattice. If this contribution is strong enough, the equilibrium distance between two molecules in the first monolayer can be changed to a distance that is commensurate to the substrate lattice. Furthermore, molecules can be rotated away

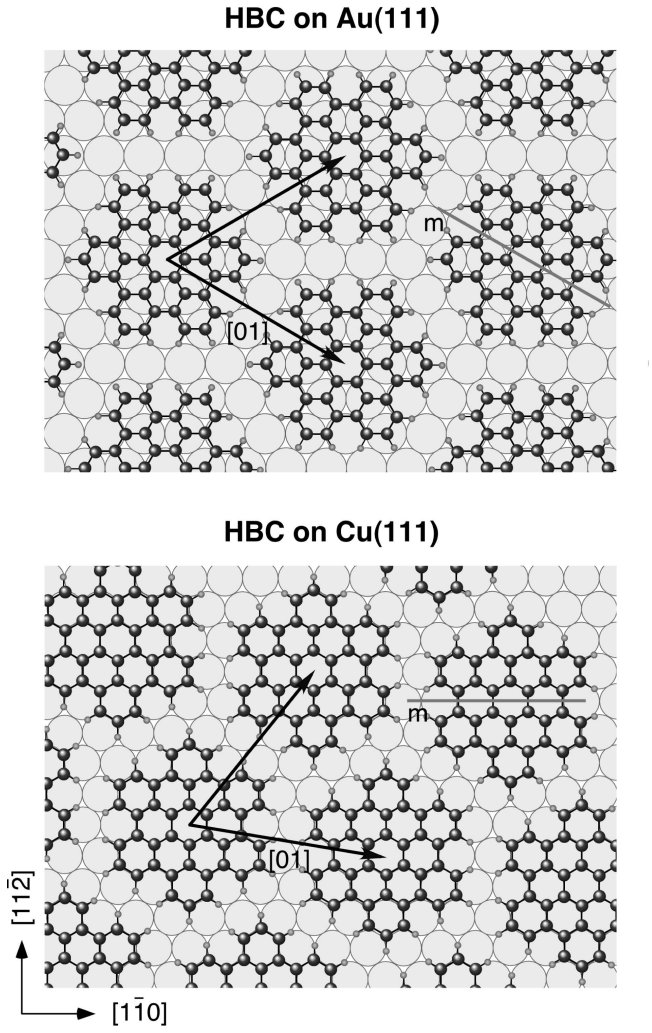

Figure 5.2: Two dimensional ordering of HBC molecules on Cu(111) (a) and Au(111)(b). Lattice vectors of the substrate and the molecular film are indicated with arrows. Lines labeled m indicate the molcular axis of HBC.

from the equilibrium orientation in the absence of the substrate interaction, for which in the case of HBC the molecular axis m is aligned with the [01] direction. The equilibrium distance d_0 found from the intermolecular potential calculation for a molecular monolayer film is 14.1 Å in the absence of substrate interaction (details of the calculation are given below), which is lower than the observed nearest-neighbour distances of 15.0 Å and 14.2 Å for the Au(111) and Cu(111) surfaces, respectively. The expansion of the molecular lattice by ~ 6 % on Au(111) and the molecule rotation of 9° on Cu(111) indicate a rather strong molecule-substrate interaction on both investigated substrates resulting in films with different densities and molecule orientations.

In order to study the three-dimensional stacking of HBC, subsequent layers have been evaporated onto the ordered monolayer systems. As evidenced by LEED, the superstructure remains the same as for the monolayer film. [13] The XPD patterns of $\sim$ 10Å thick multilayers deposited on Cu(111) and Au(111) are displayed in Fig. 3 a) and b). In contrast to the patterns of monolayer films, new features are expected to appear at non-grazing emission due to the appearance of new scatterers in the next higher layer. However, SSC calculations for the case where all second layer molecules have the same offset with respect to first layer molecules show much more distinct features near normal emission than the experimental patterns. This low number and low anisotropy of features near normal emission of the experimental XPD pattern suggests a multitude of possible lateral offsets, a model which will be discussed in the last part. The intensity maxima at grazing emission remain unchanged, indicating the preservation of molecular orientation during film growth. The degree to which the orientation is preserved can be estimated from the variation of the anisotropy of the intensity in the XPD pattern. As at grazing emission surface sensitivity is highest, changes in anisotropy directly indicate the degree of orientational ordering of the topmost molecules of the stacks. The anisotropy of the intensity at grazing emission remains on the level of the monolayer system (0.18) for thicknesses of up to about 20 Å. For even higher stacks ($\sim$25 Å) the anisotropy drops only to 0.14. This is most likely due to an increasing misorder in the azimuthal orientation and not due to a tilting of the molecules, since it has been shown for multilayer films deposited on flat substrates, that the

molecules lie flat for film thicknesses of up to ∼100 Å [14]. The results from LEED and XPD suggest the growth of columns of flat lying molecules where the molecule orientation in the column is preserved.

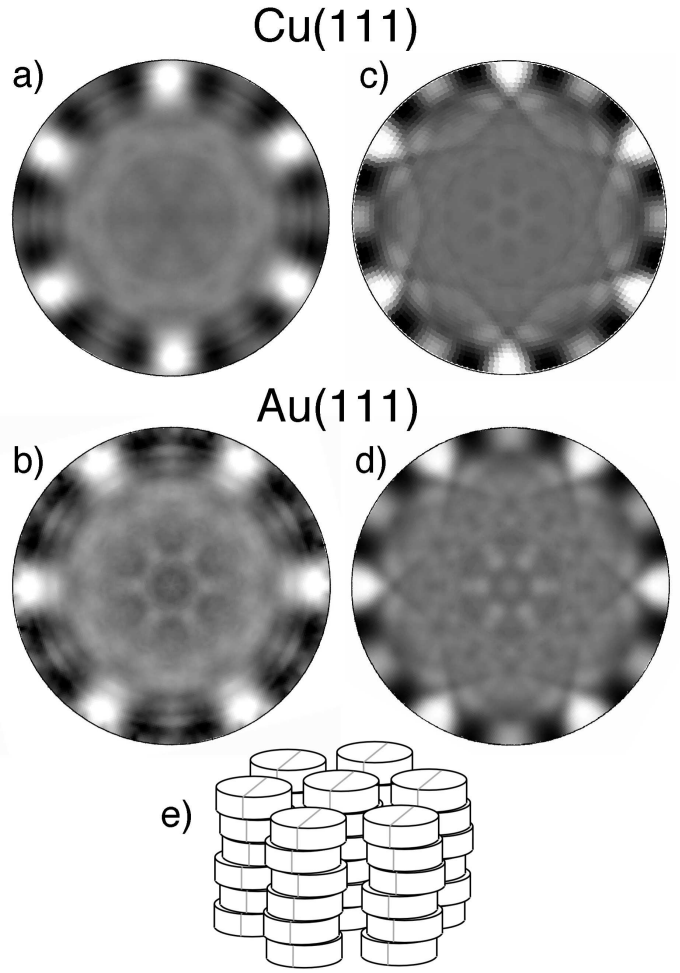

Figure 5.3: Multilayer films ($n \simeq 3$) of HBC. (a) Experimental XPD pattern of the C1s signal ($E_{kin} = 970$ eV) on Cu(111). (b) Exp. XPD pattern of C1s on Au(111). (c) SSC pattern calculated for various positions allowed at room temperature (see text). (d) Averaged SSC pattern for various shifts of subsequent molecules in the direction of the C-C bond. Offsets for the individual calculations were in the range of 0.6 to 1.2 Å. (e) Proposed column structure.

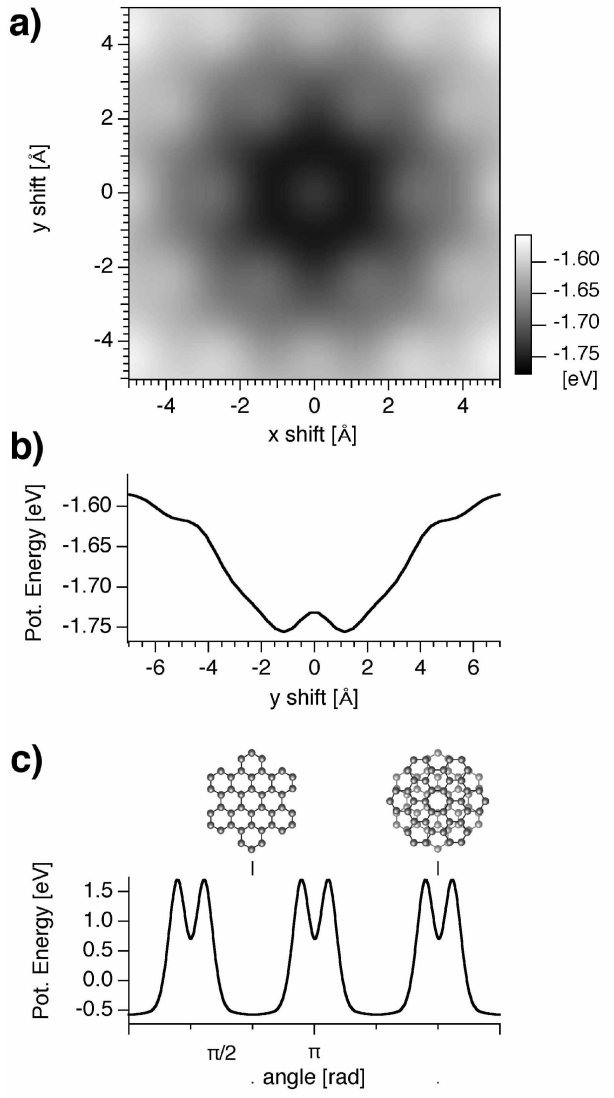

Figure 5.4: Calculation of the intermolecular potential of a single HBC molecule on a completed monolayer HBC/Au(111) film. The intermolecular equilibrium distance in z is found to be 3.4 Å. (a) Potential as a function of xy-shift with respect to the center of a molecule of the first layer. (b) Potential as function of y-shift at x=0. (c) Interaction with nearest-neighbour molecules in the same layer as a function of molecule orientation.

The intermolecular potential has been calculated for different stacking positions of a HBC molecule on a completed monolayer using a Lennard-Jones potential of the type of $V_{ij}(r_{ij}) = 4\varepsilon_{ij}\left[\left(\frac{\sigma_{ij}}{r_{ij}}\right)^{12} - \left(\frac{\sigma_{ij}}{r_{ij}}\right)^{6}\right]$, which describes well nonbonded intermolecular interactions between hydrocarbons and fullerenes [15, 16]. The parameters ε_{ij} and σ_{ij} for C-C and H-H interactions are taken from the work of Stuart [15]. The mixed parameters ε_{CH} and σ_{CH} are determined according to the Lorentz-Berthelot combining rules [17]. Atom coordinates of the molecule were taken from the X-ray analysis of Goddard *et al* [9]. In order to determine the position a molecule would take when adsorbing on a completed monolayer, a HBC molecule and its six nearest-neighbours were taken at fixed positions as determined by LEED and XPD and one molecule of the second layer was used as probe. The position-dependent potential was calculated by summing up the interaction potentials of each of the atoms in the molecule of the second layer with all the atoms of the molecules of the first layer. A potential plot obtained in this way is shown in Fig. 4 a) showing the dependence on the xy-shift of the top molecule with respect to the molecule underneath. Coordinates for molecules of the first layer are taken for the HBC/Au(111) superstructure (see table 5). The vertical equilibrium distance between two layers is 3.4 Å. The offset dependence of the intermolecular potential is dominated by the attractive part of the intermolecular potential which favours on axis columnar aggregation in order to maximize the overlapping of two molecules. On the other hand the energetically favoured sequence of stacked graphene sheets is ABA, where subsequent layers are shifted by 1.42 Å relative to each other. This contribution can be seen as a $\sqrt{3} \cdot 1.42$ Å modulation of the potential and is responsable for the off-center position (1.2 Å) of the potential minimum. However, for a single molecule adsorbed in the second layer, the absolute potential minimum is found for an azimuthal rotation of 30° relative to first-layer molecules (not shown). This orientation of the molecules becomes unfavorable if nearest-neighbors in the second layer are taken into account (Fig 4c). The facing hexagon corners of neighboring molecules are in the repulsive regime of the van der Waals interaction if molecules are not aligned to molecules of the first layer. This promotes the realignement during film growth and explains the observed conservation of the molecular orientation on multi-

layer samples. We performed SSC calculations for molecule stacking sequences according to the calculated intermolecular potential. The set of offset positions was chosen to obey the Maxwell-Bolzmann distribution at 300 K with regard to the calculated potential energy. At room temperature the thermal energy is high enough to allow lateral offsets of up to ~ 2Å. The resulting averaged SSC pattern is shown in Fig. 3(b) where the intensity near the normal emission shows indeed a very poor structure due to the averaging of different possible offsets. This reproduces very well the experimental XPD pattern observed for the multilayer deposited on Cu(111).

In comparison to Cu(111), the multilayer on Au(111) shows an enhanced anisotropy at small polar angles, indicating an increased constrain on the possible offset positions. The remaining structure at $\vartheta \simeq 24°$ could be reproduced with SSC by the average pattern of various lateral offsets in the C-C bond direction (Fig. 3 d). This preferred offset from the column axis possibly originates from the interaction with neighbouring molecules of the same layer. The equilibrium distance between them is 14.1Å and thus for the column separation on Au(111) (15.0Å) an attractive force exists between these molecules resulting in typical offsets of ~ 1Å. Larger off-center distances are energetically unfavourable (Fig. 4b) which promotes the growth of columnar structures with small lateral offsets.

In conclusion, we have shown that adsorption of HBC on Au(111) and Cu(111) forms ordered molecular monolayer films with a superlattice that is commensurate to the substrate lattice due to a sufficent molecule-substrate interaction. The intermolecular distances on Au(111) and Cu(111) are 15.0 Å and 14.2 Å, respectively. Due to the attractive part of the intermolecular potential, subsequently deposited molecules are adsorbed flat near the center of the first-layer molecules. The molecular lattice of the first monolayer is thus transmitted to the following layers of molecules resulting in the growth of columnar stacks with conservation of the molecule orientation and a limited offset from the columnar axis. In that sense, the ordered monolayer system acts as template for the growth of columnar structures with a substrate dependent stack separation. The prospect of this work is the building of scaffoldings made of molecular stacks for the positioning of functional groups.

Financial support by the Swiss National Science Foundation (NFP 47 and MaNEP) is greatfully acknowledged.

References for Chapter 5

[1] C. Joachim, J.K. Gimzewski, and A. Aviram, Nature **408**, 541 (2000)

[2] N. Karl and Ch. Günther, Cryst. Res. Technol. **34**, 243 (1999)

[3] T. Yokoyama, S. Yokoyama, T. Kamikado, Y. Okum, and S. Mashiko, Nature **413**, 619 (2001)

[4] G. P. Lopinski, D. D. M. Wayner, and R. A. Wolkow, Nature **406**, 48 (2000)

[5] P. Herwig, C.W. Kayser, K. Müllen, and H.W. Spiess, Adv. Mater. **8**, 510 (1996).

[6] A.V. de Craats, J. Warman, A. Fechtenkötters. J.D. Brandt, K. Müllen, Adv. Mater. **11**, 1469 (1999)

[7] D. Adam, F. Closs, T. Frey, D. Funhoff, D. Haarer, H. Ringsdorf, P. Schuhmacher, and K. Siemensmeyer, Phys. Rev. Lett. **70**, 457 (1993).

[8] S. Ito, M. Wehmeier, J.D. Brand, C. Kübel, R. Epsch, J.P. Rabe, and K. Müllen, Chem. Eur. J. **6**, 4327 (2000).

[9] R. Goddard, M.W. Haenel, W.C. Herndon, C. Krüger, and M. Zander, J. Am. Chem. Soc. **117**, 30 (1995).

[10] R. Fasel, P. Aebi, R.G. Agostino, D. Naumović, J. Osterwalder, A. Santaniello, and L. Schlapbach, Phys. Rev. Lett. **76**, 4733 (1996).

[11] R.M. Küttel, R.G. Agostino, R. Fasel, J. Osterwalder, and L. Schlapbach, Surf. Sci. **312**, 131 (1994).

[12] J. Osterwalder, P. Aebi, R. Fasel, D. Naumovic, P. Schwaller, T. Kreutz, L. Schlapbach, T. Abukawa, and S. Kono, Surf. Sci. **331-333**, 1002 (1995).

[13] H. Proehl, M. Toerker, F. Sellam, T. Fritz, K. Leo, C. Simpson, and K. Müllen, Phys. Rev. B **63**, 205409 (2001)

[14] M. Keil, P. Samorí, D.A. dos Santos, T. Kugler, S. Stafström, J.D. Brand, K. Müllen, J.L. Brédas, J.P. Rabe, and W.R. Salaneck, J. Phys. Chem. B **104**, 3967 (2000).

[15] S.J. Stuart, A.B. Tutein, and J.A. Harrison, J. Chem. Phys. **112**, 6472 (2000).

[16] J. Song and R.L. Cappelletti, Phys. Rev. B **50**, 14678 (1994).

[17] G.H. Hudson and J.C. McCoubrey, Trans. Faraday Soc. **56**, 761 (1959).

Appendix A

Experimental Determination of the Transmission Factor for the Omicron EA125 Electron Analyzer

P. Ruffieux, P. Schwaller, O. Gröning, L. Schlapbach and P. Gröning

Institut de Physique, Université de Fribourg, Pérolles, CH-1700 Fribourg, Switzerland

Q.C. Herd

Omicron Electron Spectroscopy Ltd., Manchester M17 1NF, United Kingdom

D. Funnemann and J. Westermann

Omicron Vakuumphysik GMBH, D-65232 Taunusstein, Germany

published in Rev. Sci. Instrum. **71**, 3634 (2000)

In this paper a study of the transmission factor of the

Omicron EA 125 analyzer equipped with the universal lens is presented. The procedure is based on a model by Cross and Castle (J. Electron Spectroscopy Relat. Phenom. **22**, 53 (1981)) and is applicable to every spectrometer which can be operated in the Constant Analyzer Energy (CAE) and in the Constant Retarding Ratio (CRR) measuring mode. The advantage of the method is its independence on the sample and on the inelastic mean free path of the electrons. We find that the transmission factor for the CAE-mode is proportional to E_{kin}^{-1} for most measuring setups. This dependence is predicted by theory for an ideal analyzer. Deviations from this behavior are observed if the retarding ratio for a given kinetic energy is too small. The limit value of the retarding ratio for ideal behavior, i.e. an E_{kin}^{-1} transmission factor, depends on the analyzer entrance slit aperture which has been selected.

A.1 Introduction

X-ray photoelectron spectroscopy (XPS) is a widely used and versatile tool to study the chemical composition within the near surface region of solids [1]. For an accurate quantitative analysis the intensities of core-level peaks in an XPS spectrum have to be precisely determined. The photoelectron intensity I of a core-level measured at a kinetic energy E_{kin} can be expressed by the following relation:

$$I \propto n \cdot \sigma \cdot \lambda(E_{kin}) \cdot T(E_{kin}) \cdot cos(\theta) \tag{1}$$

In equation (1) n is number of atoms per area, σ the photoionization cross section [2], $\lambda(E_{kin})$ the inelastic mean free path of the photoelectrons, $T(E_{kin})$ the analyzer transmission factor (see below) and θ the photoelectron emission angle with respect to the surface normal. $\lambda(E_{kin})$ depends on the kinetic energy E_{kin} and on the interlayer distance d of the sample and can be expressed by [3,4] ($\lambda(E_{kin})$ and d in Å):

$$\lambda(E_{kin}) = 538 \cdot \frac{d}{E_{kin}^2} + 0.13 \cdot \sqrt{d^3 \cdot E_{kin}} \tag{2}$$

Within a first approximation, the first term in equation (2) can be neglected for kinetic energies in the XPS range (50 - 2000 eV) so that

$$\lambda(E_{kin}) \propto \sqrt{E_{kin}} \tag{3}$$

$T(E_{kin})$ is the transmission factor of the electron analyzer. The transmission factor has to be known for a reliable quantitative XPS analysis but this factor is unique to every analyzer type [5]. In this paper, a detailed study of the transmission factor for the Omicron EA 125 analyzer is presented [6]. The results are also valid for the EA 125 HR analyzer which is for all points relevant to the transmission identical to the EA 125. Note that for many spectrometer types the factories provide so-called "sensitivity factors" which include cross-sections and transmission factors. The procedure we applied is based on work of Cross and Castle [7] and is applicable to all hemispherical analyzers which can be used in both, the constant analyzer energy (CAE) mode, as well as in

the constant retarding ratio (CRR) mode. Basically one has to measure the same photoelectron spectrum in both measuring modes. From the intensity ratio of the two spectra the transmission factor can then be determined (see below).

The advantage of the method is its independence from the X-ray source and the sample type or quality as long as the X-ray flux and the surface quality remain constant during the measurements. It is also independent of the mean free path $\lambda(E_{kin})$. This is important because equation (2) is certainly adequate for normal metals, but may be different for oxides or polymers for example. In fact, the sample is here used as an electron source. Often analyzer transmission factors are determined using an electron point source. Using a sample as "extended electron source" has the advantage that not only the ideal electron trajectory in the center of the lens is tested, but also the off-center region, so that possible lens aberration effects are taken into account.

Figure A.1 shows a schematic representation of the Omicron EA125 analyzer. Details can be found in [8]. The analyzer consists of a hemisphere and of an electrostatic lens system (in our setup the so-called *universal lens*). The lens system can be divided into two parts: The magnification lenses are used to adjust the spatial and angular resolution of the analyzer. Three magnification modes are available: High (small spot size, low angular resolution), Low (large spot size, high angular resolution) and Medium (in between Low and High magnification). The magnification is changed by activating different lens elements. In the first section of the lens the focussing voltages run proportional to the electron kinetic energy. For medium and low magnification mode the lens is operated as a "single lens". A non-adjustable aperture at the end of this lens is put at the position of the disk of least confusion. This is the position with the maximum electron transmission. This aperture stops the most aberrated electrons (and in this respect it is an angle defining aperture) and serves for pre-defining the sampled area.

The second stage of the lens system is used to retard the photoelectrons from their kinetic energy in vacuum (E_{kin}) down to the desired pass energy (PE) in the hemisphere. This zoom lens stage images the electrons from the aperture of the first lens onto the entrance slit of the hemispheres. An angular

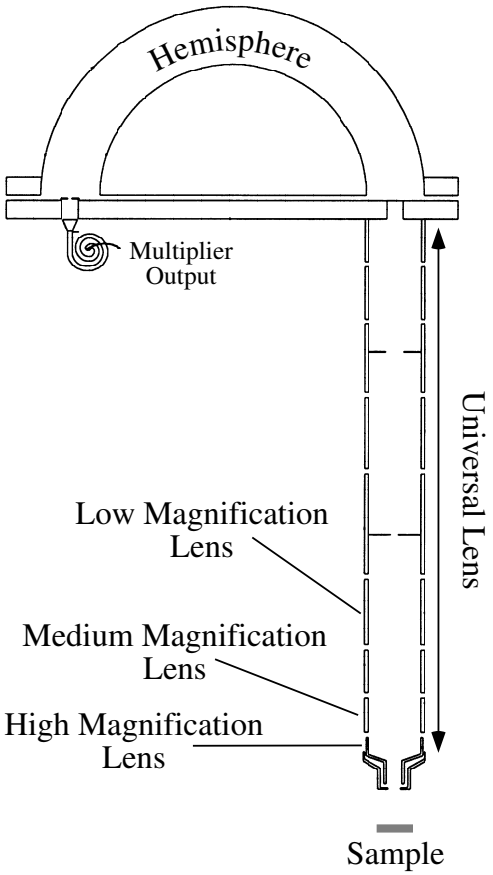

Figure A.1: Schematic representation of the EA 125 electron analyzer [8].

defining aperture is positioned in its focal plane.

Although discussed as separate stages, the whole lens system was calculated as one integral unit with the emphasis on focussing and defining an electron beam from the sample onto the variable entrance slit of the hemisphere. The following entrance slit apertures are selectable: 6 mm x 12 mm, circular 6 mm diameter, circular 2 mm diameter, circular 1 mm diameter and 1 mm x 12 mm.

Taking the work of Cross and Castle [7], the transmission factor $T(E_{kin})$ can be written as

$$T(E_{kin}) = L(E_{kin}) \cdot H(E_{kin}) \tag{4}$$

where $L(E_{kin})$ is the transmission of the lens system and $H(E_{kin})$ the transmission of the analyzer hemisphere. The derivation of the relations for the transmission factors is described in [7] and will not be further discussed here. For the CAE measuring mode the hemisphere and lens transmissions are given by [7]

$$H_{CAE} = PE \cdot k \tag{5}$$

$$L_{CAE}(E_{kin}) = \frac{PE}{E_{kin}} \tag{6}$$

In equations (5) and (6) PE is a *fixed* analyzer pass energy, E_{kin} the kinetic energy of the photoelectrons and k a constant which is characteristic for the analyzer.

The corresponding relations for the CRR mode with a *fixed* retarding ratio $RR = \frac{E_{kin}}{PE}$ are [7]

$$H_{CRR}(E_{kin}) = \frac{E_{kin}}{RR} \cdot k \tag{7}$$

$$L_{CRR} = RR^{-1} \tag{8}$$

Using equations (1) and (4-8) the intensity ratio $R(E_{kin})$ between two XPS spectra with identical settings (same measuring range, same X-ray flux, no sample degradation etc.), but one measured in the CAE mode and the other in the CRR mode, can be written as

$$R(E_{kin}) = \frac{T_{CAE}}{T_{CRR}} = \frac{(PE \cdot RR)^2}{E_{kin}^2} \tag{9}$$

Equation (9) is valid for an ideal electron lens system. Cross and Castle treat deviations from an ideal system by taking an exponent of the form $1 + x$ in equation (9):

$$R(E_{kin}) = (\frac{PE \cdot RR}{E_{kin}})^{1+x} \tag{10}$$

We will use the $1 + x$ correction factor only for the kinetic energy term E_{kin} in the denominator of equation (9):

$$R(E_{kin}) = \frac{(PE \cdot RR)^2}{E_{kin}^{1+x}} \tag{11}$$

Using equation (11) we are only fitting the *shape* of the $R(E_{kin})$ curve. The numerical values of the $R(E_{kin})$ curve should be independent of the transmission factor. It is known [7] that the hemisphere transmission in the CRR mode is proportional to E_{kin} (equation (7)). Therefore by using equation (11) the transmission factor in the CAE mode, the measuring mode which is today mainly used for XPS experiments, is given by

$$T_{CAE}(E_{kin}) \propto E_{kin}^{-x} \tag{12}$$

The intensity ratio between two core-level signals 1 (energy E_1) and 2 (energy E_2) can then be expressed by

$$\frac{I_1}{I_2} = \frac{n_1 \cdot \sigma_1 \cdot \sqrt{E_1} \cdot cos(\theta) \cdot E_1^{-x_1}}{n_2 \cdot \sigma_2 \cdot \sqrt{E_2} \cdot cos(\theta) \cdot E_2^{-x_2}} \tag{13}$$

If the parameter x is determined using equation (10) the intensity ratio is equal to

$$\frac{I_1}{I_2} = \frac{n_1 \cdot \sigma_1 \cdot \sqrt{E_1} \cdot cos(\theta) \cdot (PE \cdot RR)^{1+x_1} \cdot E_1^{-x_1}}{n_2 \cdot \sigma_2 \cdot \sqrt{E_2} \cdot cos(\theta) \cdot (PE \cdot RR)^{1+x_2} \cdot E_2^{-x_2}} \tag{14}$$

Using equation (10) has the disadvantage that for every pass energy the parameter x has to be determined whereas the x values found using equation (11) are universal (see also the numerical results in tables A.3 and A.3).

The parameter x can be determined by measuring photoelectron spectra in the CAE and the CRR mode and to fit the experimental intensity ratio by the functions shown in equations (10) and (11). It is worthwhile mentioning that x is the only fit parameter and we would again emphasize that a major advantage of the procedure described above for the determination of the transmission factor is that it is completely independent of the knowledge of the inelastic mean free path $\lambda(E_{kin})$.

What would be an ideal analyzer transmission factor for quantitative XPS ?

First, the most basic requirement is that the transmission factor is predictable, i.e. it can be calculated. The transmission factor needs not necessarily be of a shape as given by equation (11). Any continuous and smooth function would fulfil this requirement. Discontinuities in a spectrum could be generated when using non-linear lens curves with not enough support points.

Second, the Helmholtz-Lagrange (H.L.) law [9] states that between two points 1 and 2, if current is conserved, the product of (object) size a, (acceptance) angle φ and square root of energy E_{kin} of the electrons is conserved:

$$a_1 \cdot \varphi_1 \cdot \sqrt{E_{kin}} = a_2 \cdot \varphi_2 \cdot \sqrt{PE} \tag{15}$$

Equation (11) is based on this law. A real electron transport system has all kind of aberrations which through the action of apertures reduce the beam intensity. We call an analyzer ideal that follows equation (11) with the exponent x as close as possible to one. It has for given parameters of a and φ the highest possible transmission at a given retard ratio range.

A.2 Experimental

All measurements have been done on an Ar-ion sputtered polycrystalline Al sample with a diameter of 16 mm. The photoelectrons were excited using a non-monochromatized Al Kα X-ray source (photon energy 1486.6 eV). For all measurements it has been checked that sample properties and X-ray flux did not change during the experiments. Fig. A.2 shows as illustration photoelectron spectra measured in the CAE mode with a pass energy PE of 40 eV and in the CRR mode (Retarding ratio $RR = 20$). Both spectra have been measured in the Low-Magnification mode and with the 6 mm x 12 mm analyzer entrance aperture. The relation $PE = \frac{E_{kin}}{RR}$ implies that the two spectra should have the same intensity at a kinetic energy corresponding to the product of RR and PE, i. e., at 800 eV in this particular case. As indicated by the vertical dashed line this is in fact the case.

Fig. A.3 shows as illustration the intensity ratios $R(E_{kin})$ measured in the Low-Magnification lens mode for two different analyzer entrance apertures. The inset shows an enlargement of both curves for the kinetic energy range between 1486.6 eV (Al Kα photon energy) and 600 eV. The dotted line has been obtained using the 6 mm x 12 mm entrance slit, the solid curve with the circular 6 mm slit.

The spike-like features around 1400 eV kinetic energy can be attributed to the prominent Al 2s and Al 2p core-level signals (see Fig. A.2): For a given kinetic energy the pass energies (i.e. the energy resolutions) are different for a CRR and a CAE spectrum (except for E_{kin}=800 eV in this particular case). As a consequence, core-level line shapes are different and this results in "spikes" in the $R(E_{kin})$ curves. From Fig. A.3 it can immediately be concluded

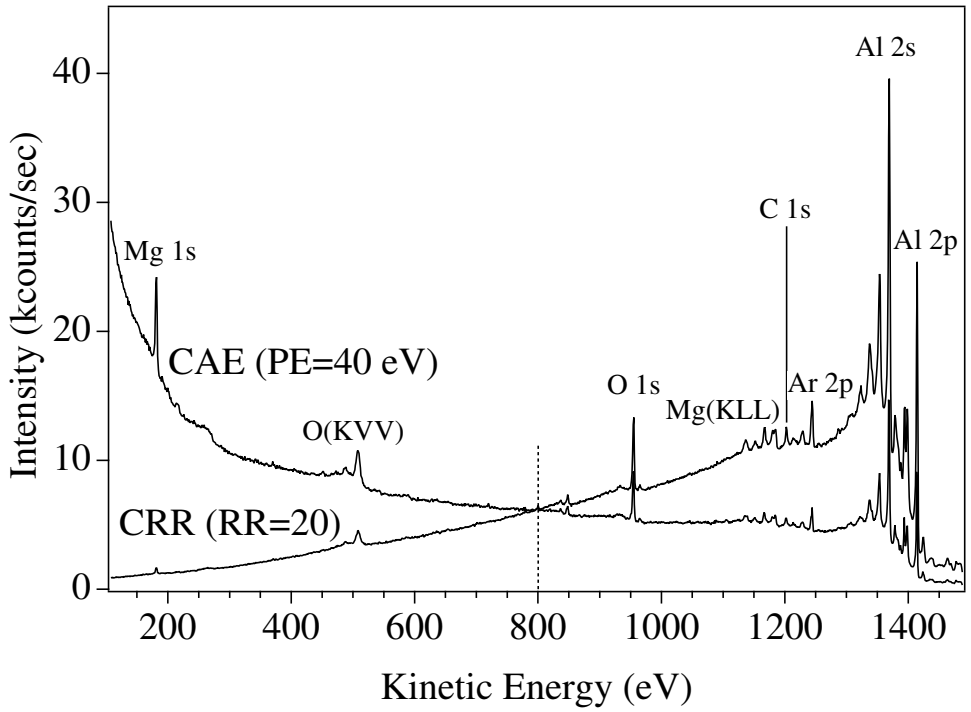

Figure A.2: Photoelectron spectra of polycrystalline Al measured in the CAE mode (Pass energy PE = 40 eV) and in the CRR mode (Retarding ratio RR = 20).

that for high kinetic energies (1486 - 700 eV) an unique transmission factor for both settings (6 mm x 12 mm and circular 6 mm entrance slit) exists. For lower kinetic energies ($E_{kin} < 700$ eV) however, significant differences occur. The quantitative analysis of these curves as well as possible reasons for the differences at low kinetic energies will be discussed in the next section.

A.3 Results and Discussion

The quantitative analysis of the experimental $R(E_{kin})$ curves has been done using equations (10) and (11). Fig. A.4 illustrates the results using equation (11) for one specific measurement ($PE = 40$ eV, $RR = 20$, Low Magnification and circular 6 mm entrance slit). Results obtained for other setups are summarized in tables A.3 and A.3. We have divided the curves into four different kinetic energy ranges: 1486.6 - 700 eV (Fig. A.4a), 700 - 450 eV (Fig. A.4b), 450 - 200 eV (Fig. A.4c), and 200 - 107.6 eV (Fig. A.4d) because better fit results have been obtained by this than by using one single exponent x over the whole kinetic energy range. As it is illustrated in Fig. A.4, the different parts of the experimental $R(E_{kin})$ curve (dots) can be adequately fitted (solid lines) by a $E_{kin}^{-(1+x)}$ function. For kinetic energies between 1486.6 eV and 700 eV (Fig. A.4a) and between 450 eV and 107.6 eV (Figs. A.4c,d) the values found for x correspond or are very close (0.98, 0.99) to the $x = 1$ value which is predicted by theory for an ideal analyzer. The most difficult part to fit is the range between 700 eV and 450 eV (Fig. A.4b). Even though a value of 0.99 for x is found, the $E_{kin}^{-(1+x)}$ curve follows the experimental curve only approximative.

The above values have been obtained for the low magnification mode. We have found that for a given pass energy PE, retarding ratio RR and analyzer entrance slit, there are no differences between the different magnification modes.

As can be seen from the results shown in Fig. A.4 the EA 125 analyzer behaves like an ideal analyzer, i.e., the Helmholtz - Lagrange equation (equation 15) is fulfilled. As it will be discussed below this seems not to be the case if the retarding ratio is too small for a given entrance slit or if the entrance slit is too large for a given retarding ratio (see also table A.3 and A.3).

Fig. A.5 shows $R(E_{kin})$ curves measured with the 6 mm x 12 mm entrance slit in the high magnification mode. For both curves a retarding ratio of 20 has been used for the CRR spectrum. The CAE spectrum has been measured with $PE = 40$ eV for the $R(E_{kin})$ curves in Figs. A.5a and b. For the curves in Figs. A.5c and d the CAE spectrum has been measured with $PE = 20$ eV. It is important to note that the only difference between the curves shown in Fig. A.5 is that the CAE spectrum in Figs. A.5a,b has been measured with a lower retarding ratio for a given kinetic energy. The high energy parts (1486.6 - 450 eV kinetic energy) are not shown because for both settings identical values have been found ($x = 0.99$ for E_{kin} between 1486.6 and 700 eV, $x = 1.00$ for

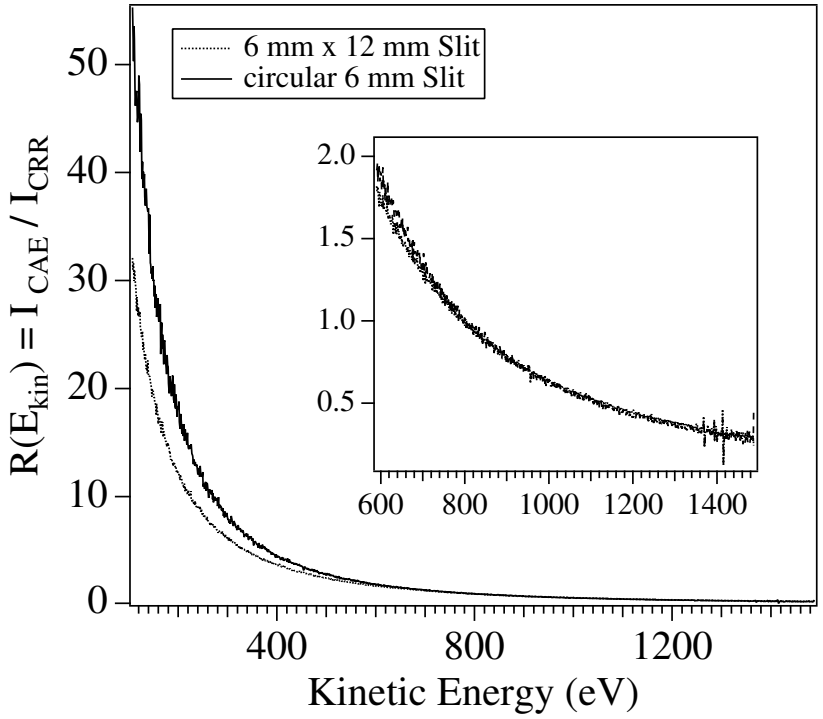

Figure A.3: $R(E_{kin})$ curves obtained from spectra measured with $PE = 40$ eV and $RR = 20$ for a 6 mm x 12 mm (dotted line) and for a circular 6 mm diameter (solid line) analyzer entrance slit aperture. The inset shows an enlargement of both curves for high kinetic energies.

E_{kin} between 700 and 450 eV). Significant differences are obeserved for kinetic energies below 450 eV. For the $R(E_{kin})$ curves in Figs. A.5a,b ($PE = 40$, $RR = 20$) no $E_{kin}^{-(1+x)}$ dependence (by using equation (11)) is found. From the experimental finding that only for kinetic energies above 450 eV (for the specific case of a pass energy of 40 eV and the 6 mm x 12 mm entrance slit) an ideal analyzer behavior is found (see also Figs. A.5a and b for energies below 450 eV) we can set the lowest kinetic energy for which the analyzer behaves like an ideal analyzer at 450 eV. Having a pass energy of 40 eV, the limit retarding ratio (for the 6 mm x 12 mm entrance slit) is therefore about 11. A similar value is found by the analysis of the $R(E_{kin})$ curves shown in Figs. A.5c,d (PE

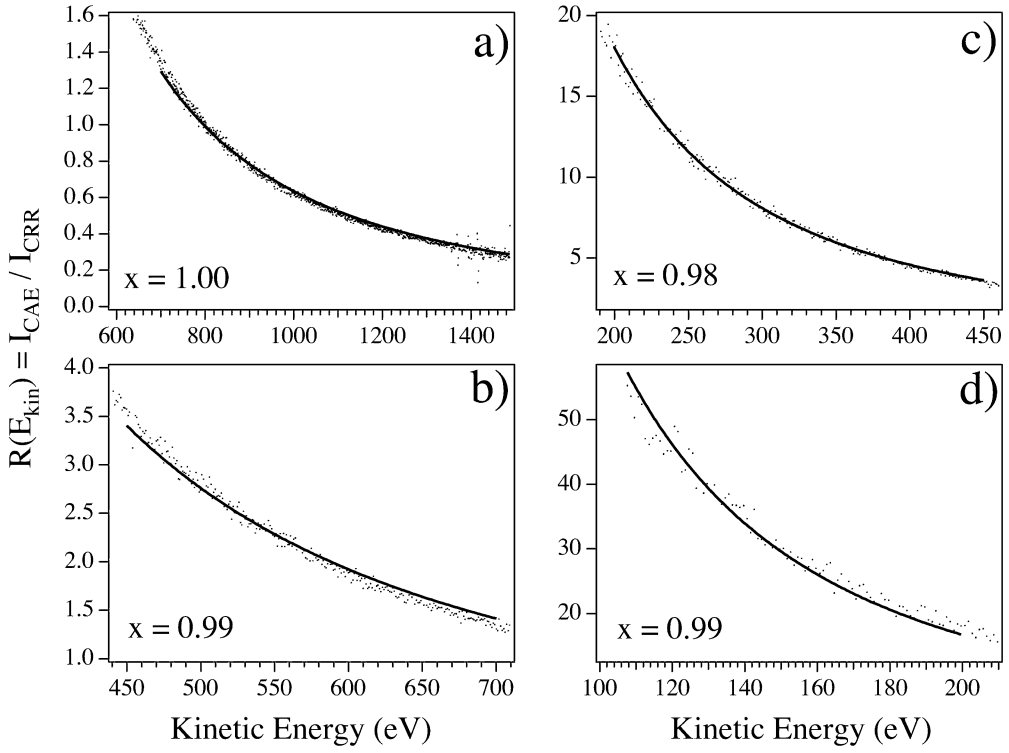

Figure A.4: (a)-(d): Experimental $R(E_{kin})$ curves (dots) and curve fits (solid lines) using equation (11) for different kinetic energy ranges for the circular 6 mm diameter entrance slit. All curves have been obtained from spectra measured with $PE = 40$ eV and $RR = 20$.

Entrance slit	1486.6 - 700 eV eq.(11)/eq.(10)	700 - 450 e eq.(11)/eq.(10)	450 - 200 eV eq.(11)/eq.(10)	200 - 107.6 eV eq.(11)/eq.(10)
circular 2 mm	1.00 / 1.00	0.98 / 1.23	0.98 / 1.11	0.99 / 1.01
circular 6 mm	1.00 / 0.96	0.99 / 1.19	0.98 / 1.06	1.01 / 0.97
6 mm x 12 mm	1.00 / 1.02	1.00 / 0.96	- / 0.84	- / 0.76
1 mm x 12 mm	1.00 / 0.87	1.00 / 1.06	- / 0.88	- / 0.78

Table A.1: Transmission factor exponent x determined using equation (11) (left column) and equation (10) (right column) for different analyzer entrance slits. The corresponding $R(E_{kin})$ curves have been measured with pass energy $PE = 40$ eV and retarding ratio $RR = 20$. The results are valid for all magnification modes. The error on x is ± 0.01. The - sign indicates that no reasonable curve fit using equation (11) has been possible.

= 20 eV, $RR = 20$). Here the limit is at about 200 eV, which corresponds to a retarding ratio of 10. We can therefore conclude that for the 6 mm x 12 mm entrance slit the CAE transmission factor is proportional to E_{kin}^{-1} as long as the retarding ratio is larger than approximately 10. This statement is also valid for the 1 mm x 12 mm entrance slit. For the circular 6 mm entrance slit the limit retarding ratio is found to be about 5, for the circular 2 mm slit about 2.5. If the entrance slit aperture for a given pass energy is reduced an E_{kin}^{-x} behavior with $x = 1$ or close to 1 is observed for a larger kinetic energy range (see tables A.3 and A.3).

This is also illustrated in Figs. A.4c and d, and in Figs. A.5a and b, respectively. All four curves have been obtained by measuring a CRR spectrum with a retarding ratio of 20 and a CAE spectrum with a pass energy of 40 eV. Whereas for the circular 6 mm entrance slit measurement (Figs. A.4c,d) the experimental data at low kinetic energies can be fitted by a function of the form $E_{kin}^{-(1+x)}$, no $E_{kin}^{-(1+x)}$ dependence is found at low kinetic energies for the 6 mm x 12 mm entrance slit measurement (always by using equation (11)). Again no differences are found for kinetic energies between 1486.6 and 450 eV. The fact that no E_{kin}^{-x} dependence of the transmission factor is found at low kinetic energies in this case may be explained by effects of off-center electron trajectories which will be most important for large slit apertures. Similar conclusions can also be made if the CAE spectra are measured with a pass energy of 80 eV. The results are summarized in table A.3. Compared to the measurements with

$PE = 40$ eV (table A.3) the entrance slit apertures have to be further reduced to get the behavior of an ideal analyzer over a large kinetic energy range.

It is worthwhile to mention that a satisfactory curve fit is always possible by using equation (10). Results are listed up in tables A.3 and A.3. However these results are only useful if the ratio of two transmission factors is formed (see equation (14)). Furthermore, x-values obtained from equation (10) are not universal but depend on the pass energy.

We will now discuss the fact that deviations from an ideal analyzer occur for low retarding ratios. The three magnification lenses (see Fig. A.1) do not change their object size and image size as a function of the retarding ratio. However, the retarding lenses (see Fig. A.1) select different sections of the magnification lens image for different retarding ratios. The spot becomes smaller for high retarding ratios (i.e. for high kinetic energies) and less off-center electron trajectories have therefore to be considered. The lower the retarding ratio, the larger the spot size and as a consequence off-center trajectories become more important. As a further consequence the sample analysis area and/or the angular resolution will vary in some degree with the kinetic energy. This spot-size variation as a function of the retarding ratio is a consequence of the H.L. law (equation 15). For a given slit width a_2 at the analyser, a constant pass energy PE, and a constant transmission angle through the analyser φ_2 there is a consequence on the input side of the lens system. For a lower kinetic energy (or lower retard ratio) the product of object size and angle

Entrance slit	1486.6 - 700 eV eq.(11)/eq.(10)	700 - 450 eV eq.(11)/eq.(10)	450 - 200 eV eq.(11)/eq.(10)	200 - 107.6 eV eq.(11)/eq. (10)
circular 2 mm	0.99 / 1.16	0.98 / 1.10	0.98 / 1.06	- / 0.95
circular 6 mm	1.00 / 1.03	1.00 / 0.99	- / 0.92	- / 0.81
6 mm x 12 mm	1.01 / 0.85	- / 0.81	- / 0.74	- / 0.67

Table A.2: Transmission factor exponent x determined using equation (11) (left column) and equation (10) (right column) for different analyzer entrance slits. The corresponding $R(E_{kin})$ curves have been measured with pass energy $PE = 80$ eV and retarding ratio $RR = 20$. The results are valid for all magnification modes. The error on x is ± 0.01. The - sign indicates that no reasonable curve fit using equation (11) has been possible.

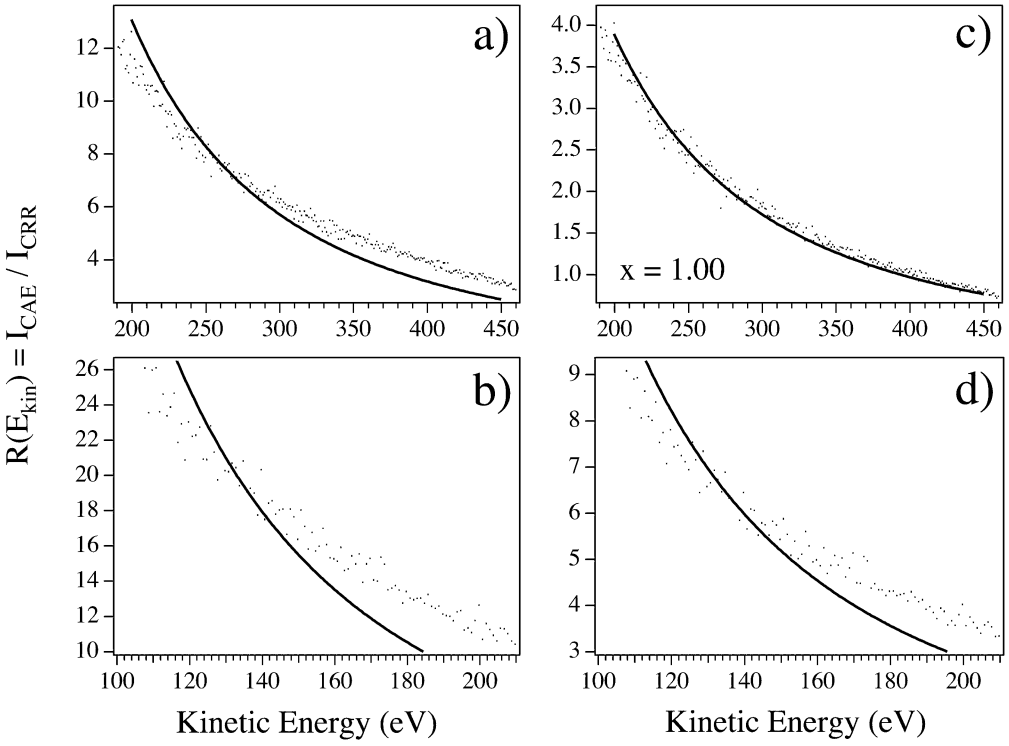

Figure A.5: (a)-(d): Experimental $R(E_{kin})$ curves (dots) and curve fits (solid lines) using equation (11) for different kinetic energy ranges for the 6 mm x 12 mm entrance slit. The curves have been obtained from spectra measured with $RR = 20$ eV and $PE = 40$ eV (a and b), and $PE = 20$ (c and d), respectively.

---

has to increase in order to fulfil equation (15). As a consequence, one needs homogeneous samples within the whole probed area. However, this behavior is suitable for a comfortable chemical characterization of a material.

A.4 Acknowledgments

Skillful technical assistance has been provided by E. Mooser, O. Raetzo, R. Schmid, F. Bourqui and C. Neururer. This work has been supported by the Swiss National Science Foundation and by the Commission of Technology and Innovation of Switzerland.

References for Appendix A

[1] S. Hüfner, Photoelectron Spectroscopy, Second Edition, Springer-Verlag, Berlin (1996).

[2] J.J. Yeh and I. Lindau, Atomic Data and Nuclear Data Tables **32**, 1 (1995).

[3] M.P. Seah and W.A. Dench, Surf. Int. Anal. **1**, 2 (1979).

[4] R.E. Ballard, J. Electron Spectrosc. Relat. Phenom. **25**, 75 (1975).

[5] M.P. Seah, Surf. Int. Anal. **2**, 222 (1980).

[6] Omicron Vakuumphysik GMBH, D-65232 Taunusstein, Germany.

[7] Y.M. Cross and J.E. Castle, J. Electron Spectroscopy Relat. Phenom. **22**, 53 (1981).

[8] EA 125 Electron Analyzer Technical Reference Manual.

[9] D. Roy and D. Tremblay, Rep. Prog. Phys. **53**, 1621 (1990).

Epilogue

Scientific work of recent years has shown that the successful description of phenomena at surfaces and in solids requires, beside the theoretical description, various experimental methods. Among the most successful recently developed methods are the scanning probe techniques. Their direct imaging capabilities on the atomic level have brought the missing piece for several questions related to surface phenomena. I hope to have convinced the reader that the area-integrating photoemission techniques and scanning probe microscopy are a powerful combination for the description of the surface and the near-surface region of solids and adsorbed molecule layers in the sense of yielding complementary information. Whereas XPD and ARUPS are well suited for the atomic and electronic structure determination of highly ordered and homogeneous thin films and near surface regions, the description of defects and other low-symmetry structures has to be addressed by the scanning probe techniques.

As exemplified by the presented results for sp^2-bonded carbon, scanning probe microscopy allows a profound insight into the local electronic structure of surfaces. However, although it reveals the function of the defects as scatterers for the delocalised electrons, the effect on the charge transport properties cannot be given quantitatively. Therefore, a future challenge will be the combination of the measurement of transport properties of carbon nanostructures (e.g. nanotubes) and the identification and modification of scatter-active defects with scanning probe microscopy. This step is necessary in order to allow the 'design' of devices with electronic functions on these nanostructures.

The investigations on the molecular films of HBC on metal surfaces have shown the influence of the substrate-molecule interaction on the structural parameters of the molecular assembly. To go one step further and to use the multiple chemical variations of HBC molecules as initial points for the building of molecular heterostructures, larger separations between the molecules are required. For this purpose, substrates with appropriate densities of molecule-specific nucleation centers need to be found, which demands a profound understanding and the possibility of adjustment of the molecule-substrate interaction. Therefore, an indespensable requirement to succeed in this field, is a

close collaboration between chemistry and physics.

Although only a very limited number of answers can be given during a thesis and many more questions arise, I hope to have shown that interesting phenomena arise in the presented systems which are relevant for the characterisation and design of structures on the nm-level. By all means, there remain numerous challenging tasks to be tackled for future investigations in this field.

Danksagung

Diese Doktorarbeit wurde in der Forschungsgruppe für Festkörperphysik von Prof. Louis Schlapbach unter der Leitung von Dr. Pierangelo Gröning ausgeführt.

Als erstes will ich mich bei Prof. Dr. Louis Schlapbach bedanken, der es mir ermöglicht hat, diese Doktorarbeit in seiner Gruppe auszuführen. Sein hilfsbereiter und herzlicher Umgang mit Menschen überträgt sich auf seine Forschungsgruppe, was ein hilfsbereites und motivierendes Umfeld für Forschungsarbeit schafft.

Ein ganz spezieller Dank geht an Dr. Pierangelo Gröning, der mich während dieser Doktorarbeit begleitet hat, für seine ständige Verfügbarkeit zur Diskussion von kleineren und grösseren Problemen. Er schafft es immer wieder, einem durch die richtigen Fragen dazu zu bringen, die 'Sache' auch von anderen Blickwinkeln zu betrachten.

Bei Dr. Oliver Gröning möchte ich mich ganz herzlich für seine Hilfsbereitschaft und sein Engagement bedanken. Sein breites Wissen und nicht zuletzt auch seine Virtuosität im Umgang mit 'Igor & Co.' mögen jederzeit zu beeindrucken.

Michael Bielmann und Patrick Schwaller danke ich für das Teilen des Büros mit mir und auch die Gespräche, die nicht immer direkt mit der Physik verbunden waren. Die Zusammenarbeit am Spektrometer war sehr angenehm.

Bedanken möchte ich mich auch bei allen anderen Mitarbeitern der FK-Gruppe für ihre Hilfsbereitschaft und anregenden Diskussionen. Im speziellen bei Dr. Andreas Züttel, Prof. Philipp Aebi, Philippe Mauron, Christian Koitzsch, Carine Galli und Marc Bovet.

Die ganzen Experimente wären unmöglich zu realisieren ohne die grosse und professionelle Unterstützung, die wir von unserer Werkstatt erfahren dürfen. Die Art, wie sie eine rudimentäre Skizze in ein brauchbares Stück Stahl umset-

zen, ist beeindruckend. Allen ein herzliches ‘Merci’.

Isabelle, danke für deine Aufmunterung wenn’s nötig war und alles andere ...

Curriculum vitae

Personal details

Family name	Ruffieux
First name	Pascal
Date of birth	May 23, 1973
Place of birth	Fribourg, Switzerland
Nationality	Swiss
Status	Single

Studies

1979 - 1988	Basic education in Plasselb/Plaffeien FR
1988 - 1992	High School in Fribourg, Kollegium Gambach Economy (Matura Typ E)
1992 - 1997	Studies in Physics:
1997	Diploma work in Solid State Physics: "Photoleitfähigkeitsmessungen an Diamant" under the direction of Dr. O.M. Küttel
10·1997 -	Graduate student in the Solid State Physics Group of Prof. Dr. Louis Schlapbach University of Fribourg, Switzerland

Publications

Photoelectron emission from nitrogen- and boron-doped diamond (100) surfaces
L. Diederich, O.M. Küttel, P. Ruffieux, T. Pillo, P. Aebi, and L. Schlapbach
Surf. Sci. **417**, *41 (1998)*

Hydrogen atoms cause long-range electronic effects on graphite
P. Ruffieux, O. Gröning, P. Schwaller, L. Schlapbach and P. Gröning
Phys. Rev. Lett. **84**, *4910 (2000)*

Experimental Determination of the Transmission Factor for the Omicron EA125 Electron Analyzer
P. Ruffieux, P. Schwaller, O. Gröning, L. Schlapbach and P. Gröning
Rev. Sci. Instrum. **71**, *3634 (2000)*

Carbon nanostructures: Growth, electron emission, interactions with hydrogen
L. Schlapbach, O. Gröning, L.O. Nillsson, P. Ruffieux, P. Sudan, P. Mauron, C. Emmenegger, P. Gröning, A. Züttel
Proc. of the International Winterschool on 'Electronic properties of molecular nanostructures', AIP **591** *(2001)*

Hydrogen adsorption on sp^2-bonded carbon: Influence of the local curvature
P. Ruffieux, O. Gröning, M. Bielmann, P. Mauron, L. Schlapbach and P. Gröning
accepted for publication in Phys. Rev. B (2002)

AgO investigated by photoelectron spectroscopy: Evidence for mixed valence
M. Bielmann, P. Schwaller, P. Ruffieux, O. Gröning, L. Schlapbach, and P. Gröning
Phys. Rev. B **65**, *235431 (2002)*

Supramolecular columns of hexabenzocoronenes on the copper and gold (111) surfaces
P. Ruffieux, O. Gröning, M. Bielmann, C. Simpson, K. Müllen, L. Schlapbach, and P. Gröning
Phys. Rev. B **66**, *073409 (2002)*

H_2 plasma treatment of silver contacts: impacts on wirebonding performace

M. Bielmann, P. Ruffieux, P. Schwaller, P. Sudan, L. Schlapbach, and P. Gröning

acc. for pub. in J. Electron. Mater. (2002)